PNNL-36716

Summary: Nuclear Energy Critical Material Waste Reduction and Supply Chain Solutions Enabled by Advanced Manufacturing

M2CR-22PN0401017

September 2024

Isabella van Rooyen
Carolyne Burns

Prepared for the U.S. Department of Energy
under Contract DE-AC05-76RL01830

PACIFIC NORTHWEST NATIONAL LABORATORY
operated by
BATTELLE
for the
UNITED STATES DEPARTMENT OF ENERGY
under Contract DE-AC05-76RL01830

Printed in the United States of America

Available to DOE and DOE contractors from
the Office of Scientific and Technical Information,
P.O. Box 62, Oak Ridge, TN 37831-0062
www.osti.gov
ph: (865) 576-8401
fox: (865) 576-5728
email: reports@osti.gov

Available to the public from the National Technical Information Service
5301 Shawnee Rd., Alexandria, VA 22312
ph: (800) 553-NTIS (6847)
or (703) 605-6000
email: info@ntis.gov
Online ordering: http://www.ntis.gov

PNNL-36716

Summary: Nuclear Energy Critical Material Waste Reduction and Supply Chain Solutions Enabled by Advanced Manufacturing

M2CR-22PN0401017

September 2024

Isabella van Rooyen
Carolyne Burns

Prepared for
the U.S. Department of Energy
under Contract DE-AC05-76RL01830

Pacific Northwest National Laboratory
Richland, Washington 99354

Summary

In September 2020, the U.S. government issued an executive order to address the threat to the domestic supply chain from its reliance on critical minerals (CMs) from foreign competitors and to support the domestic mining and processing industry. A national strategy on CMs with impact on the U.S. Department of Energy's (DOE's) vision for 2021–2031 was developed. This vision embraces science and technology to re-establish U.S. competitiveness in the CM and material supply chains by (a) scientific innovation and technologies to ensure resilient and secure CMs and maintain a domestic material supply chain, (b) building a long-term minerals and materials innovation ecosystem to foster new capabilities to mitigate CM supply chain challenges, (c) increasing private sector adoption for sustaining the domestic CM supply chain, and (d) coordinating with international partners and federal agencies to diversify global supply chains and ensure the adoption of best practices for sustainable mining and processing (DOE 2021).

The Advanced Materials and Manufacturing Technology (AMMT) program is addressing this executive order by evaluating advanced manufacturing (AM) and its impact on the demands of CMs for energy production in general and how the deployment of AM in nuclear energy will support the projected goals of the Paris Accord and further a net-zero carbon economy (NZE) by 2050.

From a list of 50 CMs and evaluations of the CMs related to advanced alloys selected for deployment in Gen-IV reactor systems, the following minerals were identified as most important to the nuclear industry: Al, Cr, Co, Mn, Ni, Nb, Ta, Ti, V, W, and Zr. Co is one of the CMs with a high supply risk for both short and medium terms for advanced alloys for Gen-IV reactor systems. As global demand for stainless steel rapidly increases, supplies for minerals such as nickel, manganese, and chromium become more critical. To shift peak mineral production and delay the scarcity of alloying minerals, the recycling rate of minerals needs to increase. However, the natural sources for these minerals are exhaustible, and Hubbert's model projects peak production for these minerals between 2020 and 2050.

The outcome and conclusions from the AMMT program CM studies are described in two strategic reports issued to date (Hartmann et al., 2022, 2023) and in detailed experimental design and execution regarding (1) the replacement of high-risk CMs such as cobalt and subsequently niobium with more abundant minerals (Burns et al., 2024) and (2) the minimization and utilization of CM waste streams (van Rooyen et al., 2024). This report provides a summary of the AMMT program's work as detailed in the abovementioned body of work. This report provides a detailed summary, in the bullets bellow, of the full projects' main findings:

- The AMMT strategy to decrease nuclear material vulnerability due to CM supply and the economic impact focuses on (1) Co, as a short-term (2020–2050) and medium-term (2025–2035) high supply risk, and (2) Ni, a near-critical material for the near term, but a high critical material for the medium term (2025–2035).
- Recycling 70% of certain alloying metals can delay their peak production by about 50 years. Experimental feasibility studies show that the recycling of solid waste through the consolidation of machining chips or offcuts and liquid waste metal recovery through aqueous separation can have positive impacts for nuclear material supply risks. This process shows the benefit of a full circular process, with no waste of CMs, and can be repeated several times. Friction stir consolidation (FSC) has been considered in this work because it has been reported to be a reproducible process and can refine the microstructure without producing unwanted textures, thereby reducing anisotropy.

- Three nuclear grade materials have been processed by FSC to evaluate the feasibility of this process for the efficient recovery of materials: (1) Alloy 709 (Fe–20Cr–25Ni with other minor elements such as Mo, Mn, Nb, N, C, etc.) is a 20Cr–25Ni austenitic grade stainless steel and has been considered for sodium-cooled fast reactors (SFRs). (2) Alloy 316H is a high carbon modification of Alloy 316 developed for use at elevated temperatures. The alloy is used for structural and pressure vessel applications at temperatures above 500°C and is currently considered for multiple reactor types. (3) Alloy 617 is a nickel–chromium–cobalt alloy that has many outstanding properties such as high-temperature oxidation resistance and corrosion resistance in various corrosive aqueous environments. It is the sixth material cleared by the Boiler and Pressure Vessel Code (BPVC) for use in high-temperature nuclear reactors.
- In the FSC process, metal chips of all three alloys were successfully solid-state-consolidated into dense products after limited optimization of process parameters. The extents of consolidation in A709 and Inconel 617 (IN617) are higher compared to that in 316H. Further, the real-time density evolution was measured, revealing the mechanism of the consolidation process, which will allow for future upscaling benefits. In all three alloys (A709, 316H, and IN617) that were FSC-processed, the grains are refined in size and nearly equiaxed, removing any anisotropy from the starting material. In A709, the grain size decreased by nearly 80 percent (from 10 to 2 μm). Similarly, the grain size reduction was nearly 88 percent in IN617 (from 10.2 to 1.2 μm). Subsequently, the hardness of the FSC product substantially increased because of grain boundary strengthening (Hall–Petch relationship).
- Ionic metal–organic framework (iMOF)-based adsorbents are successfully designed for CM extraction from aqueous solution, thereby providing a pathway for future upscaling for salvaging dissolved Ni ions. This research has achieved its goal of showing the impact of novel applications of recycling technologies for solid and liquid wastes that can be upscaled for application. The uptake properties of the iMOFs were evaluated in terms of the adsorption capacity, removal efficiency, and kinetics. The adsorption capacity of iMOFs towards nickel reaches 34.1 mg/g with a removal efficiency of >99.9%. Notably, complete removal of nickel takes place within 5 min, which is much faster compared to other adsorbents. Moreover, the iMOFs can simultaneously coextract multiple minerals, proving their effectiveness as general adsorbents.
- The design of nuclear materials without critical elements as alloying elements is a part of the nuclear materials strategy to overcome CM scarcity. In this report, two approaches are evaluated—namely, (1) the replacement of critical elements as alloying elements in nuclear materials and (2) the design of new alloys that do not contain CMs as an alloying element.
- For the first approach, IN617 has been selected as an alloy system to substitute its high Co concentration using noncritical Mn. IN617 is an alloy system that has been recently ASME-code certified for high-temperature nuclear systems (U.S. Office of Nuclear Energy, 2020); therefore, it was used as a feasibility study. A computational feasibility study of compositional changes to IN617 with simulation-generated stress–strain curves determined the impact that Co replacement with Mn has on the alloy's mechanical properties (e.g., tensile strength). For select compositions, phase diagrams were calculated, and given the promising and similar results compared to the original alloy, experimental verification was performed. The phase diagrams and tensile simulations suggest that Mn substituted for Co will yield similar tensile strength and phase stability. The composition with the best combination of simulated oxygen penetration and tensile strength was down-selected for experimental fabrication and characterization. Two different fabrication methods were used to fabricate alloy samples: (1) casting and (2) friction stir consolidation and alloying. The samples were then characterized using scanning electron microscopy (SEM) energy dispersive spectroscopy (EDS), X-ray diffraction (XRD) (casting alloy only) and Vickers hardness. IN617-M1 shows considerable

promise as a material, particularly when subjected to advanced processing methods like friction stir alloying (FSA), due to the grain refinement as an additional strengthening mechanism.

- For the second approach evaluated herein, multiobjective Bayesian optimization (MOBO) techniques were employed to design novel alloys for nuclear applications that do not contain the CMs nickel and cobalt while maximizing alloy yield strength and hardness. The material system within which new compositions were developed for this study is Fe–Cr–Cu–Al–Nb–Ta–Ti–V–Zr–Mo–W–Mn. Predictions made through MOBO need to be verified by conducting simulations using molecular dynamics and by experimentally producing the alloys and measuring their hardness and yield strength values.

In conclusion, a significant number of alloying elements of nuclear materials are classified as scarce CMs with high economic risk and supply chain disruptions, and the supply of critical raw materials is highly concentrated, posing risks to supply chain reliability, affordability, and sustainability. The feasibility experimentation shows that it is viable to design new material types minimize the current waste of these alloying elements. The report further shows that action needs to be considered early in the design and development stages to minimize the impact on both the current fleet and new reactor types. Moreover, research successfully showcased novel recycling technologies for solid and liquid waste, with promising upscaling opportunities for various industrial applications.

Two publications submitted to *Materialia* and *Journal of Coordination Chemistry*, two conference presentations [MS&T2024, ASTM International Conference on Advanced Manufacturing 2024 (ICAM2024)], and four technical reports (this report included) demonstrate the outcomes and impacts to date from this work.

Acknowledgments

The research presented here was supported by the Advanced Materials and Manufacturing Technology (AMMT) program of the DOE Office of Nuclear Energy. PNNL is a multi-program national laboratory operated for the U.S. Department of Energy (DOE) by Battelle Memorial Institute under Contract No. DE-AC05-76RL01830. Dr. Teresa Lemmon and Marie Swita at PNNL are thanked for their support on elemental analysis as part of the Ni separation study, and Mr. Alan Schemer-Kohrn is thanked for his assistance with XEDS analysis of the as-cast IN617-M1 sample. We thank the Advanced Reactor program for the offcuts of plate material of Alloy 617 and Alloy 709 [Dr. Sam Sham (NRC, previously INL), Dr. Yanli Wang (ORNL), Dr. Xuan Zhang (ANL)]. Isaiah P. Steinke is thanked for technical editing, and Dr. Richard Daniel is thanked for peer review of this report.

The following researchers contributed to the reporting of the research performed under the AMMT program's critical minerals project and are specifically acknowledged for their work on the summary and strategic tasks.:

- Critical Minerals Evaluation Report, PNNL-33356, M3CR-22PN0401018, September 2022, Thomas Hartmann, Stuart Maloy, Isabella van Rooyen
- Strategic Plan: Decrease Critical Minerals Waste through Enabling Advanced Manufacturing Techniques, Revision 1, PNNL-34225, M2CR-22PN0401011, July 2023, Thomas Hartmann, Praveen K. Thallapally, Isabella van Rooyen.
- Nuclear Energy Critical Material Waste Minimization Enabled by AM Techniques, PNNL-36049, M3CR-22PN0401013, May 2024, IJ van Rooyen, T Wang, S Meher, D Garcia, P Thallapally, M Nartu, J Dos Santos, QRS Miller, C Silva, T Hartmann, SHR Shin.
- Development Results on Replacement Materials for Current Scarce or High Supply Chain Risk Materials, PNNL-36491, M3CR-22PN0401015, August 2024, Carolyne Burns, Ankit Roy, Steven Livers, Subhashish Meher, Asif Mahmud, David Garcia, Pratikshya Meher, Benjamin Lund, Mohan Nartu, Jorge Dos Santos, Thomas Hartman, Isabella van Rooyen.

Acronyms and Abbreviations

AM	advanced manufacturing
AMMT	Advanced Materials and Manufacturing Technology
API	application programming interface
ASME	American Society of Mechanical Engineers
BAU	business as usual
BET	Brunauer–Emmett–Teller
BPVC	Boiler and Pressure Vessel Code
BSE	backscattered electron
CM	critical mineral
DMA	dimethylammonium
DMACl	dimethylammonium chloride
DOE	U.S. Department of Energy
EBSD	electron backscatter diffraction
EDS	energy dispersive spectroscopy
EJ	exajoule(s) or 1×10^{18} J
fcc	face-centered cubic
FSA	friction stir alloying
FSC	friction stir consolidation
FSW	friction stir welding
GAN	generative adversarial network
GB	grain boundary
GFR	gas-cooled fast reactor
GWe	gigawatt(s) electric
HCl	hydrochloric acid
HEA	high entropy alloy
HVI	hypervolume improvement
ICP	inductively coupled plasma
iMOF	ionic metal–organic framework
LAMMPS	Large-scale Atomic/Molecular Massively Parallel Simulator
MD	molecular dynamics
MI	mutual information
ML	machine learning
MMT	million metric tons
MOBO	multiobjective Bayesian optimization
MOF	metal–organic framework
MPEA	multiprincipal element alloy

MSR	molten salt reactor
MWe	megawatt(s) electric
NAS	National Academy of Sciences
NSGA	nondominated sorting genetic algorithm
NZE	net-zero carbon economy
PJ	petajoule(s) or 1×10^{15} J
PNNL	Pacific Northwest National Laboratory
ppt	precipitate(s)
PV	photovoltaic
PXRD	powder X-ray diffraction
qEHVI	q-expected hypervolume improvement
qNEHVI	q-noisy expected hypervolume improvement
ReLU	ectified linear unit
SEM	scanning electron microscopy
SFR	sodium-cooled fast reactor
UCB	upper confidence bound
VEC	valence electron concentration
VHTR	very high temperature reactor
XEDS	X-ray energy dispersive spectroscopy
XRD	X-ray diffraction
YS	yield strength

Contents

Figures

Tables

1.0 Introduction

In September 2020, the U.S. government issued an executive order to address the threat to the domestic supply chain from its reliance on critical minerals (CMs) from foreign competitors and to support the domestic mining and processing industry (DOE, 2021). In this context, a national strategy on CMs was developed, which had an impact on the U.S. Department of Energy's (DOE's) vision for the decade of 2021–2031. This vision embraces science and technology to re-establish U.S. competitiveness in the CM and material supply chains by (a) scientific innovation and technologies to ensure resilient and secure CMs and maintain a domestic material supply chain, (b) building a long-term minerals and materials innovation ecosystem to foster new capabilities to mitigate CM supply chain challenges, (c) increasing private sector adoption for sustaining the domestic CM supply chain, and (d) coordinating with international partners and federal agencies to diversify global supply chains and ensure the adoption of best practices for sustainable mining and processing (DOE 2021).

The Advanced Materials and Manufacturing Technology (AMMT) program is addressing this executive order by evaluating advanced manufacturing (AM) and its impact on the demands of CMs for energy production in general and how the deployment of AM in nuclear energy will support the projected goals of the Paris Accord and further a net-zero carbon economy (NZE) by 2050. Two strategic reports have been issued by the AMMT to date (Hartmann et al., 2022, 2023), and detailed experimental design and execution have been the focus of the past year's work regarding (1) the replacement of high-risk CMs such as cobalt and niobium with more abundant minerals (Burns et al., 2024) and (2) the minimization and utilization of CM waste streams (van Rooyen et al., 2024). This report provides a summary of the AMMT program's work as detailed in the abovementioned body of work.

1.1 Background

The Paris Accord's aim is to control the level of anthropogenic global temperature increase by 2050 well below 2°C above pre-industrial levels, and in 2016, the United States became a signatory to this agreement. To achieve a "climate neutral world" by mid-century, all developed industrialized countries have heavily invested in renewable electric energy production and provide substantial incentives to promote electric battery transportation. Therefore, in recent years, renewable energy systems are set to force a huge increase in the requirements for CMs, and the energy sector will emerge as a major force in consuming CMs. In fact, renewable energy technologies are becoming the fastest-growing segment of mineral demand (IEA 2022). Nuclear energy, on the other hand, has only moderate requirements on CMs (e.g., copper, nickel, and chromium) of less than 1% of the world's supply. Global material use will more than double, from 79 billion tons in 2011 to 167 billion tons in 2060. The projected growth in materials use, coupled with the environmental consequences of material extraction, processing, and waste, is likely to increase pressure on the resource bases of the planet's economies and jeopardize economic and social gains in well-being.

CMs are essential for a range of clean energy technologies, which are experiencing rapid growth due to global policies and business agendas in recent years. Record deployment of clean energy technologies such as solar photovoltaics (PVs) and batteries is propelling unprecedented growth in CM markets, while electric car sales exceeded 10 million units in 2022. Energy storage systems experienced even more rapid growth, with capacity additions doubling in 2022 and wind power installations set to resume their upward trend. All of this has led to a significant increase in demand for CMs and increased supply pressure on all other industries. From 2017 to 2022, demand from the energy sector was the main factor behind a tripling in the overall demand for lithium, a 70% jump in demand for cobalt, and a 40% rise in demand for nickel. In 2022, the share of clean energy applications of the total demand reached 56% for lithium, 40% for cobalt, and 16% for nickel, up from 30%, 17%, and 6%, respectively, five years ago (IEA, 2023a).

Driven by rising demand and high prices, the market share of energy transition minerals doubled over the past five years, reaching USD 320 billion in 2022. Energy transition minerals, which used to be a small segment of the market, are now moving to center stage in the mining and metals industry. A combination of volatile price movements, supply chain bottlenecks, and geopolitical concerns has created a mix of risks for secure and rapid energy transitions.

The asymmetric distribution of CMs promotes supply reliability concerns associated with trade tensions and resource nationalism in all major supply countries (e.g., China, Russia, Congo, Chile, Brazil, South Africa). Commodities with the highest supply risks include cobalt, gallium, neodymium, and niobium, while the supply risks of copper, nickel, and chromium are low (Moss et al., 2011)

To meet the 2050 goal of carbon neutrality, mineral exploration must be significantly increased compared with 2018 production. The production level of CMs such as graphite, lithium, and cobalt must be scaled up as much as five times, neodymium, vanadium, and indium two times. All nickel produced is needed for scaling up clean energy production capacities. The demand for copper by energy technology will increase to between 60% and 73% of the world’s supply based on the 2015 production yield (Hund et al., 2020; IEA, 2022; Moss et al., 2011). From 1900 to 2010, metal and element output from world’s mining efforts increased approximately exponentially with a doubling time in production from 10–20 years and an average annual growth in resource extraction between 3.5% and 7% (Sverdrup and Ragnarsdottir, 2014). The exponential trend to extract CMs is alarming since in a finite Earth, all resources are finite as well, and exponential growth forever is unsustainable and inexcusable to future generations.

1.2 Sustainable Clean Energy CM Needs

Along with hydroelectric power, nuclear energy is one of the low-carbon technologies with the lowest total mineral intensity of 5,240 kg/MWe compared with 6,830 kg/MWe for solar PV, 10,215 kg/MWe for onshore wind farms, and as much as 15,410 kg/MWe for offshore wind farms (IEA 2022; Nassar and Fortier 2021). Because of the need for advanced structural materials, the energy-specific use of alloying elements such as nickel and chromium is higher in nuclear energy relative to renewable technologies. However, besides the demands for hafnium and indium used in reactor control rods, the demand for all other minerals in nuclear energy, such as Mo, Ni, W, Nb, Zr, Cd, Cr, Sn, V, Cu, Pb, Ti, and Co, is far below 1% of total annual production (Moss et al., 2011). The deployment of more advanced Gen-IV reactor technologies will however increase and eventually double nuclear energy’s mineral demand since more alloying metals are required to allow for enhanced materials of high-temperature strength and improved resistance to corrosion.

For the year 2050, the worldwide installed nuclear energy capacity is projected to be 792 GWe maximum (IAEA, 2021), the installed capacity of solar PVs is forecasted to be 1,600 GWAC (US Office of Energy Efficiency & Renewable Energy, 2024) and the capacity of wind energy is estimated to be as high as 5,900 GW (Richard, 2021). The installation of additional nuclear energy capacity will require 0.2% of the copper supply, 7.5% of nickel, and 0.8% of chromium relative to the 2021 production yields applying Gen-III+ technology. For solar PVs, 18% of the copper supply is needed. The installation of the projected wind energy capacity will require 104% of copper, 83% of nickel, 21% of manganese, and 6.3% of the chromium production yield. The demand for critical structural metals for clean energy technologies by 2050 is however achievable without enhancing mineral exploration and mining capacity. Even if peak mining of most CMs will decline by mid-century, the overall mineral supply can be met by intensifying recycling efforts and a peak supply shift by 50+ years. Optimizing mineral recycling is indispensable to meet the goals of the Paris Accord and to mitigate supply risks.

The rapid growth in nuclear capacity by 2.365% annually requires the installation of 21 nuclear power stations between 2049 and 2050 and a demand of 840,000 tons of steel for nuclear energy, about 0.028% of the world's steel supply in 2050. If all steel used in these 21 nuclear plants is produced by AM methods, an energy savings of 7 to 39 petajoules (PJ) could be achieved. If we realistically consider a contribution of 10% AM for all structural materials in nuclear technology, the energy savings is still considerable: about 0.7 to 4 PJ. An average 1,000 MWe power plant produces 31.5 PJ annually. This is equivalent to the maximum energy savings possible if all structural alloys of the 21 nuclear plants are produced by AM.

1.3 Scope of This Report

Nuclear materials without a critical mineral (CM) as an alloying element are rare; therefore, the strategic aim of this project (Section 2.0) was to identify the CMs relevant to nuclear energy, specifically those relevant to the alloying elements of nuclear materials for the current fleet and next-generation nuclear reactors. From these data, two main experimental feasibilities were defined and executed as described in Sections 3.0 and 5.0, respectively. Recommendations are provided for mitigation strategies to decrease the impact of CM scarcity in Section 6.0. Lastly, all publications completed as part of this work will be provided in Section 7.0.

2.0 Strategy

Two primary aspects were considered at the onset of the study—namely, the minerals as elements in typical nuclear materials and the manufacturing methods that are currently used for future optimization or modification to decrease waste. Additionally, the widespread implementation of AM technologies can lead to a noticeable reduction in the global energy demand. Extrapolated to the global energy demand in the (net-zero) year 2050 of 513 exajoules (EJ), a reduction by up to 138 EJ/year, equivalent to 27% of the global demand seems achievable (Verhoef et al., 2018). The 2022 final list of CMs includes the following 50 minerals: aluminum, antimony, arsenic, barite, beryllium, bismuth, cerium, cesium, chromium, cobalt, dysprosium, erbium, europium, fluorspar, gadolinium, gallium, germanium, graphite, hafnium, holmium, indium, iridium, lanthanum, lithium, lutetium, magnesium, manganese, neodymium, nickel, niobium, palladium, platinum, praseodymium, rhodium, rubidium, ruthenium, samarium, scandium, tantalum, tellurium, terbium, thulium, tin, titanium, tungsten, vanadium, ytterbium, yttrium, zinc, and zirconium.

2.1 CMs for Nuclear Materials

The list of CM elements was paired with Gen-IV reactor types (Hartmann et al., 2022) (Table 1), showing the vulnerability of reactor manufacturing, sustainability, and the influence on growth potential due to material availability.

Table 1. Pairing of the listed CMs with the alloys to be used in Gen-IV reactor types [adapted from (Hartmann et al., 2022)].

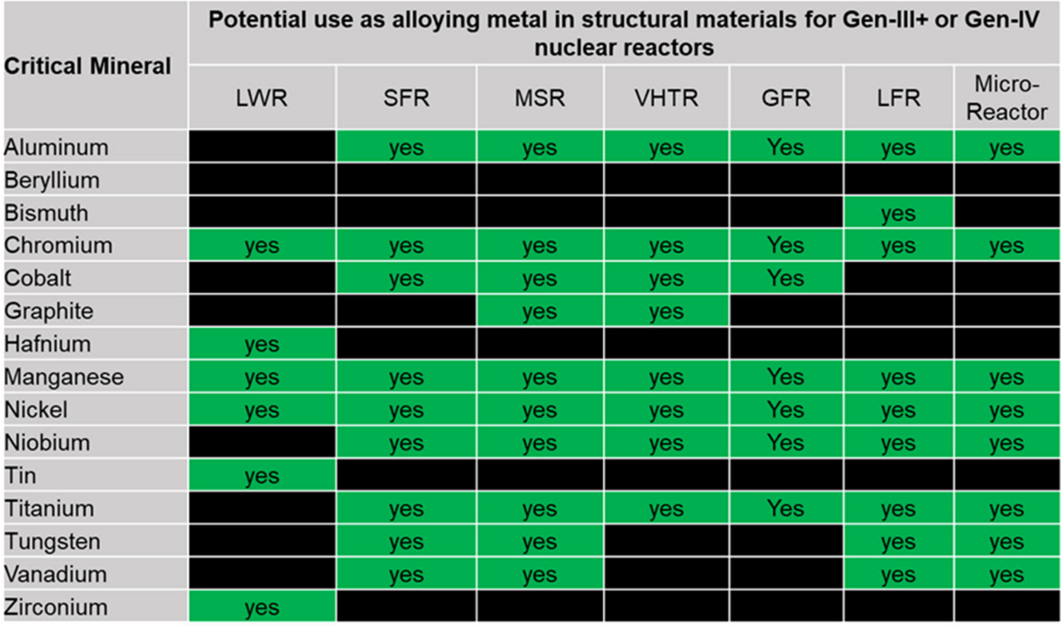

Critical Mineral	**Potential use as alloying metal in structural materials for Gen-III+ or Gen-IV nuclear reactors**						
	LWR	SFR	MSR	VHTR	GFR	LFR	Micro-Reactor
Aluminum	■	yes	yes	yes	Yes	yes	yes
Beryllium	■	■	■	■	■	■	■
Bismuth	■	■	■	■	■	yes	■
Chromium	yes	yes	yes	yes	Yes	yes	yes
Cobalt	■	yes	yes	yes	Yes	■	■
Graphite	■	■	yes	yes	■	■	■
Hafnium	yes	■	■	■	■	■	■
Manganese	yes	yes	yes	yes	Yes	yes	yes
Nickel	yes	yes	yes	yes	Yes	yes	yes
Niobium	■	yes	yes	yes	Yes	yes	yes
Tin	yes	■	■	■	■	■	■
Titanium	■	yes	yes	yes	Yes	yes	yes
Tungsten	■	yes	yes	■	■	yes	yes
Vanadium	■	yes	yes	■	■	yes	yes
Zirconium	yes	■	■	■	■	■	■

Within the next decade, commodity prices for CMs crucial for steel production will see a sharp surge since lower ore grade qualities will be mined and refined and higher volumes of ore-bearing rocks must be processed for comparable metal yields. The large-scale deployment of AM in industrialized countries and China, specifically within the nuclear industry, may result in significant materials and cost savings, allowing for fast prototyping, which can provide nuclear materials with superior mechanical properties and corrosion resistance. Here, the adoption of AM materials for critical parts within the nuclear industry will contribute to the economic feasibility of manufacturing processes and therefore enhance the deployment of AM materials for nuclear energy production. Estimates must be revised considering the use of Gen-IV technology for primary energy production to reduce carbon emissions by 4,000 million metric tons (MMT).

Based on a methodology developed by the National Academy of Sciences (NAS) that accounts for the impacts of supply disruption and supply risk, along with the importance to (decarbonized clean) energy, elements are categorized according to supply risk:

- Short-term (2020–2025) high supply risk: seven CMs—namely, cobalt (Co), dysprosium (Dy), gallium (Ga), natural graphite, iridium (Ir), neodymium (Nd), and terbium (Tb). There are also nine near-critical (electrical steel, fluorine, lithium, magnesium, nickel, platinum, praseodymium, silicon carbide, and uranium) and seven noncritical (aluminum, copper, manganese, phosphorous, silicon, tellurium, and titanium) materials.
- Medium-term (2025–2035), there are thirteen CMs (cobalt, graphite, gallium, platinum, magnesium, silicon carbide, lithium, nickel, dysprosium, iridium, neodymium, praseodymium, and terbium), six near-critical materials (copper, electrical steel, silicon, uranium, aluminum, and fluorine), and four noncritical materials (manganese, titanium, phosphorus, and tellurium) (Bauer et al., 2023).

From the list of 50 CMs, the focus of earlier AMMT program evaluations was the CMs related to advanced alloys selected for deployment in Gen-IV reactor systems. Among the minerals identified as most important to the nuclear industry (e.g., Al, Cr, Co, Mn, Ni, Nb, Ta, Ti, V, W, and Zr for advanced alloys for Gen-IV reactor systems), cobalt (Co) is one of the CMs with a high supply risk for both short and medium terms (Hartmann et al., 2022).

Hubbert's model, developed to predict peak production and scarcity of natural resources, projects that the production of industry-crucial commodities such as gold, silver, copper, iron, platinum group metals, indium, zinc, molybdenum, and nickel will peak at the year 2050 or well before (Sverdup et al., 2013; Sverdup and Ragnarsdóttir, 2014). The most important alloying metals for stainless steel—nickel, manganese, and chromium—run the risk of becoming scarce long before iron will. Stainless steel, an iron–carbon alloy with nickel (Ni), manganese (Mn), and chromium (Cr), is one of the most important materials in the world. Owing to its excellent properties such as resistance to corrosion, ductility, and toughness, stainless steel has been widely used in many industrial applications. As global demand for stainless steel increases, supply for Ni, Mn, and Cr becomes more critical. However, the natural sources of these minerals are exhaustible, and Hubbert's model projects peak productions for these minerals between 2020 and 2050 (Figure 1) (Sverdup and Ragnarsdóttir, 2014). Nickel production will peak between 2025 and 2030, while peak production for chromium has already happened in 2020. Hubbert's peak production for molybdenum is expected between the year 2050 and year 2070, and the peak production for cobalt is around 2025.

A shortage of the minerals in supply can be mitigated by recycling minerals. It has been reported that the time for mineral scarcity can be significantly delayed depending on recycling rates (Table 2) (Sverdup et al., 2013). For example, Ni and Mn have burn-off times of less than 45 years with current recycling rates, and the burn-off time can be delayed to more than 400 years with 90% improved recycling rates. Enhanced recycling is essential to shift CM peak production and delay the scarcity of alloying minerals.

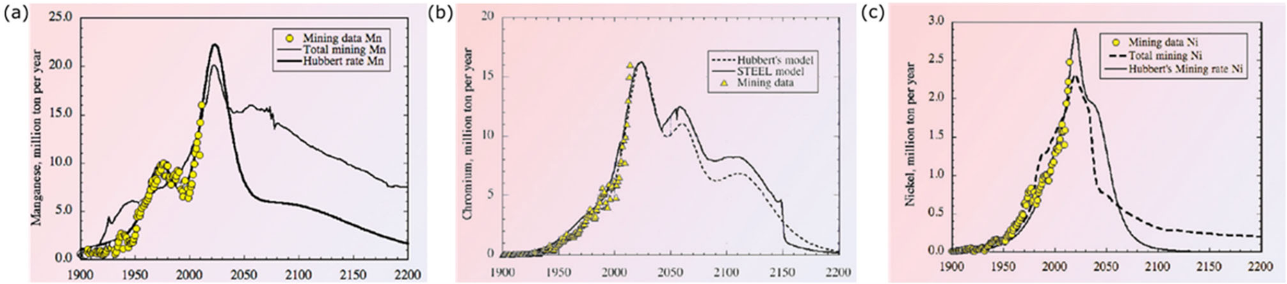

Figure 1. Production curves for (a) Mn, (b) Cr, and (c) Ni using Hubbert's model and the system dynamics STEEL model (Sverdup and Ragnarsdóttir, 2014).

Table 2. Estimated burn-off times for minerals depending on different improved recycling rates in the market. BAU = business as usual with recycling as today. All values are years counted from 2010 and forwards (Sverdup et al., 2013).

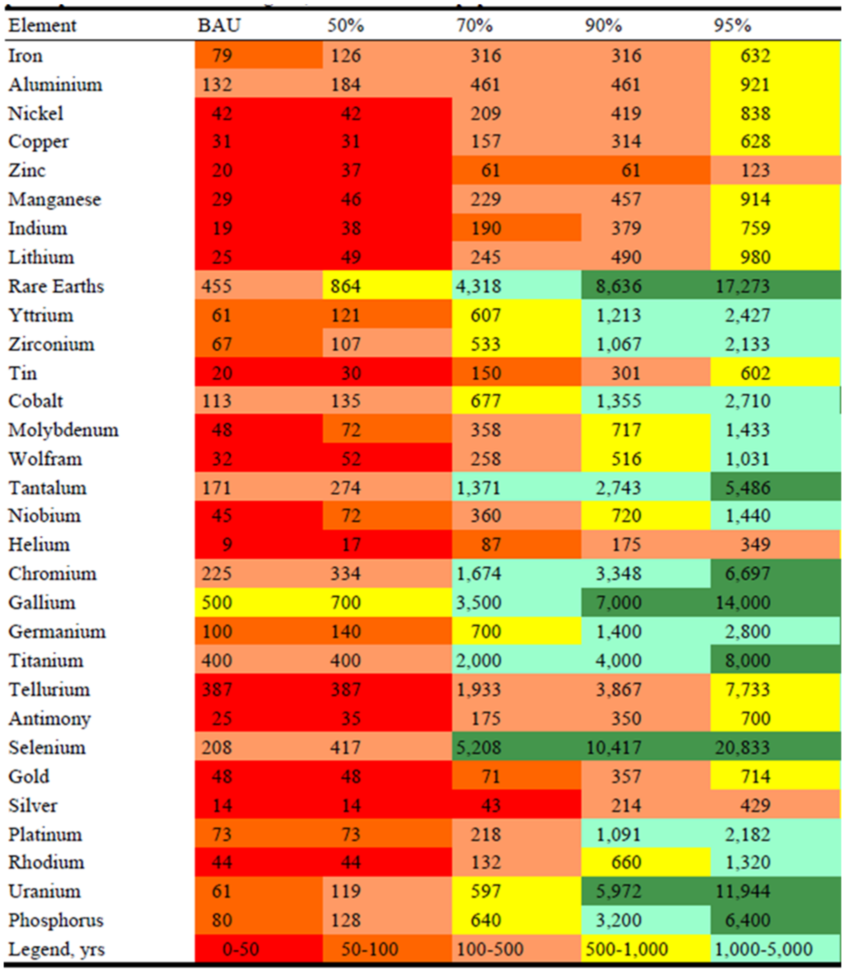

Element	BAU	50%	70%	90%	95%
Iron	79	126	316	316	632
Aluminium	132	184	461	461	921
Nickel	42	42	209	419	838
Copper	31	31	157	314	628
Zinc	20	37	61	61	123
Manganese	29	46	229	457	914
Indium	19	38	190	379	759
Lithium	25	49	245	490	980
Rare Earths	455	864	4,318	8,636	17,273
Yttrium	61	121	607	1,213	2,427
Zirconium	67	107	533	1,067	2,133
Tin	20	30	150	301	602
Cobalt	113	135	677	1,355	2,710
Molybdenum	48	72	358	717	1,433
Wolfram	32	52	258	516	1,031
Tantalum	171	274	1,371	2,743	5,486
Niobium	45	72	360	720	1,440
Helium	9	17	87	175	349
Chromium	225	334	1,674	3,348	6,697
Gallium	500	700	3,500	7,000	14,000
Germanium	100	140	700	1,400	2,800
Titanium	400	400	2,000	4,000	8,000
Tellurium	387	387	1,933	3,867	7,733
Antimony	25	35	175	350	700
Selenium	208	417	5,208	10,417	20,833
Gold	48	48	71	357	714
Silver	14	14	43	214	429
Platinum	73	73	218	1,091	2,182
Rhodium	44	44	132	660	1,320
Uranium	61	119	597	5,972	11,944
Phosphorus	80	128	640	3,200	6,400
Legend, yrs	0-50	50-100	100-500	500-1,000	1,000-5,000

Enhancements in quality and yield of CM recycling and the recovery of CMs from solid and industrial waste streams are needed to enhance supply security for stainless-steel production and to shift the time to scarcity for society to future years to achieve an NZE by 2050.

2.2 Strategy for Decreasing Nuclear Material Vulnerability Due to CMs

As a part of the DOE's focus on CMs, increasing manufacturing efficiency, identifying better substitutes, and improving the recycling and recovery of CMs are important aspects that need focus using both experimental and computational efforts. Experimental feasibility studies were identified as part of the strategy to decrease nuclear material vulnerability due to CM supply and economic impacts on the following elements: (1) Co, as a short-term (2020–2050) and medium-term (2025–2035) high supply risk, and (2) Ni, a near-critical material for the near term but a high critical material for the medium term (2025–2035). Two detailed strategic reports have been issued by the AMMT program to date (Hartmann et al., 2022, 2023), and detailed experimental design and execution have been the focus of the past year's work regarding (1) the replacement of high-risk CMs such as cobalt and niobium with more abundant minerals (Burns et al., 2024) and (2) the minimization and utilization of CM waste streams (van Rooyen et al., 2024). Figure 2 shows a schematic of the CM strategy for nuclear materials as adopted during the early stages of this project (Hartmann et al., 2022).

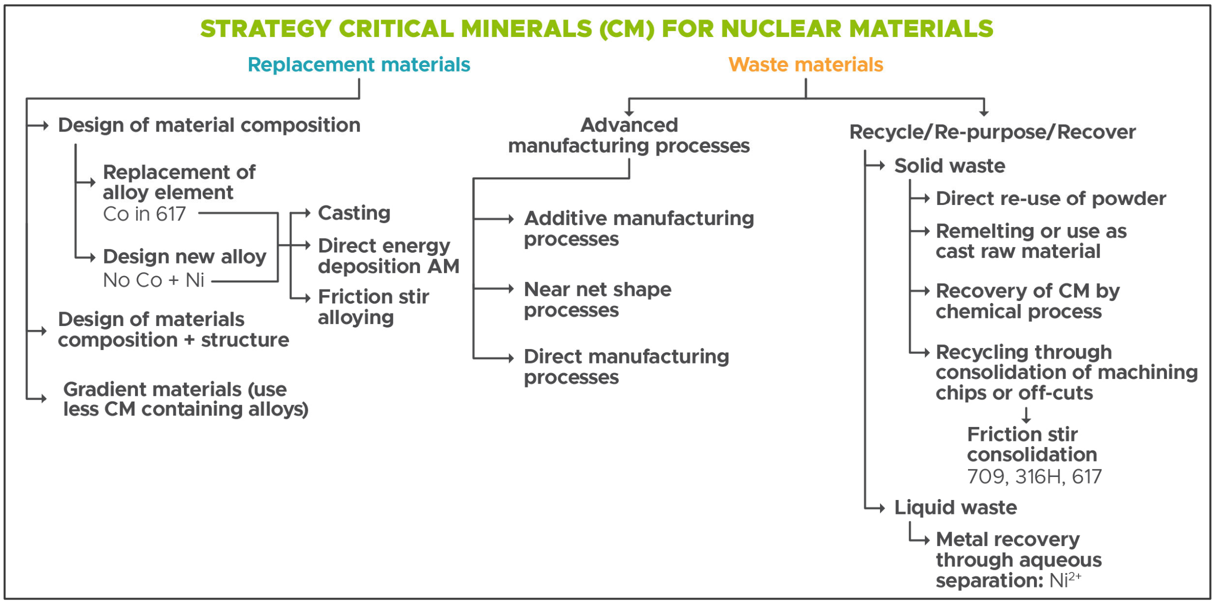

Figure 2. Schematic of the CM strategy for nuclear materials as developed during this study.

3.0 Nuclear Energy CM Waste Minimization Enabled by AM Techniques

A summary of Milestone Report M3CR-22PN0401011, “Strategic Plan: Decrease Critical Minerals Waste through Enabling Advanced Manufacturing Techniques,” is presented in this section.

These experimental studies show that the recycling of solid waste through the consolidation of machining chips or offcuts and liquid waste metal recovery through aqueous separation can have positive impacts for nuclear material supply risks. The use of novel methods to separate and recover CMs from solid and liquid industrial waste streams is needed, which supports the goal of enhancing the quality and yield of CMs.

3.1 Solid Waste: Recycling through the Consolidation of Machining Chips or Offcuts

The solid-state recovery or recycling of CMs involves the use of alloy shavings or machined chips as the starting materials for friction stir consolidation (FSC) to produce dense billets that can be extruded to different useful dimensions (Figure 3). This process shows the benefit of a full circular process, with no waste of CMs, and can be repeated several times. FSC has been considered in this work because it has been reported to be a reproducible process and can refine the microstructure without producing unwanted textures, thereby reducing anisotropy (Catalini et al., 2013; Jiang et al., 2017; Komarasamy et al., 2021). It was also reported to produce favorable secondary precipitates such as dispersoids in ODS MA956 during friction consolidation (Catalini et al., 2013).

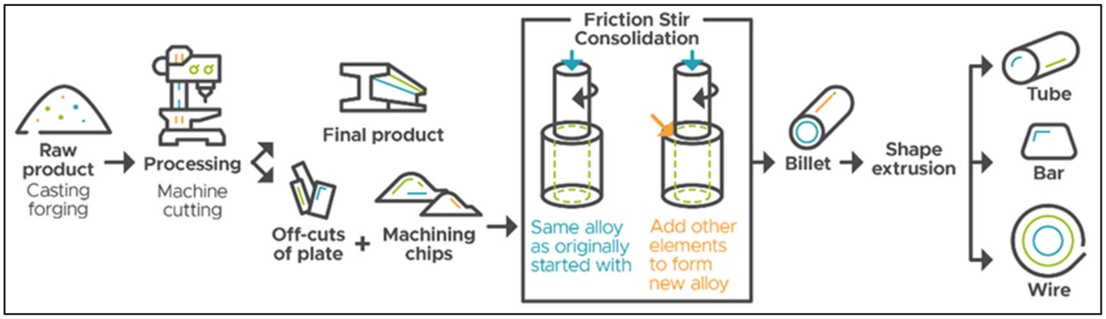

Figure 3. Schematic of recycling by FSC of alloy machining chips to produce alloy billets.

Three nuclear grade materials have been processed by FSC to evaluate the feasibility of this process for the efficient recovery of materials (van Rooyen et al., 2024).

A709: Alloy 709 (Fe–20Cr–25Ni with other minor elements such as Mo, Mn, Nb, N, C, etc.) is a 20Cr–25Ni austenitic grade stainless steel and has been considered for sodium-cooled fast reactors (SFRs). Alloy 709 is a niobium-strengthened steel owing to the presence of nanoscale carbides (Upadhayay et al., 2018). It has a greater creep strength and better swelling resistance under self-ion irradiation than stainless steel 316 (Kim et al., 2019) and Grade 91 (Smith et al., 2017). Thermal properties such as the thermal conductivity and specific heat capacity of Alloy 709 have been found to be well within the values reported for other high Cr and high Ni austenitic steels (Smith et al., 2017).

316H: Alloy 316H is a high carbon modification of Alloy 316 developed for use at elevated temperatures. The alloy is used for structural and pressure vessel applications at temperatures above 500°C (Mehmanparast et al., 2014). The higher carbon content of 316H imparts higher tensile and yield strengths than those of 316/316L. The corrosion resistance of Alloy 316H has been observed to be comparable to that of Alloy 316/316L.

IN617: Alloy 617 is a nickel–chromium–cobalt alloy that has many outstanding properties such as high-temperature oxidation resistance and corrosion resistance in various corrosive aqueous environments (Mankins et al., 1974). It is the sixth material cleared by the Boiler and Pressure Vessel Code (BPVC) for use in high-temperature nuclear reactors.

3.1.1 FSC Process

The FSC experiments were performed using the friction stir welding (FSW) machine at Pacific Northwest National Laboratory (PNNL), depicted in Figure 4. Two tooling setups, MP159 and W–Re, were utilized. Initial experiments with A709 steel chips indicated that the consolidated material tends to adhere to the MP159 tool. Consequently, the W–Re tooling setup was employed for the subsequent experiments. There are three critical process variables during friction consolidation experiments: the loading force, rotation rate, and processing time. Additionally, the tool/chip interface can be monitored during friction consolidation, making the temperature a crucial parameter in determining the extent of consolidation. It is important to note that the temperature is influenced by the combination of the loading force and rotation rate. These selected metals were machined into chips for the FSC experiments.

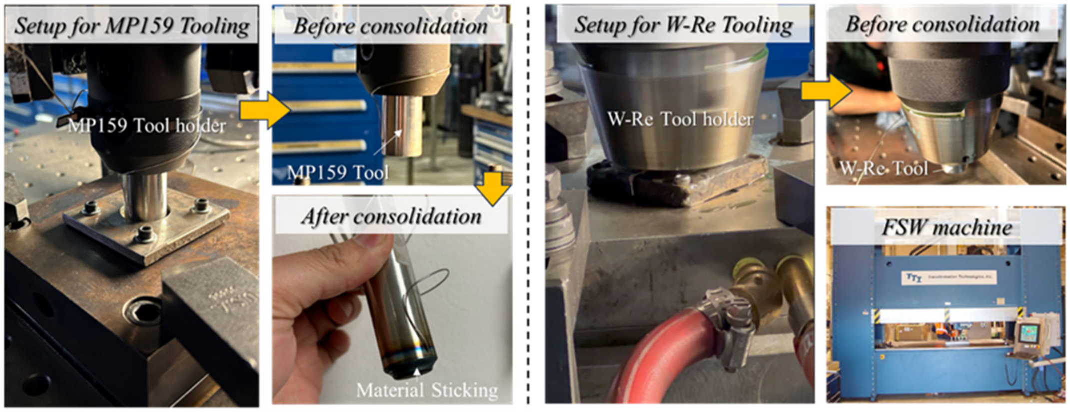

Figure 4. Friction consolidation setup. Left: MP159 tooling setup; right: W–Re tooling setup. The machine used for this study is the FSW machine (as shown in the right bottom).

3.1.2 FSC of Alloy 709

From the five experiments performed, it became evident that the loading force played a significant role in consolidating the materials. As the loading force increased from 2 kN to 20 kN, the rotation rates were reduced from 300–350 RPM to 100 RPM in Run #5 to maintain a consistent tool/chip interface temperature of 850°C. (see Table 3 for the critical parameters for A709 FSC experiments). The fully consolidated layer thickness increases from Run #3 to Run #5; hence, it can be reasonably inferred that the loading force has a more significant impact on the consolidation level compared to the processing time.

Table 3. Critical parameters for the friction consolidation of A709 steel chips.

Run #	Weld #	Tool	Loading (kN)	Rotation rate (RPM)	Temperature (°C)	Processing time (s)
1	2023-10-28-#004	MP159	4–8	500	More than 1000	40
2	2023-10-28-#005	W–Re	2–4	150–200	Up to 450	120
3	2023-10-28-#006	W–Re	2–4	300–350	Up to 850	830
4	2024-04-11-#002	W–Re	10	150	Up to 850	650
5	2024-04-12-#000	W–Re	20	100	Up to 850	320

Figure 5(a) shows the electron backscatter diffraction (EBSD) orientation map that reveals the grain structure of the FSC A709 sample. The grains appear to be equiaxed and refined, and the average grain size of the as-received A709 sample is nominally 10 µm, while it is nominally 2 µm for the friction-consolidated samples. The range of grain sizes is also at the higher end for the as-received sample compared to the friction-consolidated samples. Microhardness data collected for the as-received and FSC samples are shown in Figure 5(b). The hardness of the friction-consolidated sample varies from 246 to 287 HV, with variations corresponding to the locations of indentation in the sample. The as-received sample had an average hardness value of 194 ± 3 HV with hardness values in the range of 186–201 HV. This higher hardness of the friction-consolidated samples can primarily be due to the smaller grain size of the friction-consolidated samples, in agreement with the Hall–Petch relationship (Hall 1951).

An optical microscopy image of the cross section of a friction-consolidated A709 sample (Run #5) is shown in Figure 6(a). From this image, the middle part of the consolidated product shows no significant pores or defects. Consolidation is observed to be lower towards both ends. Figure 6(b) shows a montage of scanning electron microscopy (SEM) images collected from the dense consolidated part enclosed by the black box in Figure 6(a). This area was analyzed by SEM, and images at different magnifications were collected. The grains from all areas appear to be equiaxed and finer compared to those in the as-received A709 sample. Further, grain boundary precipitates are retained in the FSC product.

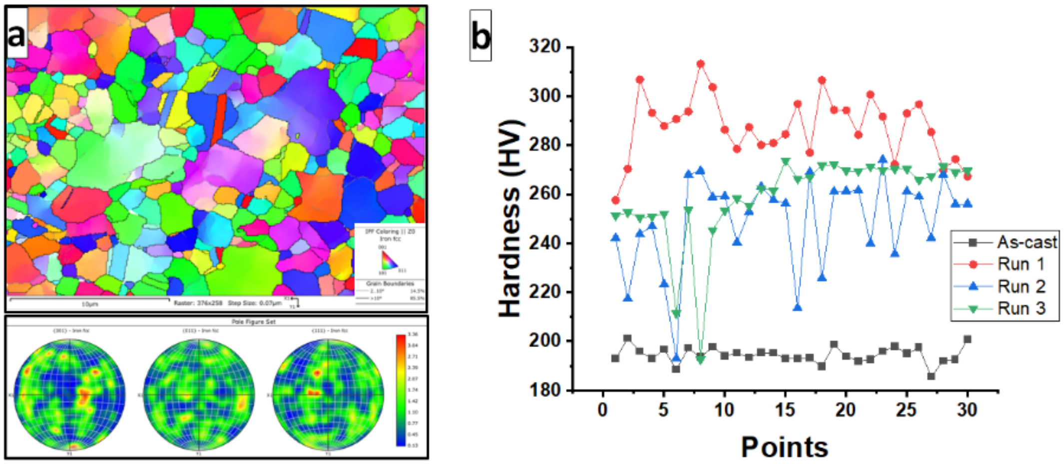

Figure 5. (a) EBSD map of FSC A709 showing the finer and equiaxed grain structure and (b) hardness plot of the as-received and FSC A709 samples.

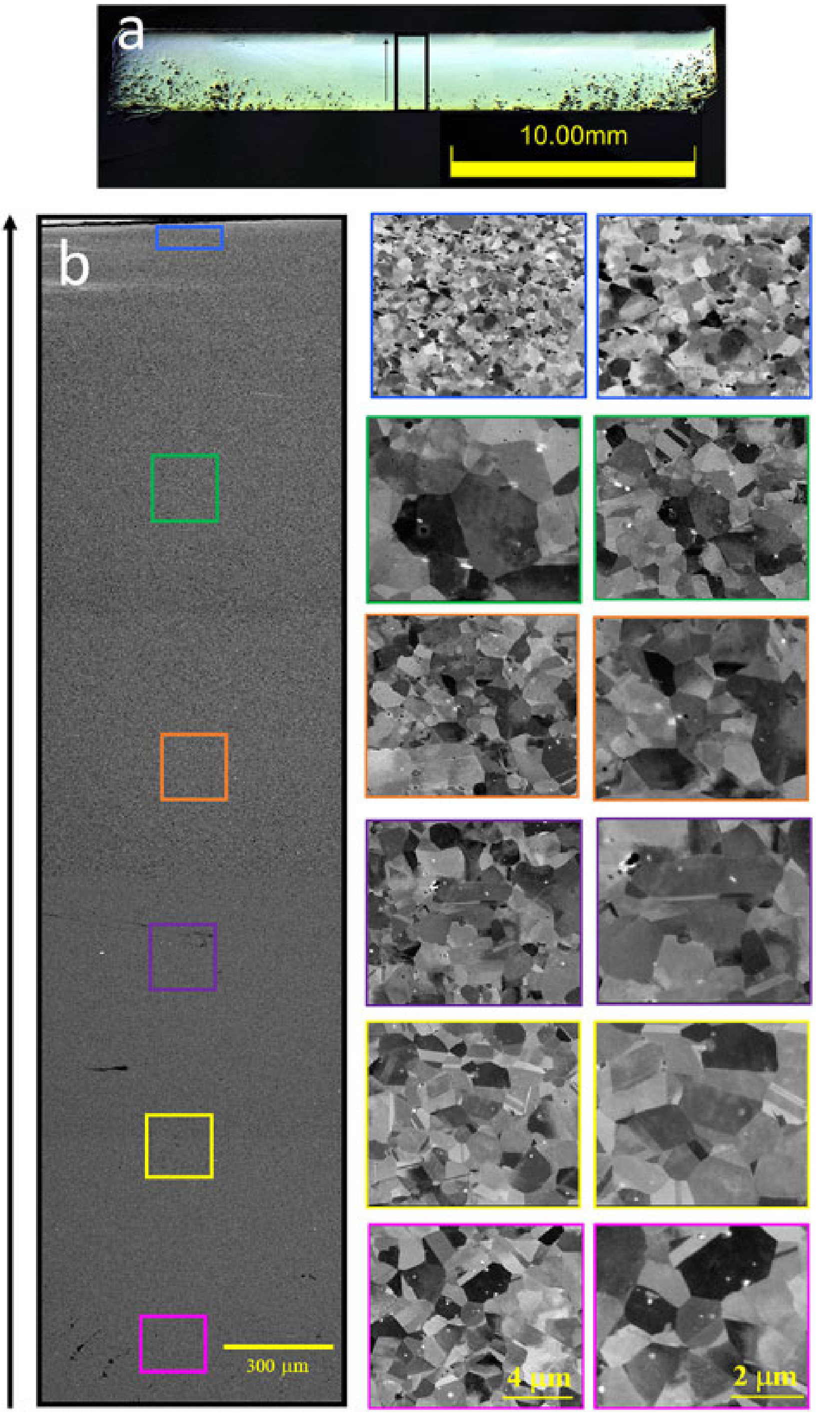

Figure 6. (a) Optical image of an FSC A709 sample. The black rectangle in (a) indicates the location of the SEM images in (b).

3.1.3 FSC of Alloy 316H

Three runs of friction consolidation for 316H steel chips were conducted, with the critical parameters listed in Table 4. As the loading force increased from 20 kN to 30 kN, the rotation rates were reduced from 100–110 RPM to 70–100 RPM to maintain a consistent tool/chip interface temperature of 850°C. For the 3rd experiment (Run #3), a low rotation rate range was selected to reduce the tool/chip interface temperature and test the viability of the low-temperature friction consolidation concept. The proposed mechanism implies that “harder” chips could transfer the load to the bottom chips more effectively. However, the results indicate that low-temperature friction consolidation negatively impacts the compaction level, as evidenced by the outcomes of Run #3.

Table 4. Critical parameters for the friction consolidation of 316H steel chips.

Run #	Weld #	Tool	Loading (kN)	Rotation rate (RPM)	Temperature (°C)	Processing time (s)
1	2024-05-08-#000	W–Re	20	100–110	Up to 850	420
2	2024-05-08-#001	W–Re	30	70–100	Up to 850	420
3	2024-05-08-#002	W–Re	30	35–50	Up to 650	420

An optical microscopy image of the cross section of a friction-consolidated 316H sample (Run #2) is shown in Figure 7(a). From this image, the top part of the middle region of the consolidated product shows no significant pore spacing or defects. However, the extent of consolidation appears to be lower compared to that in A709. The consolidation of 316H chips is observed to be even lower towards both ends. Figure 7(b) shows a montage of SEM images collected from the dense consolidated part indicated by the black line in Figure 7(a). This area was analyzed by SEM, and images at different magnifications were collected. Further, grain boundary precipitates are retained in the FSC product. The lack of consolidation towards the lower end of the samples is visible in the SEM images.

Figure 8 shows energy dispersive spectroscopy (EDS) maps of a certain area of the FSC 316H sample (Run #2), where Si- and W-rich regions are observed. The 316H sample does not contain W, so the observed W can be from the W–Re tool used in this study. Figure 9(a) shows the EBSD orientation map that reveals the grain structure of the FSC 316H sample. The grains are equiaxed and refined, and the grain sizes are 0.77 and 0.55 µm for the first two runs. Figure 9Figure 9(b) shows a plot of the microhardness of the FSC 316H samples.

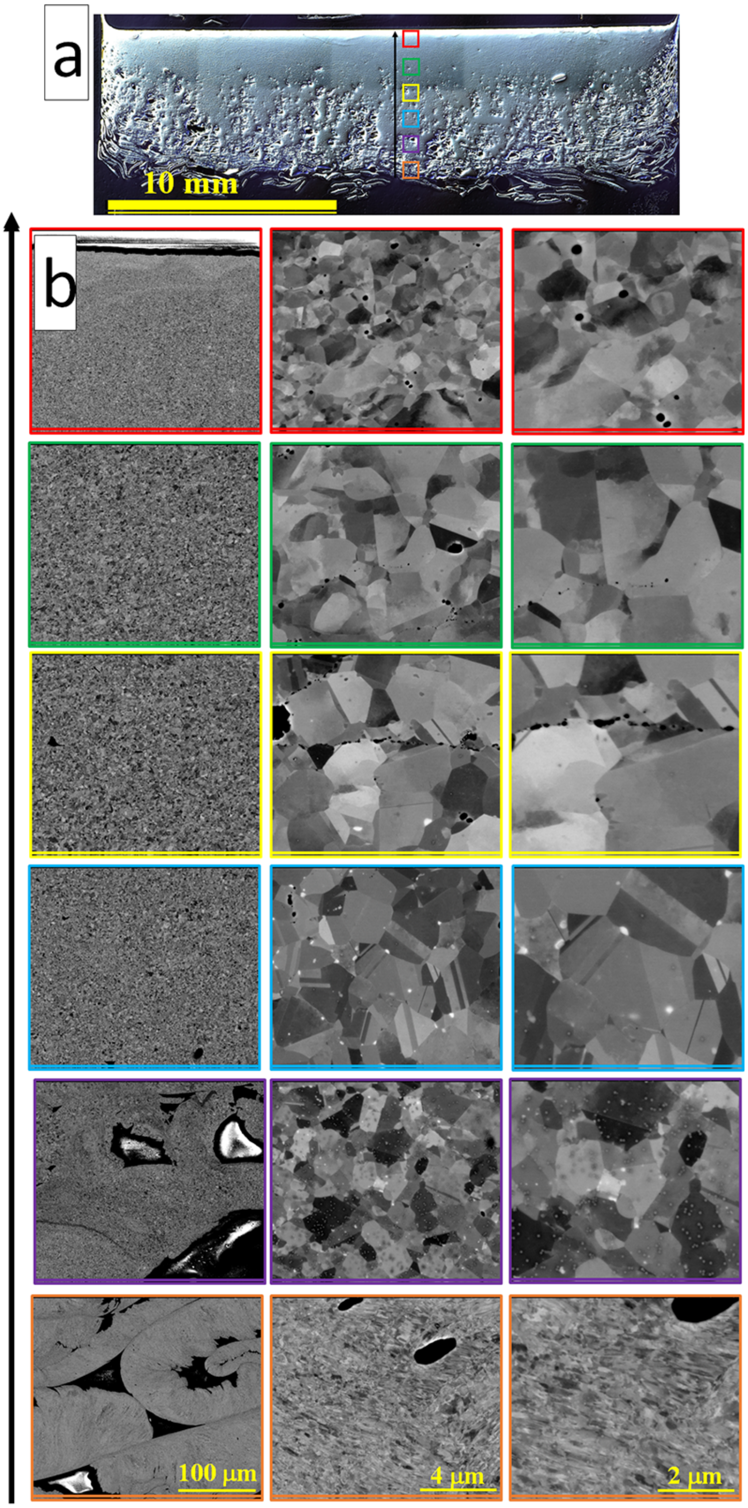

Figure 7. (a) Optical image of an FSC 316H sample. The black line in (a) indicates the location of the SEM images in (b).

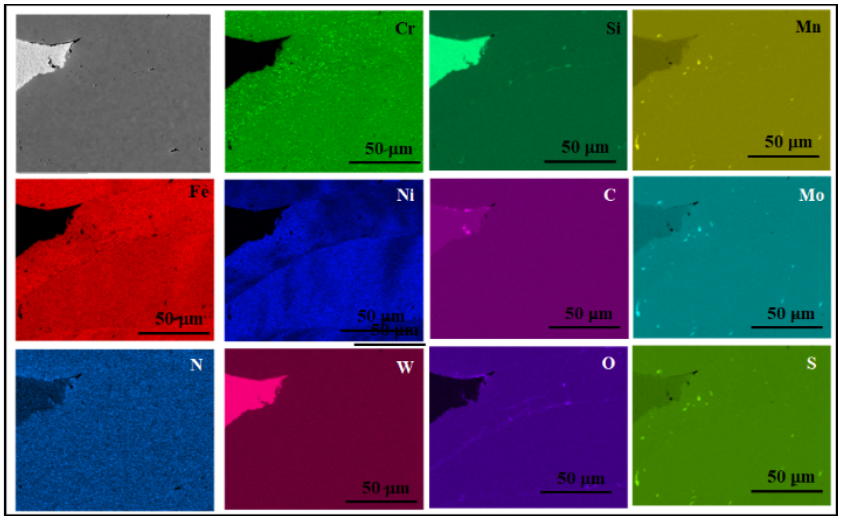

Figure 8. EDS maps of the FSC 316H sample, showing the presence of W and Si.

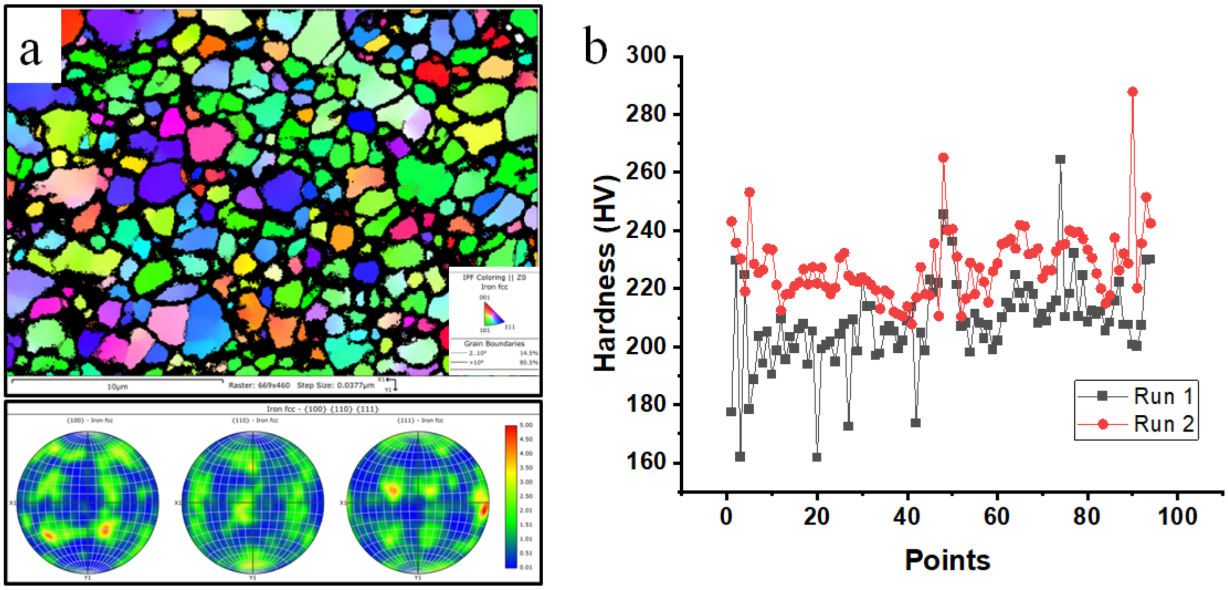

Figure 9. (a) EBSD map of the FSC 316H sample, showing a finer and equiaxed grain structure and (b) hardness plot of the FSC 316H samples.

3.1.4 FSC of Alloy 617

Four runs of friction consolidation for Inconel 617 nickel alloy chips were conducted, with the critical parameters listed in Table 5. As the loading force was increased from 20 kN in Run #1 to 35, 50, and 65 kN in Runs #2, #3, and #4, respectively, the rotation rates were reduced from 100–150 RPM in Run #1 to 50–100, 40–100, and 30–100 RPM in Runs #2, #3, and #4, respectively, to maintain a consistent tool/chip interface temperature of 900°C. All four experiments yielded fully consolidated layers.

Table 5. Critical parameters for the friction consolidation of Inconel 617 alloy chips.

Run #	Weld #	Tool	Loading (kN)	Rotation rate (RPM)	Temperature (°C)	Processing time (s)
1	2024-04-30#000	W–Re	20	100–150	Up to 900	150
2	2024-04-30#001	W–Re	35	50–100	Up to 900	180
3	2024-05-03#000	W–Re	50	40–100	Up to 900	180
4	2024-05-03#001	W–Re	65	30–100	Up to 900	180

Figure 10(a–b) show SEM images and an EBSD map of the as-received sample of IN617, respectively. The grains of the as-received IN617 sample can be observed with significant size variations (10.2 µm, STD 6.8 µm).

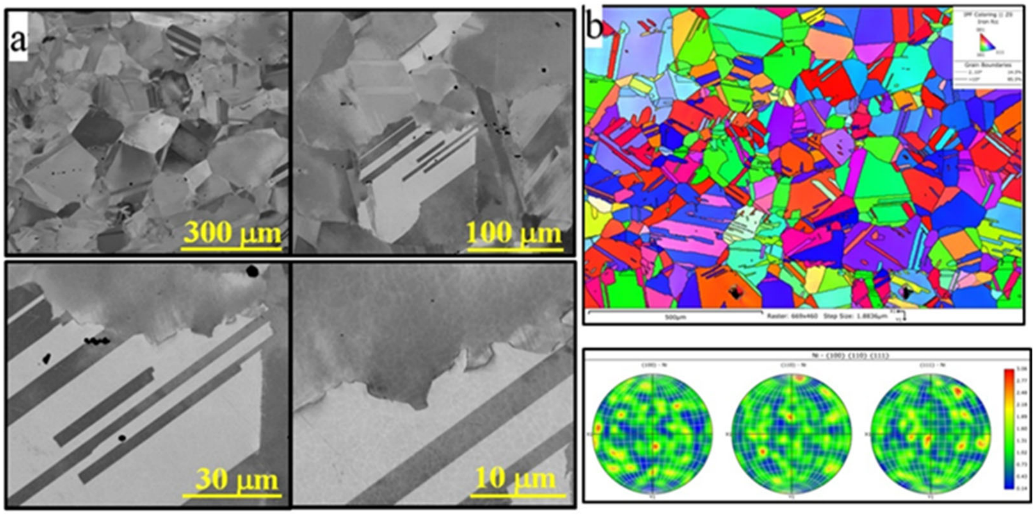

Figure 10. (a) SEM images and (b) EBSD map showing the grain structure of the as-received IN617 material.

An optical image of the cross section of a friction-consolidated IN617 sample (Run #4) is shown in Figure 11(a). From this image, the middle part of the consolidated product shows no significant pore spacing or defects. The consolidation of IN617 chips is observed to be lower towards both ends. Figure 11(b) shows a montage of SEM images collected from the dense consolidated part indicated by the black line in Figure 11(a). This area was analyzed by SEM, and images at different magnifications were collected. The grains from all areas appear to be equiaxed and finer (1.35 and 1.14 µm for Runs 3 and 4, respectively) compared to those in the as-received IN617 sample. Further, grain boundary precipitates are retained in the FSC product.

Figure 12(a) shows an EBSD orientation map that reveals the grain structure of the FSC IN617 sample. The grains appear to be equiaxed and refined, and Figure 12(b) shows a plot of the microhardness of the as-received and FSC IN617 samples. It is observed that the FSC samples have a higher hardness due to finer grains.

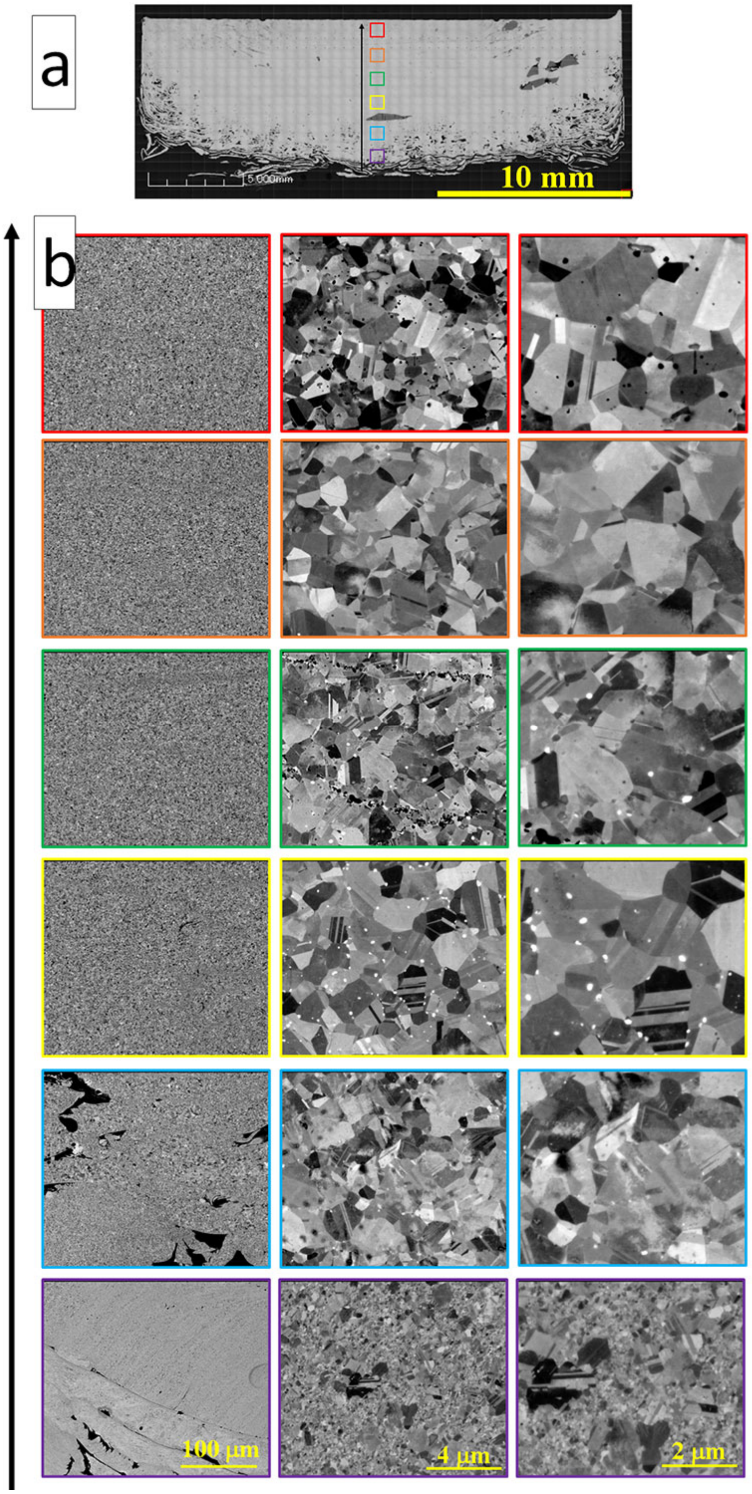

Figure 11. (a) Optical image of the FSC IN617 sample. The black line in (a) indicates the location of the SEM images in (b).

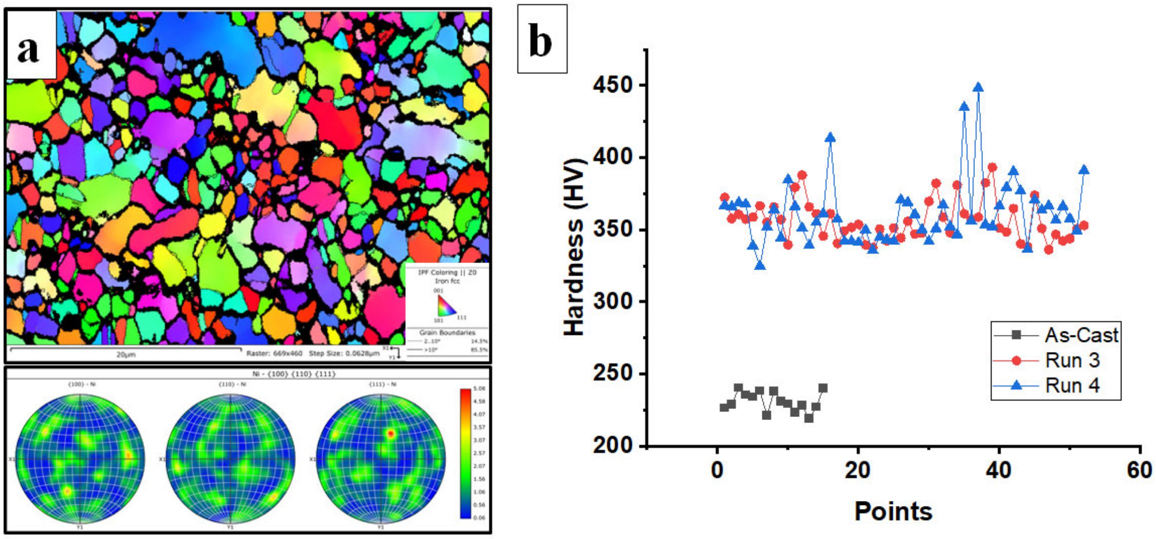

Figure 12. (a) EBSD map of an FSC A709 sample showing a finer and equiaxed grain structure and (b) a plot of the hardness of the as-received and FSC A709 samples.

Evolution of the relative density during friction consolidation: According to the machine data, the real-time relative density of the chips during the friction consolidation experiments can be measured.

This section presents the results of Inconel 617 friction consolidation experiments. As shown in Figure 13, there are four stages during friction consolidation:

- Stage 1: The relative density rapidly increases without a significant rise in temperature. This stage is very brief, lasting around 15 s.
- Stage 2: The increase in the relative density slows compared to that in Stage 1, while the tool/chip interface temperature begins to rise towards its peak.
- Stage 3: The relative density increases again, faster than that in Stage 2 but slower than that in Stage 1. During this stage, the tool/chip interface temperature stabilizes at its peak.
- Stage 4: The increase in the relative density slows but continues at a steady rate. The tool/chip interface temperature remains constant at its peak level.

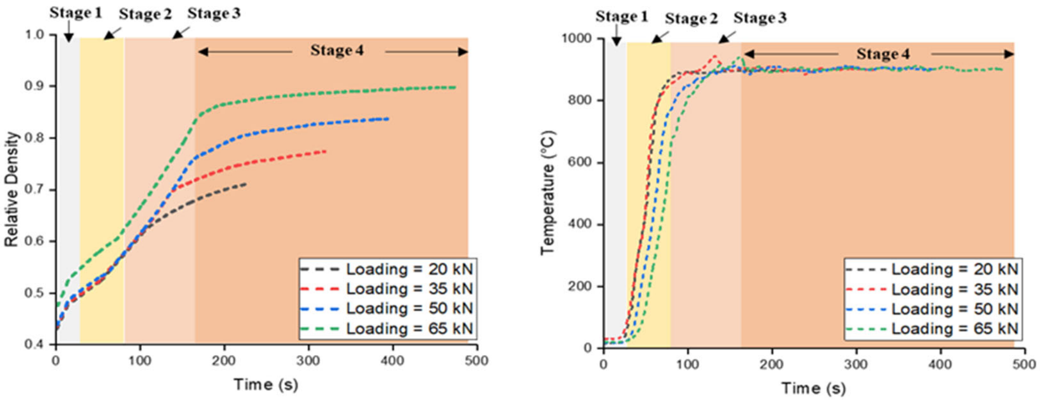

Figure 13. Relative density vs. time (left) and tool/chip interface temperature vs. time (right) for Runs #1–#4 of the friction consolidation of Inconel 617 chips.

3.1.5 FSC Summary

This work aims to ascertain the feasibility of FSC as a materials recycling process utilizing three nuclear-reactor-relevant alloys. The main findings are summarized below:

1. In the FSC process, metal chips of all three alloys were successfully solid-state-consolidated into dense products after limited optimization of process parameters. The extents of consolidation in A709 and IN617 are higher compared to that in 316H. Further, the real-time density evolution was measured, revealing the mechanism of the consolidation process, which will allow for future upscaling benefits.
2. In all three alloys (A709, 316H, and IN617) that were FSC-processed, the grains are refined in size and nearly equiaxed, removing any anisotropy from the starting material. In A709, the grain size decreased by nearly 80 percent (from 10 to 2 μm). Similarly, the grain size reduction was nearly 88 percent in IN617 (from 10.2 to 1.2 μm).
3. Subsequently, the hardness of the FSC product substantially increases because of grain boundary strengthening (Hall–Petch relationship).
4. In the 316H consolidation, small W- and Si-rich particles were observed in the chemical analysis. The W is possibly due to wear from the tool used for friction stir compaction.

In summary, this project provides evidence of the successful recycling of solid waste offcuts resulting from conventional manufacturing processes from three relevant alloys to next-generation nuclear reactor developers, providing a potentially upscalable circular process where no critical elements will be lost.

3.2 Liquid Waste: Metal Recovery through Aqueous Separation

A summary of Milestone Report M3CR-22PN0401013, “Develop and Perform Feasibility Experiments for Critical Materials Waste Minimization Enabled by AM Techniques,” is presented in this section.

3.2.1 Introduction

As mentioned earlier, the global demand for stainless steel is rapidly increasing, leading to concerns over the supply of Ni, Mn, and Cr. Natural sources of these minerals are finite, with Hubbert’s model (Sverdrup and Ragnarsdóttir 2014) projecting peak production between 2020 and 2050. Recycling these minerals is essential to mitigate shortages; enhanced recycling could delay mineral scarcity by extending their availability from less than 45 years to over 400 years with a 90% improved recycling rate.

Increasing attention has been given to the recovery of CMs from industrial wastewater in the United States and globally. Industrial processes, such as electroplating and mining, generate wastewater containing high concentrations of CMs. For instance, electroplating processes can produce wastewater with over 80,000 mg/L Ni^{2+} (Gorokhovsky et al., 2020), while mining processes contain 6,900–11,000 mg/L Ni and significant concentrations of Co (700–1,100 mg/L), Mn (23–200 mg/L), and Cr (140–2000 mg/L) (Capilitan et al., 2023).

Recovery of CMs from industrial wastewater is advantageous, offering an alternative to primary resources, enhancing recycling rates, and mitigating environmental and health hazards. Various recovery technologies have been explored, including chemical precipitation, ion exchange, membrane filtration, adsorption, solvent extraction, and electrochemical treatment (Coman et al., 2013; Qasem et al., 2021). Among these, adsorption is favored because of its simplicity, cost-effectiveness, efficiency, low sludge production, and low reagent consumption. Traditional adsorbents, such as activated carbons, zeolites, and functionalized metal–organic frameworks (MOFs), often require long contact times to reach adsorption equilibrium. Traditional ion-exchange materials face limitations like slow kinetics and poor chemical stability (Ali and El-Bishtawi, 1997; Leinonen and Lehto 2000; Nagib et al., 1999; Revathi et al., 2012) and have limitations in practical applications due to difficulties in handling and recovery.

Advanced techniques, such as ionic metal–organic frameworks (iMOFs) and magnetic nanofluid extraction, offer promising solutions (Dutta et al., 2022). iMOFs, known for their highly ordered and porous structures, demonstrate excellent chemical stability, high sorption capacity (34.1 mg/g for Ni^{2+} with >99.9% removal efficiency), and rapid uptake, achieving complete Ni^{2+} extraction within 5 minutes. Additionally, these sorbents can coextract multiple minerals, enhancing their effectiveness for CM recovery.

PNNL has developed a patented magnetic nanofluid extraction technology for rare-earth elements from brines (Figure 14) (Elsaidi et al., 2018; Liu et al., 2024). Core–shell composite nanoparticles with a magnetic iron oxide core (Fe_3O_4) and an iMOF shell functionalized with chelating ligands provide a high concentration of chelating sites without the need for traditional packed bed or membrane systems. This technology has demonstrated recovery efficiencies exceeding 90%, with production costs significantly lower than current market values. Adaptations of this process could potentially extract nickel from alloy manufacturing scrap and other processes, highlighting the need for sorbents with a high adsorption capacity, chemical stability, and rapid mineral uptake.

The development and implementation of advanced sorbents and technologies for the recovery of CMs from industrial wastewater are critical for addressing mineral scarcity, promoting sustainability, and ensuring environmental safety. By leveraging innovative solutions like iMOFs and magnetic nanofluid extraction, the industry can meet the increasing demand for CMs and enhance recycling efficiency. The potential impacts of the electrochemical separation of CMs from aqueous sources on the full CM lifecycle are shown in Figure 15.

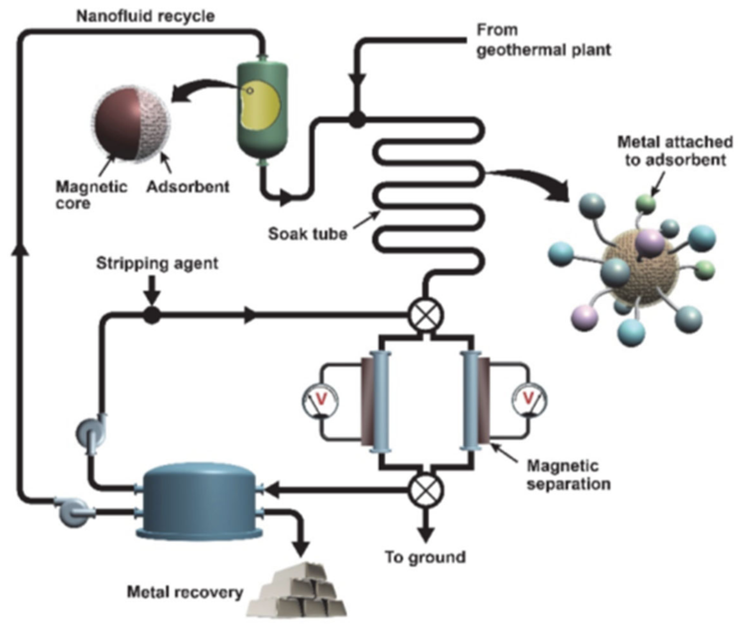

Figure 14. Schematic of the magnetic nanofluid extraction system (Elsaidi et al., 2018).

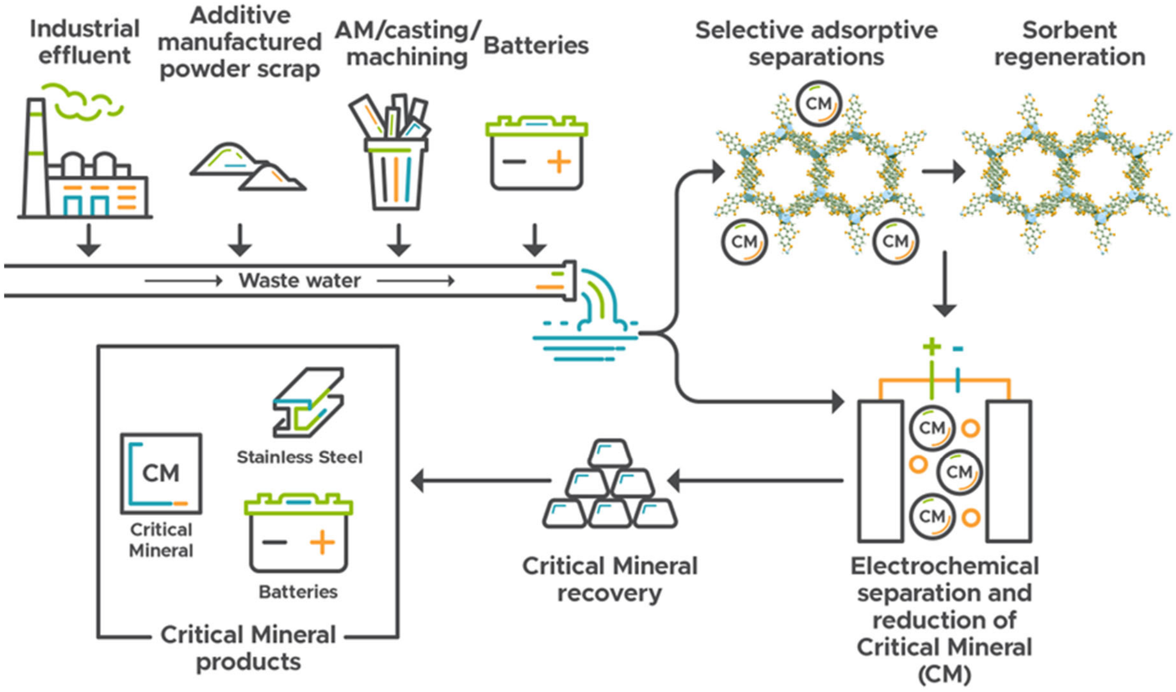

Figure 15. Schematic showing the impact of the electrochemical separation of CMs from aqueous sources on the full CM lifecycle.

3.2.2 Synthesis of Anionic Frameworks as Adsorbents

A series of iMOFs were synthesized under solvothermal conditions (Svensson Grape et al., 2023) [Figure 16(a, b)]. Since it is an anionic framework, there are charge-balancing cations such as dimethylammonium (DMA) in the pores to stabilize the framework structure. The DMA ions in the pores of iMOF(DMA) can be easily exchanged with lithium (Li), sodium (Na), and potassium (K) ions, resulting in the formation of iMOF(Li), iMOF(Na), and iMOF(K), respectively. Here, we present the most promising dataset, that of the iMOF(Li); for results on Na- and K-exchanged iMOFs, see Milestone Report M3CR-22PN0401013 (van Rooyen et al., 2024).

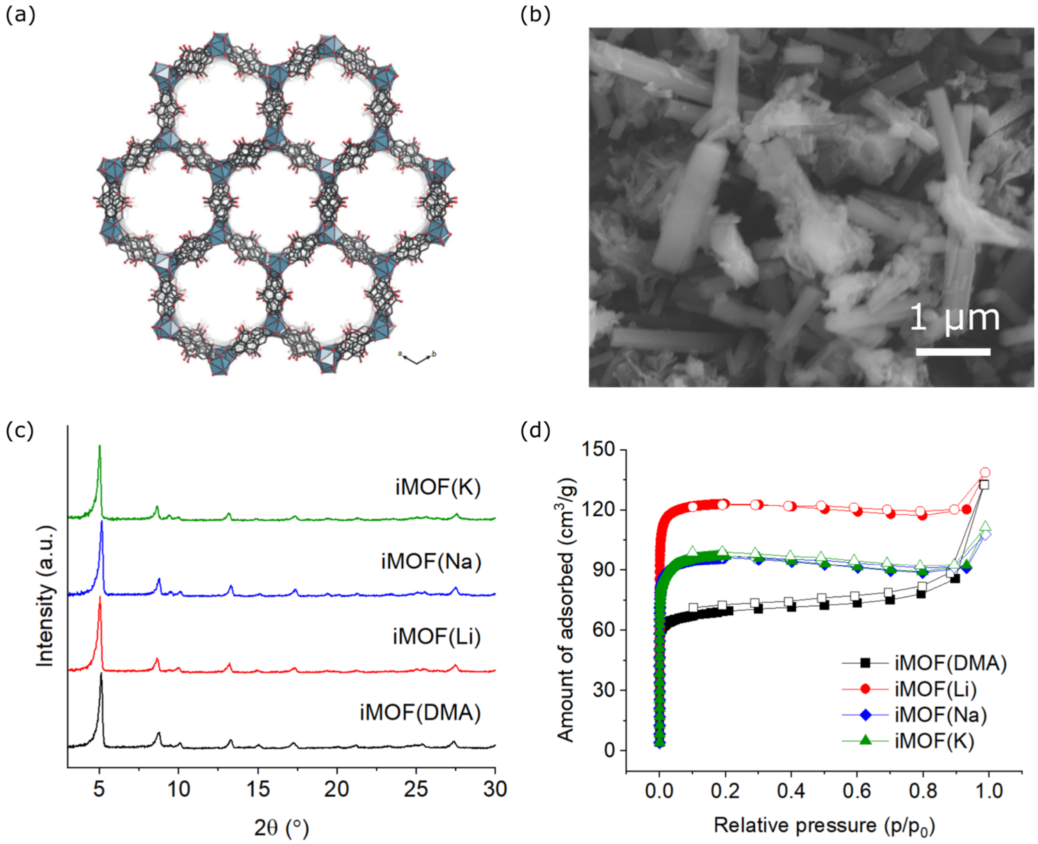

Figure 16 (a) Crystal structure of an iMOF (Svensson Grape et al., 2023), (b) scanning electron microscope image of iMOF(DMA) crystals, (c) powder X-ray diffraction patterns, and (d) nitrogen adsorption–desorption isotherms of iMOFs.

The powder X-ray diffraction (PXRD) patterns of the iMOFs in Figure 16(c) show identical diffraction peaks, confirming that the crystal structures of the iMOFs remain intact after cation exchange. It is noted that the nitrogen adsorption–desorption isotherms measured at 77 K [Figure 16(d)] illustrate that cation exchange leads to an increase in the Brunauer–Emmett–Teller (BET) surface areas of the iMOFs. Exchanging the charge-balancing cation from DMA to Li increases the surface area from 273.5 m^2/g to 505.3 m^2/g. This could be due to the replacement of the bulkier DMA ion with a smaller ion. Elemental analyses of the iMOFs (Table 6) show that DMA ions were fully exchanged to Li ions.

Table 6. Chemical compositions of iMOFs.

	C (wt%)	N (wt%)	Zr (wt%)	Li (wt%)
iMOF(DMA)	45.69	6.5	8.41	-
iMOF(Li)	37.35	0.58	10.26	1.54

3.2.3 pH Stability of iMOFs

Industrial wastewater, which is generated after electroplating, mining, tannery, and smelting processes, is complex and can have various pH ranges. Therefore, the stability of iMOFs under harsh chemical conditions is vital for industrial applications such as the treatment of wastewater sludge. The pH stability of iMOFs was evaluated by exposing iMOF(DMA) to aqueous solutions of HCl or NaOH for more than 24 h. As shown in Figure 17Figure 17, the structure of the iMOF remained unchanged under highly acidic (pH 1) and highly basic (pH 11) conditions, proving that the iMOF is highly stable in aqueous solution over a wide range of pH values. The results show that the iMOF is suitable for use in industrial wastewater.

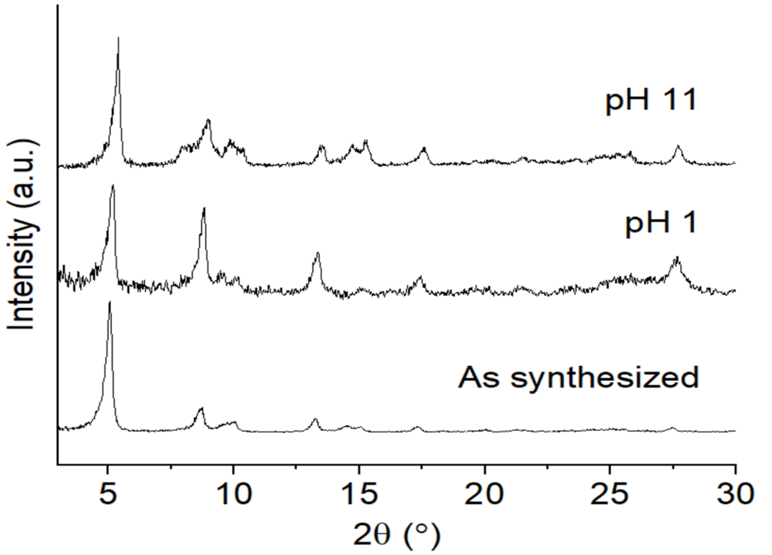

Figure 17. PXRD patterns of the iMOF after being exposed to various pH levels in aqueous solution at room temperature.

3.2.4 Nickel Extraction from Aqueous Brine by iMOFs

Batch sorption experiments were carried out by suspending the iMOFs in stock solutions of metal ions in water, which were stirred for a given time at 300 RPM at room temperature. For Ni^{2+} extraction, the iMOFs (3 mg/mL) were dispersed in a $Ni(NO_3)_2 \cdot 6H_2O$ solution (Ni^{2+} = 100 mg/L). For the coextraction of multiple metal ions, the iMOFs (4 mg/mL) were dispersed in a stock solution containing three metal ions ($Ni^{2+} = Mn^{2+} = Co^{2+}$ = 100 mg/L). The iMOFs were removed from stock solutions by centrifugation at 9,000 RPM repeated 5 times, and the supernatant solution was collected to measure the final concentration of metal ions. The sorption capacity (Q) and removal efficiency were calculated using the following equations:

$$Q\ (\frac{\mathrm{mg}}{\mathrm{g}}) = \frac{C_{\mathrm{M,0}} - C_{\mathrm{M,e}}}{C_{\mathrm{iMOF}}} \tag{1}$$

$$\text{Ni removal efficiency (\%)} = \frac{(C_{\mathrm{M,0}} - C_{\mathrm{M,e}})}{C_{\mathrm{M,0}}} \times 100 \tag{2}$$

where $C_{\mathrm{M,0}}$ is the initial metal concentration (mg/L), $C_{\mathrm{M,e}}$ is the equilibrium metal concentration (mg/L), and C_{iMOF} is the iMOF concentration (mg/mL).

The Ni adsorption capacities are 33.4 mg/g for iMOF(DMA) and 34.1 mg/g for iMOF(Li) and are given in Figure 18(a). The Ni^{2+} removal efficiency of iMOF(DMA) was 97.8%, and that of iMOF(Li) was >99.9% [Figure 18(b)]. The Ni^{2+} concentration of the resultant Ni solution with iMOF(Li) after extraction was undetectable because the Ni concentration was lower than the inductively coupled plasma (ICP) detection limit.

The Ni^{2+} sorption kinetics of the iMOFs were studied by taking an aliquot of the Ni solution at different soaking times and measuring the Ni^{2+} concentration. Within a contact time of 5 min, complete Ni^{2+} extraction (>99.9% removal efficiency) was achieved by iMOF(Li) [Figure 18(b)]. Compared to other previously reported ion exchange materials or MOF-based sorbents (Peng et al., 2018, Piątek et al., 2021), which typically show slow extraction kinetics, Ni^{2+} sorption by the iMOFs is a rapid and efficient process, which is vital for the industrial Ni recovery process.

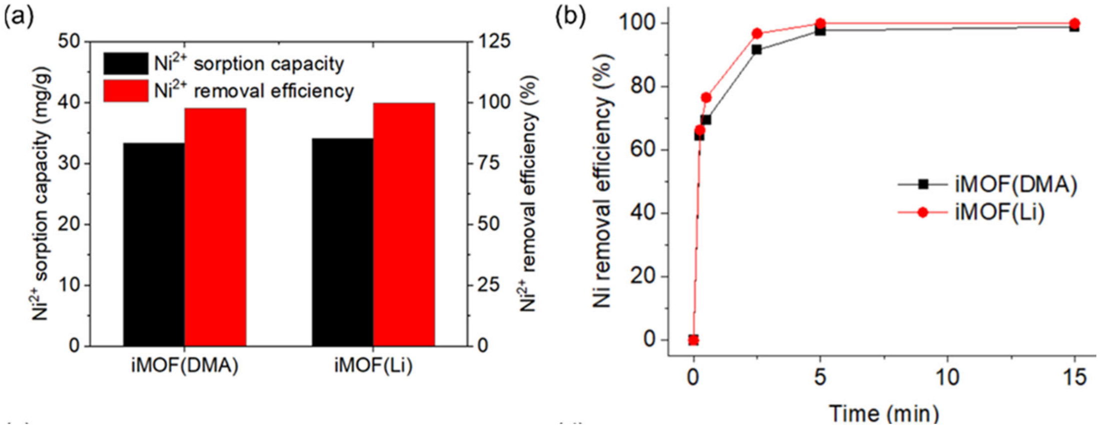

Figure 18. (a) Ni^{2+} sorption capacity and Ni^{2+} removal efficiency of iMOFs. (b) Ni^{2+} sorption kinetics on iMOFs.

To investigate the mechanism behind Ni adsorption by an iMOF, the adsorption kinetics data were modeled with the following pseudo-second-order kinetics equation (Ünlü and Ersoz, 2007):

$$\frac{t}{Q_{\mathrm{t}}} = \frac{1}{kQ_{\mathrm{e}}^2} + \frac{t}{Q_{\mathrm{e}}} \tag{3}$$

where Q_{t} = the Ni adsorption capacity at time t (mg/g)
Q_{e} = the Ni adsorption capacity at equilibrium (mg/g)
t = the adsorption time (min)
k = the adsorption rate constant [g/(mg·min)].

Table 7. Kinetic parameters of Ni adsorption using a pseudo-second-order kinetic model.

	R^2	k (g/mg·min)	$Q_{e,model}$ (mg/g)	$Q_{e,exp}$ (mg/g)
iMOF(DMA)	0.999	0.212	25.71	25.50
iMOF(Li)	0.999	0.332	25.84	25.60

Table 7 summarizes the model parameters and correlation coefficients (R^2) obtained from a linear fitting of the results in Figure 18(b). The R^2 values for the pseudo-second-order kinetics model are above 0.999, and the Q_e values calculated by the model ($Q_{e,model}$) are very close to the experimental values ($Q_{e,exp}$). The results show that the pseudo-second-order kinetics model is suitable for describing Ni adsorption onto the iMOF and that the adsorption process is chemisorption (ion exchange between Ni and the charge-balancing cation).

To investigate how much the charge-balancing cations in the pores of the iMOF are exchanged during Ni adsorption, the percentage of cation exchange was calculated as follows:

$$\text{Cation exchange (\%)} = \frac{C_{\text{cation}}}{C_{\text{iMOF}} \times \omega_{\text{cation}}} \times 100 \qquad (4)$$

where C_{cation} = the concentration of the cation in the solution (mg/L)
C_{iMOF} = the concentration of the iMOF in the solution (mg/L)
ω_{cation} = the mass fraction of the cation in the iMOF.

A Ni-loaded iMOF can be regenerated by being washed in a high-concentration acid or salt solution Figure 19. After the Ni-loaded iMOF(DMA) was immersed in a 1 M hydrochloric acid (HCl) solution for 1 h, the Ni concentration in the HCl solution increased to 59.4 ppm. Immersion in a 1 M dimethylammonium chloride (DMACl) solution led to Ni release from the Ni-loaded iMOF(DMA) as well, and the Ni concentration in the DMACl solution increased to 38.6 ppm. The results indicate that the extracted Ni can be collected and concentrated in an acid or salt solution.

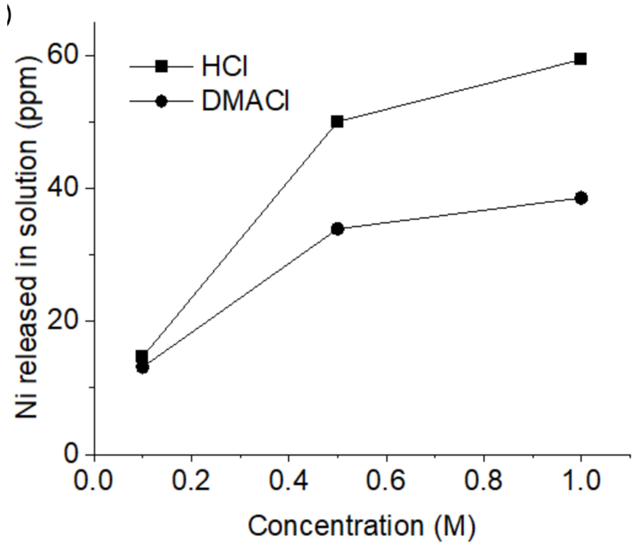

Figure 19. Ni released from the Ni-loaded iMOF(DMA) immersed in different concentrations of HCl and DMACl for 1 h.

4.0 Coextraction of CMs from Aqueous Brine by iMOFs

Considering that some aqueous brines may contain multiple minerals, batch adsorption was investigated by suspending an iMOF (4 mg/mL) in a brine containing five minerals (Table 8) at room temperature.

Table 8 Composition of brine with multiple minerals.

Ni (mg/L)	Mn (mg/L)	Cu (mg/L)	Fe (mg/L)	Co (mg/L)
100	100	100	100	100

The adsorption capacities and removal efficiencies for Ni, Mn, copper (Cu), iron (Fe), and Co shown in Figure 20(a, b) prove the effectiveness of the iMOF as a general adsorbent to extract multiple minerals simultaneously. Compared to the Ni adsorption capacity (25.58 ± 0.04 mg/g) and Ni removal efficiency (99.5% ± 0.69%) of the iMOF in a brine containing Ni only [Figure 18(b)], the Ni adsorption capacity and Ni removal efficiency of the iMOF were reduced to 13.19 ± 0.52 mg/g and 48.39% ± 0.48%, respectively, in a brine containing multiple metal ions. This is attributed to competition with coexisting minerals.

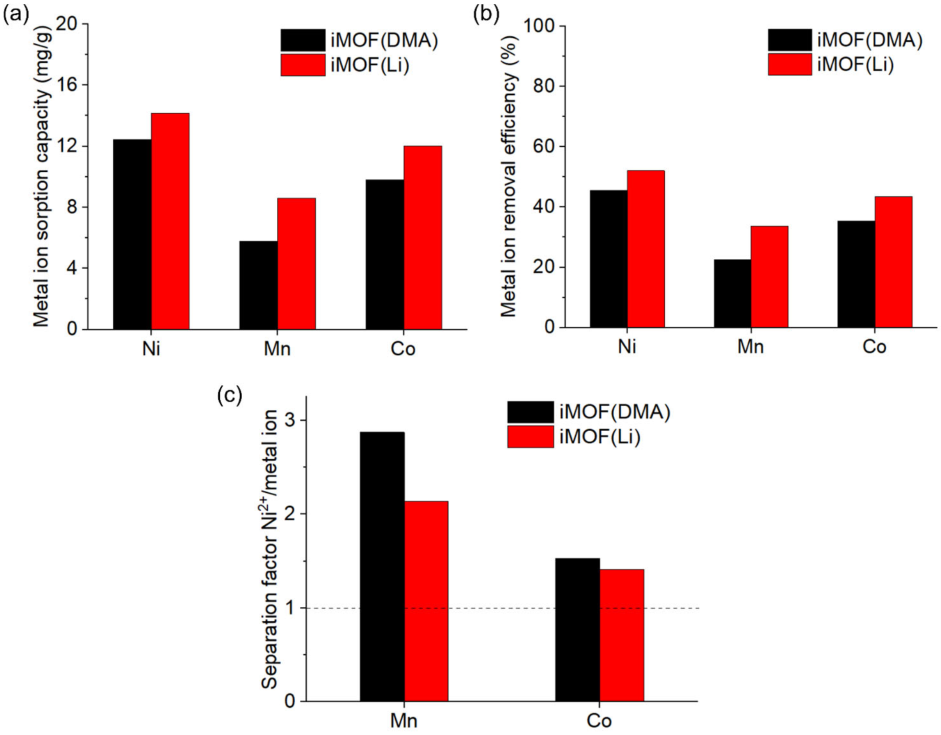

Figure 20 (a) Ni^{2+}, Mn^{2+}, and Co^{2+} sorption capacities and (b) Ni^{2+}, Mn^{2+}, and Co^{2+} removal efficiencies of iMOFs in a solution containing multiple metal ions. (c) Separation factor values for Ni^{2+}/Mn^{2+} and Ni^{2+}/Co^{2+} of iMOFs.

The adsorption performance of the iMOF for multiple minerals was further analyzed in terms of the distribution coefficient (K_d) and selectivity (α), expressed as

$$K_{\mathrm{d}} = \frac{C_{\mathrm{M,0}} - C_{\mathrm{M,e}}}{C_{\mathrm{M,e}} \times C_{\mathrm{iMOF}}} \quad (5)$$

$$\alpha = \frac{K_{\mathrm{d}}^{\mathrm{Ni}}}{K_{\mathrm{d}}^{\mathrm{M}}} \quad (6)$$

where $C_{\mathrm{M,0}}$ = the initial concentration of the mineral in the solution (mg/L)
$C_{\mathrm{M,e}}$ = the equilibrium concentration of the mineral in the solution (mg/L).

A larger K_d indicates more adsorption of the cation in the iMOF; therefore, a larger α indicates preferable adsorption of Ni over the coexisting mineral (M) in the brine. As shown in Figure 20(c), the α values for Ni/Mn ($K_{\mathrm{d}}^{\mathrm{Ni}}/K_{\mathrm{d}}^{\mathrm{Mn}}$) and Ni/Co ($K_{\mathrm{d}}^{\mathrm{Ni}}/K_{\mathrm{d}}^{\mathrm{Co}}$) are greater than 1, suggesting that the iMOF preferably adsorbs Ni compared to Mn and Co, whereas the α values for Ni/Cu ($K_{\mathrm{d}}^{\mathrm{Ni}}/K_{\mathrm{d}}^{\mathrm{Cu}}$) and Ni/Fe ($K_{\mathrm{d}}^{\mathrm{Ni}}/K_{\mathrm{d}}^{\mathrm{Fe}}$) are less than 1, suggesting that the iMOF preferably adsorbs Cu and Fe compared to Ni.

4.1.1 Ni Recovery: Conclusion and Next Steps

PNNL developed ionic framework-based adsorbents (iMOFs) for the recovery of CMs from aqueous brine. The synthesized adsorbents are highly stable in aqueous solution over wide pH ranges and show excellent mineral removal efficiency (>99.9%) within 5 min, indicating efficient mineral extraction capability from industrial wastewater. Based on current research work, future work is needed to investigate the cycling performance of the iMOFs and the controlled release of multiple minerals captured by an iMOF simultaneously. Despite the major advantages of the developed iMOFs encompassing chemical stability, a high adsorption capacity, and rapid mineral uptake, their major limitation is their processability in powder form, which limits their applicability in real-world applications. Hence, extensive research efforts need to be devoted to the construction of more robust and portable forms such as engineered particles, thin films, or membranes combined with electrochemical and/or magnetic separation to meet the demands of practical applicability and commercialization.

4.2 Conclusions and Next Steps

The experimental feasibility studies showed the positive impacts of the recycling of solid waste through the consolidation of machining chips or offcuts and liquid waste metal recovery through aqueous separation for nuclear material supply risks.

In summary, this project provides evidence of the successful recycling of solid waste offcuts resulting from conventional manufacturing processes from three relevant alloys to next-generation nuclear reactor developers, potentially providing upscaling for a circular process, where no critical element will be lost. Furthermore, iMOF-based adsorbents were successfully designed for CM extraction from aqueous solution, thereby providing a pathway for future upscaling opportunities for salvaging dissolved Ni ions. This research has achieved its goal of showing the impact of novel applications of recycling technologies for solid and liquid waste that can be upscaled for application.

5.0 Replacement Materials for Current Scarce or High Supply Chain Risk Materials

A summary of Milestone Report M3CR-22PN0401015, “Development on Replacement of Materials for Current Scarce or High Supply Chain Risk Materials,” is presented in this section.

5.1 Introduction

The demand for metals and CMs will rapidly increase with international ambitions to address climate change, in which the current strategy is set up to comply with a 2°C scenario (2015 Paris Accord). Global material use will more than double, from 79 billion tons in 2011 to 167 billion tons in 2060. The projected growth in materials use, coupled with the environmental consequences of material extraction, processing, and waste, is likely to increase pressure on the resource bases of the planet’s economies and jeopardize economic and social gains in well-being.

CMs are essential for a range of clean energy technologies, which are experiencing rapid growth due to global policies and business agendas in recent years. Record deployment of clean energy technologies such as solar PVs and batteries is propelling unprecedented growth in CM markets, while electric car sales exceeded 10 million units in 2022 (Khaleel et al., 2024). Energy storage systems experienced even more rapid growth, with capacity additions doubling in 2022 and wind power installations set to resume their upward trend. All of this has led to a significant increase in demand for CMs and increased supply pressure on all other industries. From 2017 to 2022, the demand from the energy sector was the main factor behind a tripling in the overall demand for lithium, a 70% jump in demand for cobalt, and a 40% rise in demand for nickel. In 2022, the share of clean energy applications of the total demand reached 56% for lithium, 40% for cobalt, and 16% for nickel, up from 30%, 17%, and 6%, respectively, five years ago (IEA, 2023b).

Driven by rising demand and high prices, the market share of energy transition minerals doubled over the past five years, reaching USD 320 billion in 2022. Energy transition minerals, which used to be a small segment of the market, are now moving to center stage in the mining and metals industry. A combination of volatile price movements, supply chain bottlenecks, and geopolitical concerns has created a mix of risks for secure and rapid energy transitions. In the present study, Inconel 617 has been selected as an alloy system to substitute its high Co concentration using noncritical Mn. Alloy 617 is considered for use in molten salt reactor (MSR), gas-cooled fast reactor (GFR), and very-high-temperature gas-cooled reactor (VHTR) systems because of its desirable properties such as high mechanical strength, good oxidation and corrosion resistance, considerably low thermal expansion (Natesan and Tam, 2003), high phase stability preventing the formation of embrittling phases (e.g., sigma, mu, chi, or Laves phases) at elevated temperatures, and good weldability.

A computational feasibility study of compositional changes to IN617 is presented here. Compositional modifications were made by systematically substituting the Co concentration with Mn in IN617, generating a set of possible compositional modifications. These computational studies include an analysis of the effects of Mn addition and Co subtraction on the strength and corrosion resistance at different atomic percentages and their phase diagram calculations. For the mechanical properties, tensile tests on cubic simulation cells using molecular dynamics (MD) have been performed to obtain the stress–strain curves that reveal the effect of Co replacement with Mn on the tensile strength, which maintains a directly proportional relationship with hardness. MD simulations were employed not to obtain quantitatively accurate values but rather to provide a direction for guided experimentation. Specifically, MD simulations helped to down-select the most promising modifications, focusing on properties such as the tensile strength, which could later be correlated with hardness. To assess corrosion resistance, oxygen penetration simulations were conducted, where a lower oxygen penetration depth through the alloy surface indicated higher corrosion resistance. Phase diagrams were also calculated for a few compositions that showed promising results in the simulations, allowing for an assessment of the phase stability under different conditions. Phase diagrams were calculated for a few compositions that showed promising results in the simulation evaluations.

The composition with the best combination of high tensile strength and least oxygen penetration was selected for experimental evaluation. Two different methods were used in this study to obtain alloy samples: (1) induction melting and (2) friction stir consolidation and alloying. The materials were then characterized using SEM-EDS, X-ray diffraction (XRD) (induction melt alloy only), and Vickers hardness.

5.1.1 Molecular Dynamics Simulations

The six different elemental compositions simulated in this study are shown in Table 9. MD simulations of the tensile strain were carried out in the extensively parallelized Large-scale Atomic/Molecular Massively Parallel Simulator (LAMMPS) package (Plimpton 1995); OVITO (Stukowski 2009) was used for visualization and data processing. Figure 21 shows the visualization of the relaxed face-centered cubic (fcc) supercell and the deformed supercell after tensile strain. The embedded-atom potentials (EAM) described by Zhou et al. (2004) and long-range Lennard-Jones potential by Gröger et al. (2020) were used to define the interatomic potentials. The lattice energy was minimized using the conjugate-gradient method with an energy tolerance of 10^{-15} eV and a force tolerance of 10^{-15} eV/Å in LAMMPS.

Table 9. Elemental composition of IN617 and its modified compositions.

Material	Elemental wt.%										Reference
	C	Cr	Ni	Co	Mn	Mo	Ti	Al	Fe	Total	
IN617	0.06	21.6	53.6	12.5	0.0	9.5	0.3	1.2	0.9	99.66	Natesan and Tam (2003)
IN617-M1	0.06	26.6	53.6	2.5	5	9.5	0.3	1.2	0.9	99.66	1st modification
IN617-M2	0.06	24.1	53.6	7.5	2.5	9.5	0.3	1.2	0.9	99.66	2nd modification
IN617-M3	0.06	21.6	53.6	2.5	10	9.5	0.3	1.2	0.9	99.66	3rd modification
IN617-M4	0.06	21.6	53.6	7.5	5	9.5	0.3	1.2	0.9	99.66	4th modification
IN617-M5	0.06	21.6	53.6	10	2.5	9.5	0.3	1.2	0.9	99.66	5th modification

5.1.2 Tensile Simulations

The alloy simulation was initialized with an fcc unit cell, an fcc structure at 300 K under an isothermal–isobaric (NPT) ensemble for 50 ps. Periodic boundary conditions were applied in all directions. Unidirectional tensile deformation was carried out at a strain rate of 0.01 ps^{-1} along the *x*-direction. The strain rate adopted here was previously employed for analyzing the deformation of AlCoCrFeNi high entropy alloy (HEA) (Sharma and Balasubramanian, 2017) and Mo–Ta–Ti–W–Zr (Roy et al., 2022a; Singh et al., 2018). The simulated strain rate is several orders of magnitude higher relative to experiments; this difference is necessitated by the timescales feasible in MD simulations (Wen et al., 2008).

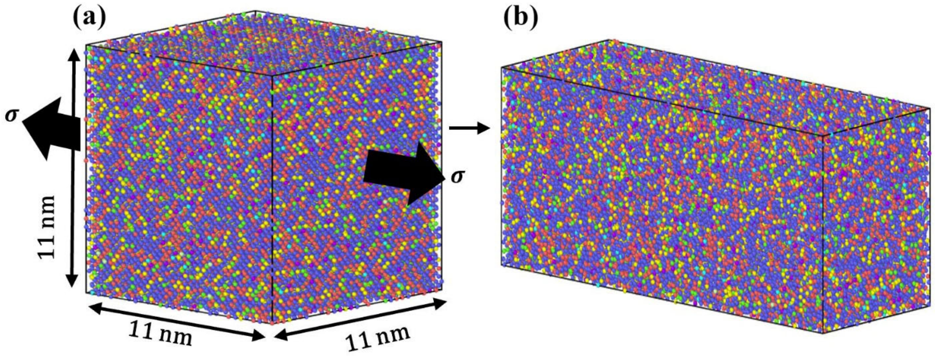

Figure 21. (a) A typical fcc alloy relaxed in molecular dynamics for IN617. (b) Unidirectional tensile deformation executed along the *x*-direction.

The results of the tensile simulations are shown in Figure 22. IN617-M1 possesses the highest strength at both room temperature and 950 K.

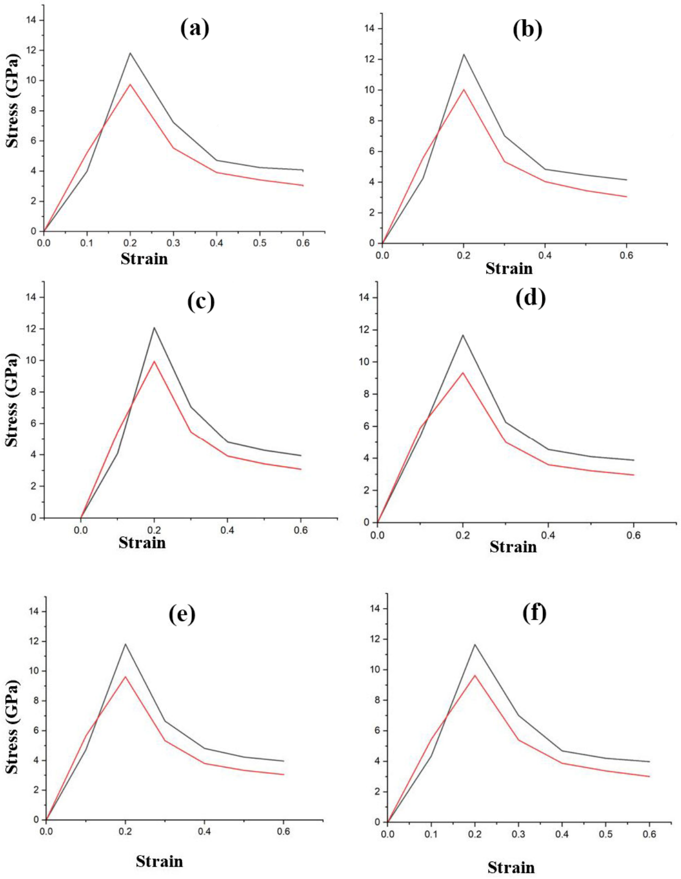

Figure 22. The stress–strain curves due to uniaxial loading in the *x*-direction for (a) IN617 and its five modifications: (b) IN617-M1, (c) IN617-M2, (d) IN617-M3, (e) IN617-M4, and (f) IN617-M5. IN617-M1 shows the best performance at both room temperature and 950 K.

In our study, MD simulations were conducted under tensile stress conditions to derive the yield strengths of various alloy modifications. These tensile strengths can be effectively correlated to hardness using several well-established relationships in the literature. One commonly cited relationship is as follows:

$$H_{\mathrm{V}} \approx 3\sigma_{\mathrm{y}} \tag{7}$$

where H_{V} represents the Vickers hardness and σ_{y} denotes the yield strength (An et al., 2010; Li and Ebrahimi 2003; Zhang et al., 2011). Hardness testing is fundamentally a surface phenomenon, quantifying the localized deformation around the indenter on the material's surface (Broitman, 2017). In contrast, tensile deformation assessments provide insights into the material properties at the bulk level, offering a more comprehensive evaluation of the material's overall strength.

However, tensile testing is both time-consuming and cost-intensive compared to hardness measurements. Consequently, for experimental validation in this study, we opted for hardness measurements because of their efficiency and practicality.

The relative order of alloy strengths determined from tensile simulations is expected to correspond with the order of the hardness values because of the linear proportionality between yield strength and hardness. Thus, while the MD simulations assessed the yield strengths for six different alloy modifications, the experimental validation focused on hardness measurements of the alloy predicted to have the highest strength.

5.1.3 Oxidation Simulations

To simulate the interaction between oxygen and the metals present in the alloy, we employed a set of interatomic interactions detailed in Table 10. The simulation cell, with dimensions of 5 nm × 5 nm × 5 nm, as illustrated in Figure 21, served as the framework for our study. To mimic the formation of an oxide layer, we initially introduced a two-atomic-layer-thick oxygen layer onto the alloy surface, depicted in Figure 22(a). The systems, including the IN617 alloy and its variations, underwent initialization at 500 K within the isothermal–isobaric (NPT) ensemble, followed by a 100 ps equilibration period. During this equilibration, oxygen atoms diffused through the alloy surface into its bulk, culminating in the formation of an oxide layer of specific thickness, as demonstrated in Figure 22(b) and (c). The average oxygen penetration depth is calculated as

$$d = \frac{d_1 + d_2 + d_3 + \cdots + d_n}{n} = \frac{\sum_{i=1}^{n} d_i}{n} \tag{8}$$

where d_1, d_2, …, d_n, are the penetration depths from the surface of oxygen atoms O_1, O_2, O_3, …, O_n.

Table 10. Interatomic potentials used to define the interactions of all nine elements for oxidation simulations of IN617 and its modifications.

Pair/group	Ref.	Interatomic potential type
Cr–Ni–Co–Mo–Ti–Al–Fe	Zhou et al. (2004)	EAM
Cr–Mn, Ni–Mn, Co–Mn, Fe–Mn, Mn–Mn	Groger et al. (2020)	Long-range Lennard–Jones potential
Cr–O	Minervini et al. (1999)	Buckingham potential

Pair/group	Ref.	Interatomic potential type
Ni–O	Restrepo et al. (2022)	Buckingham potential
Co–O	Hermet et al. (2010)	Buckingham potential
Mn–O	Maphanga et al. (2009)	Buckingham potential
Mo–O	Rajaramakrishna et al. (2020)	Buckingham potential
Ti–O	Bandura and Kubicki (2003)	Buckingham potential
Al–O	Georgieva et al. (2009)	Buckingham potential
Fe–O	Restrepo et al. (2022)	Buckingham potential
O–O	Minervini et al. (1999)	Buckingham potential

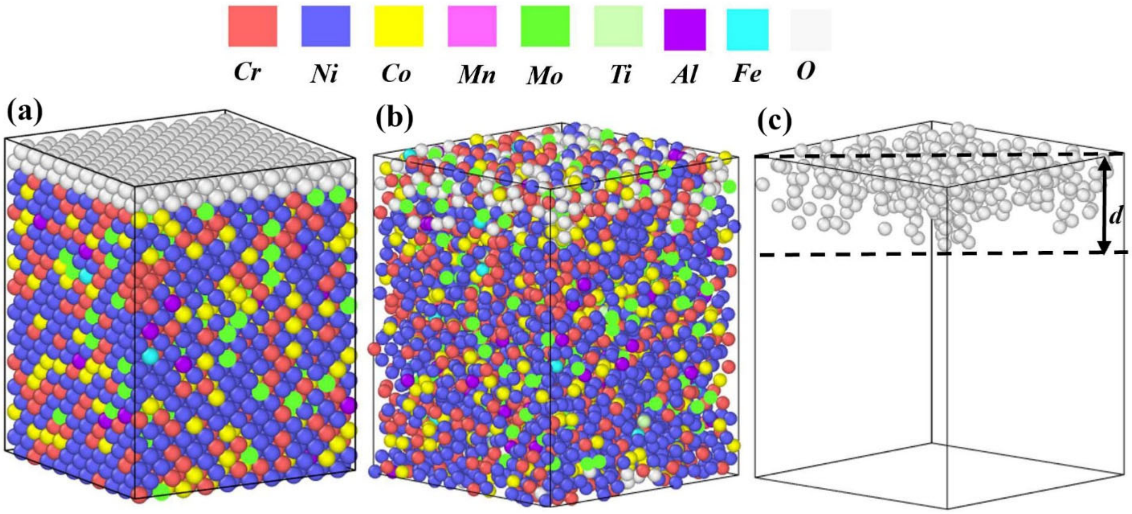

Figure 23. (a) Initial configuration of doubled-layered oxygen atoms over the alloy surface. (b) Formation of an oxide layer 100 ps after the initiation of the simulation. (c) Schematic representing the oxygen atoms’ penetration depth.

5.1.4 Simulation Results

The simulation-estimated tensile strength and oxygen penetration depths are summarized in Table 11. While IN617-M3 shows the lowest oxygen penetration (highest corrosion resistance), it also shows a low tensile strength relative to the IN617-M1 and IN617-M2 alloys. Therefore, the M1 alloy composition is the next best in terms of corrosion resistance, and it also possesses the highest strength. In short, the compositionally modified IN617-M1 exhibits superior strength and corrosion resistance despite having a lower cobalt (Co) content compared to IN617. The IN617-M1 composition features a higher chromium content compared to IN617. Chromium is pivotal for forming a passive oxide layer (mainly chromium oxide) on the alloy surface, providing excellent corrosion resistance by acting as a barrier against further oxidation (Gusieva et al., 2015; Qiu et al., 2017; Roy et al., 2022b). Additionally, chromium contributes to solid solution strengthening, enhancing the mechanical strength of the alloy.

Table 11. Average oxygen penetration depth and tensile strength for IN617 and its modifications. Only Co and Mn elemental compositions are noted for reference.

Alloy	Elemental wt%		Avg. oxygen penetration depth (d) (Å)	Tensile strength (GPa)	
	Co	Mn		300 K	950 K
IN617	12.5	0.0	3.72	11.82	9.74
IN617-M1	2.5	5	3.35	12.33	10.03
IN617-M2	7.5	2.5	3.85	12.08	9.94
IN617-M3	2.5	10	3.08	11.67	9.74
IN617-M4	7.5	5	3.41	11.82	9.63
IN617-M5	10	2.5	3.70	11.66	9.63

In summary, IN617-M1's elemental composition, characterized by a higher chromium content along with balanced ratios of nickel, titanium, and aluminum, contributes to its superior strength and corrosion resistance. The presence of chromium facilitates the formation of a protective oxide layer on the alloy surface, while other elements contribute to strengthening mechanisms and microstructural refinement. Despite having a lower cobalt content compared to IN617, IN617-M1's overall composition enhances its mechanical performance and durability, making it the top choice for experimental validation.

5.2 Phase Diagram Calculations

All phase diagram calculations were carried out using Thermo-Calc 2024a software. The only databases available for this study are Fe/Steels (TCFE13) and High Entropy Alloys (TCHEA7); neither of them is tailored for nickel alloy compositions. Therefore, validating these available databases becomes crucial, which is performed by simulating the phase diagrams (phase fraction versus temperature plots) for IN617 and comparing them with the experimental and modeling data in the literature. After the validation of the use of these databases for Ni-based alloy systems (IN617), the validated databases were used for the prediction of phase diagrams for the other selected alloy compositions shown in Table 9. These modified alloy compositions were used for phase diagram calculations since they are new and lack any experimental data.

The TCHEA7 database failed to compute any results for IN617, while the TCFE13 (Fe/Steels) database was able to partially simulate the phase fraction versus temperature plots, as shown in Figure 24. It should be noted that some regions of the plot were not simulated, which emphasizes that the Fe/Steels database is not tailored for nickel alloys. The phase fraction versus temperature plot from Rai et al. (2017) is presented in Figure 25(a). Both plots are almost identical, but the plot from our study revealed an additional phase, a π phase, below 1000 K.

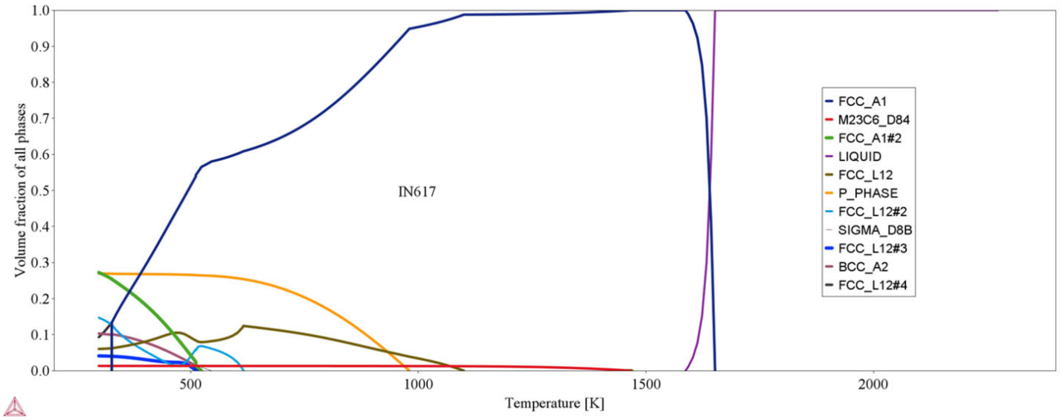

Figure 24. Phase fraction versus temperature plot for IN617 simulated using the TCFE13 database and Thermo-Calc 2024a.

The formation of π phases in the IN617 alloy has been previously observed by Wang et al. (2023). An SEM image showing the π phase, sourced from (Wang et al., 2023), is presented in Figure 25(b) and validates the usage of the Fe/Steels database for nickel alloys.

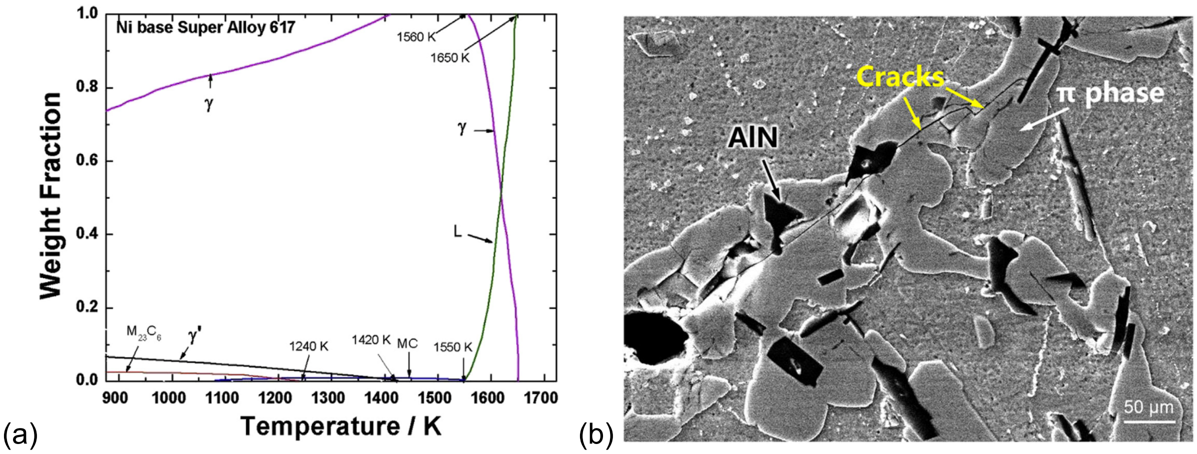

Figure 25. (a) Phase fraction versus temperature plot obtained from (Rai et al., 2017). (b) SEM image showing the presence of the π phase in the IN617 alloy. Image reproduced from (Wang et al., 2023).

The phase fraction versus temperature data for the IN617-M1 and IN617-M2 compositions were simulated using the TCFE13 database. These two alloy compositions were selected since the MD simulations performed on the modified alloy 617 compositions revealed the presence of high tensile strengths for the IN617-M1 and IN617-M2 compositions. The corresponding plots are presented in Figure 26(a) and (b). The TCFE13 database was not able to simulate the data throughout the temperature range (room temperature to melting point) for the IN617-M1 alloy composition, while the same database was successful in predicting the full temperature range for the IN617-M2 composition. This could again be attributed to the fact that the Fe/Steels database does not contain data for nickel alloys and is not intended for use with nickel alloys. The melting points of IN617-M1 and IN617-M2 are found to be 1267°C and 1280°C, respectively.

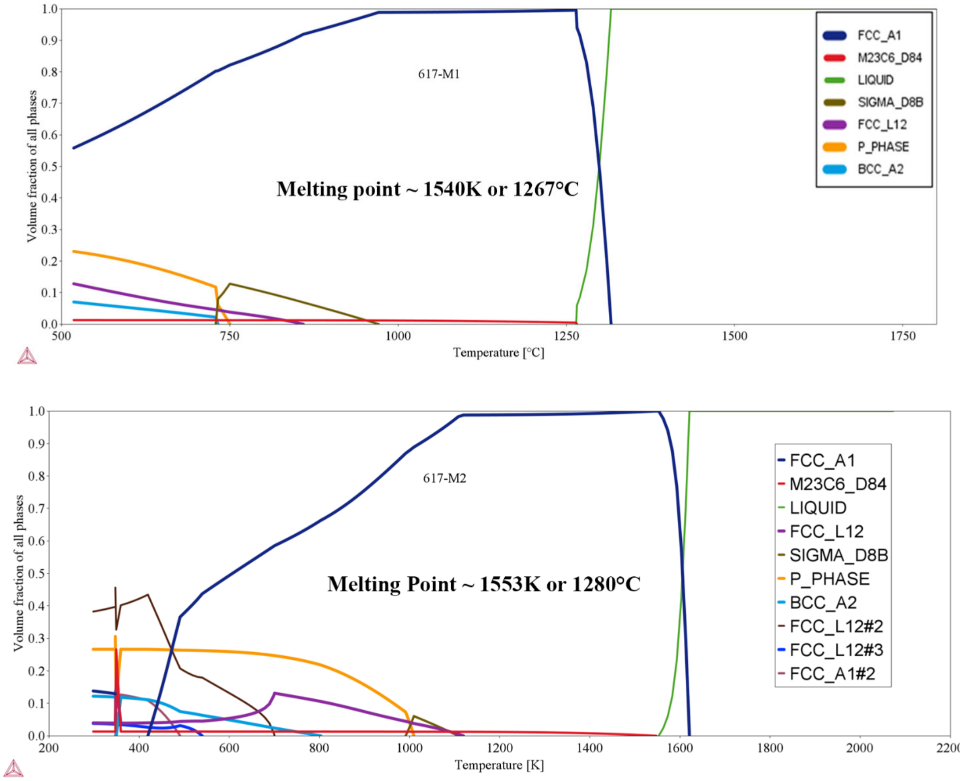

Figure 26. Phase fraction versus temperature plots for (a) IN617-M1 and (b) IN617-M2 simulated using the TCFE13 database and Thermo-Calc 2024a.

5.3 Experimental Validation of the MD Simulations

The IN617-M1 alloy recommended from the results of MD modeling was produced using two different experimental techniques: traditional casting in an induction furnace and solid phase alloying through FSC. For both approaches, wrought IN617 was turned into chips with lengths of 4.5 ± 0.7 mm and widths of 1.5 ± 0.3 mm on a milling machine prior to mixing with the other elements to encourage a more homogenous product. Both methods are described in detail in this section.

5.3.1 Casting Using an Induction Furnace

Modifications of IN617 were made by adding pure elemental metals of Fe (99.99), Mn (99.95), Cr (99.99), Ni (99.995), Mo (99.95), Ti (99.995), and Al (99.999) to Inconel 617 to achieve a desired composition as informed by computer modeling. New compositions were weighed on a Sartorius BCE224I-1S analytical balance to ±0.01 g of the required amount for a 20-gram charge. The pure metals and bulk IN617 chips shown in Figure 27 were die pressed in a ½″ die set to 12000 lb.; six pellets were pressed for a 20 g charge (Figure 28).

Figure 27. (Left) Elements with elemental purities of 4N to 5N. (Middle) IN617 filaments and chips. (Right) Alumina crucible with pure elements and IN617 ready for casting.

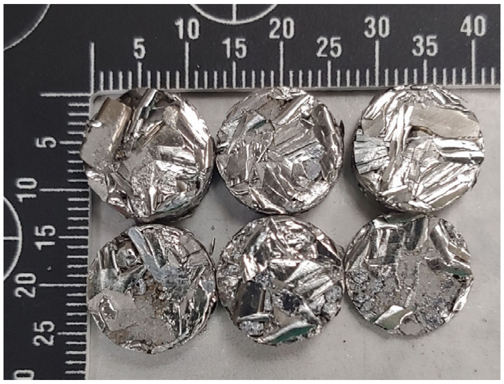

Figure 28. Pure metal components and Inconel 617 chips pressed into pellets.

The pellets were then loaded in an alumina crucible with a lid, which was placed inside a graphite crucible. The graphite crucible was then loaded into a 25 kW MTI Corp. EQ-SP-25A induction heater with a custom-made coil with 7 windings of 3/8″ copper tubing with an inner diameter of ~2.75″ and height of ~4″. The coil also contained insulation and an inert gas line, as shown in Figure 29. Argon was flowed prior to and during the melting procedure to reduce oxidation, and a type R thermocouple was inserted though top of the crucible setup to monitor, adjust, and record temperatures. An initial temperature evaluation study was performed with two thermocouples; it showed that the temperature varied by 40–80°C, the internal crucible being higher, as it had better contact with the bottom of the crucible. Graphite was used as a susceptor to reach temperatures exceeding 1700°C, which were held for 30 minutes to alloy the metal components, as shown in Figure 29(a) and (b). A temperature profile collected from a thermocouple placed on the graphite crucible is shown in Figure 29(c). The temperature was held for 30 minutes to allow the heat to soak into the inner alumina crucible and fully melt the charge inside. This holding time and target temperature were determined during previous testing. The furnace was allowed to cool to room temperature, and the ingot was extracted from the alumina crucible (Figure 30). The ingot was sectioned, mounted, and polished to 1 µm for further examination.

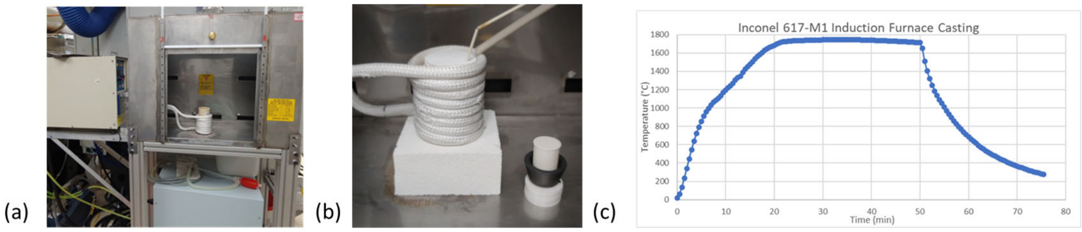

Figure 29. (a) MTI 25 kW induction furnace with the induction coil, coil, and insulation; (b) internal crucible setup used for alloying new metal compositions; and (c) temperature profile used to melt IN617-M1.

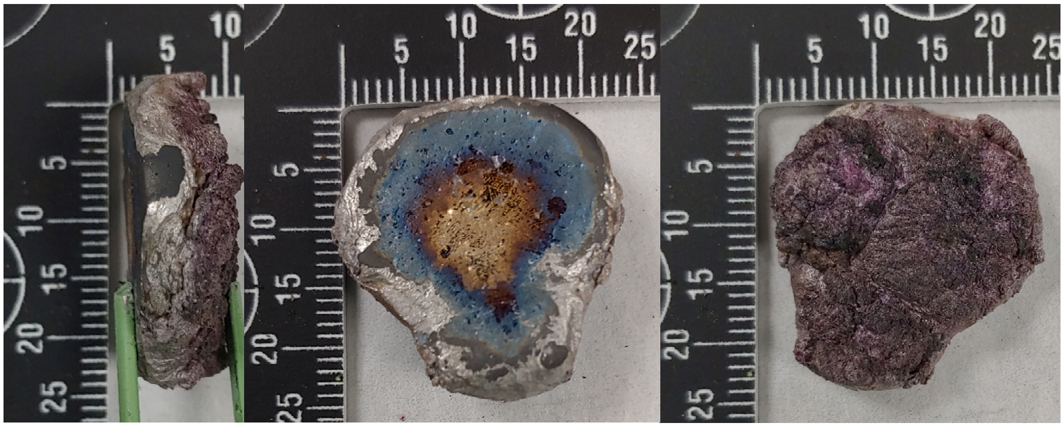

Figure 30. IN617-M1 ingot formed, max temperature of 1740°C, from left to right: side, bottom, and top of ingot.

The induction melter was able to produce an alloy and could be used for further studies. However, other methods may be more suitable to achieve the grain structure for ideal mechanical properties testing such as the ability to pour and cast to shape or the use of an arc melter for fast cooling and rapid turnaround.

5.3.2 Friction Consolidation and Solid Phase Alloying

IN617 chips were fabricated by machining Inconel 617 sheet metal using a milling machine. The IN617 chips were then mixed with 4N and 5N pure metals described previously in the quantities given in Table 12. Approximately 30 g of mixed metal chips were used for the consolidation experiment, as shown in Figure 31.

Table 12. Metal masses used for friction consolation and solid phase alloying runs.

Cr g	Ni g	Mn g	Mo g	Ti g	Al g	Fe g	IN617 g	Total, g
6.6876	12.8415	1.5006	2.2792	0.4132	0.2878	0.2171	5.9796	30.2066

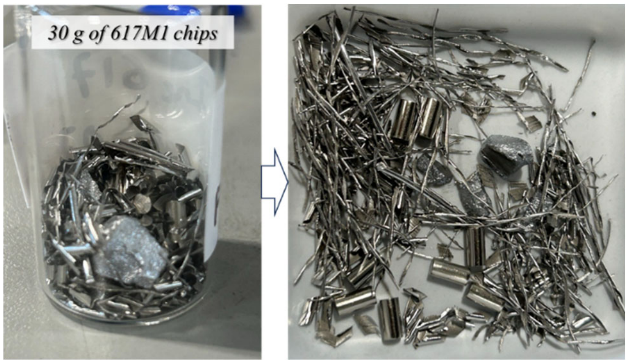

Figure 31. Mixture of Inconel 617 chips and pure metal alloying additions.

The friction consolidation and solid phase alloying experiments were performed using a Transformational Technology, Inc. LS2-2.5 FSW machine with a tungsten–rhenium (W–Re) tool coupled with a tool holder, as shown in Figure 32.

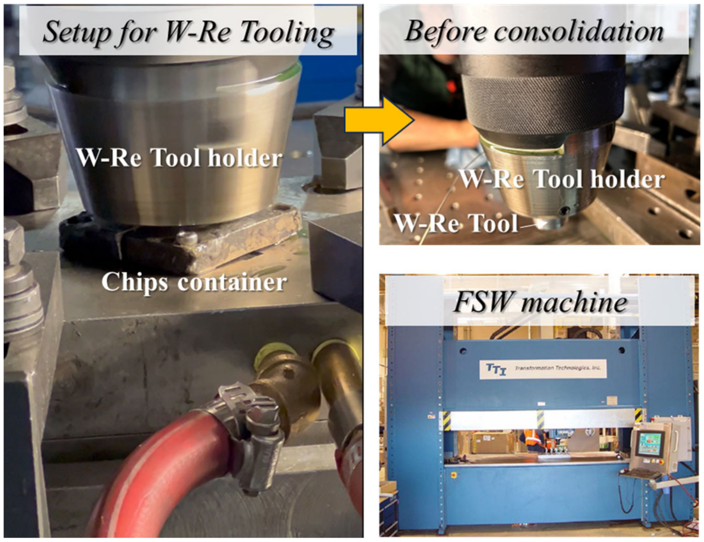

Figure 32. Friction consolidation and solid phase alloying setup.

The critical process variables during friction consolidation experiments include the loading force, rotation rate, and processing time. The tool/chip interface temperature is measured and monitored during friction consolidation and is a key parameter in determining the extent of consolidation. The temperature is directly influenced by the loading force and rotation rate during friction consolidation. The critical parameters of the two friction consolidation and solid phase alloying runs performed using IN617-M1 chips are listed in Table 13. A loading force of 65 kN was selected with rotation rates of 35–100 RPM, enabling us to maintain a consistent tool/chip interface temperature of ~900°C.

Table 13. Critical parameters for the friction consolidation of 617M1 alloy chips.

Weld #	Tool	Load (kN)	Rotation rate (RPM)	Temperature (°C)	Processing time (min)
2024-07-23-#000	W–Re	65	35 to 100	Up to 900	8

Machine data, including tool position (Z position), loading force (Z-axis force), temperature, rotation rate, spindle torque, and spindle power are plotted in Figure 33.

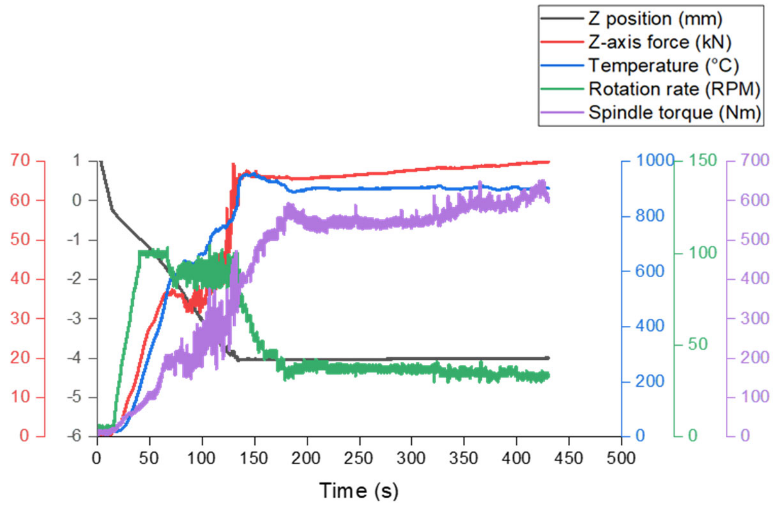

Figure 33. Machine data of the tool position (Z position), loading force (Z-axis force), tool/chip interface temperature, rotation rate, and spindle torque used for friction consolidation and solid phase alloying.

Side and top view images of the consolidated and alloyed chips are shown in Figure 34. Visual inspection of the consolidated and alloyed material suggests that a loading force of 65 kN was sufficient to obtain a fully consolidation material. This value was selected based on our previous experience with similar metal systems. The parameters that are typically adjusted to improve consolidation and alloying include the loading force/rotational speed combination and hence the temperature and process durations.

Figure 34. Top and bottom views of the friction consolidated and alloyed chips.

5.4 Characterization Results and Discussion

In this section, the characterization of the alloys produced from casting, FSC, and solid phase alloying are presented. The Vickers hardness was determined as an experimentally rapid method of obtaining information that can be correlated to the yield strength, which was used by the MD simulations to assess the different alloy modifications. SEM-EDS was also performed on each sample, providing insight into the grain boundaries, grain sizes, and chemical compositions. XRD was also performed on the cast sample to verify the phases present.

In preparation for SEM-EDS and Vickers hardness testing, the as-cast IN617-M1 and the friction stir alloying (FSA) IN617-M1 samples were mounted in epoxy and prepared metallographically with grinding and polishing. All samples were given a final polish using 1 μm diamond polishing paste and a colloidal silica (0.05 μm) polishing suspension. Once the final polishing was completed, samples were examined using Olympus DSX510 metallurgical microscope.

A JEOL 7600 SEM operating at 20 kV was used to capture backscattered images and perform compositional analyses of the as-cast IN617-M1 alloy using X-ray energy dispersive spectroscopy (XEDS, Oxford Instruments). Imaging and compositional analysis of the IN617-M1 FSC alloy were carried out using a ThermoFisher Apreo^{TM} 2 instrument.

Vickers microhardness measurements were performed using a Sun-Tec (model CM-802 AT) microhardness tester, operated with the ARS20 software for automated measurements. A load force of 300 grams-force was applied for a duration of 10 seconds for each indentation. A 2 × 2 array of indentations was performed on three regions of the IN617-M1 cast alloy (potential matrix); each indentation was separated by 0.5 mm. SEM-EDS analysis confirmed the target composition of the sample was approximately equivalent to the targeted M1 formulation. The friction alloyed sample (IN617-M1) was analyzed using a 2 × 10 array of indentations performed on two regions consisting of four lines indicated as L-1, L-2, L-3, and L-4.

Calibration checks for the hardness measurements were conducted using Sun-Tec calibration standard 297HV0.3 to verify that the instrument was in calibration. These checks confirmed that the hardness values measured were within ±2% of the calibration standard, ensuring the accuracy of the measurements.

PXRD using a D6 Phaser (Bruker Inc.) diffractometer was used to collect XRD patterns of Inconel 617 and our modified IN617-M1 sample. Both samples were mounted in epoxy, resulting in a high background, especially at low angles. The D6 Phaser is equipped with a theta/theta goniometer with a radius of 166.5 mm, Cu K_α radiation, and a 1.2 kW X-ray power generator. Prior to collecting the XRD patterns, samples were aligned, and the NIST SRM 640g internal standard was used for precision sample displacement correction. All XRD patterns were collected using 0.01° 2θ step size and 0.32 s time per step over 10–120° 2θ range. Each scan took ~1 h to complete.

5.4.1 Characterization Results of the IN617-M1 Cast Alloy

The results obtained from the mechanical testing and chemical analysis of the IN617-M1 cast alloy sample are discussed in the sections below.

5.4.2 Optical Imaging and Vickers Hardness of the IN617-M1 Cast Alloy

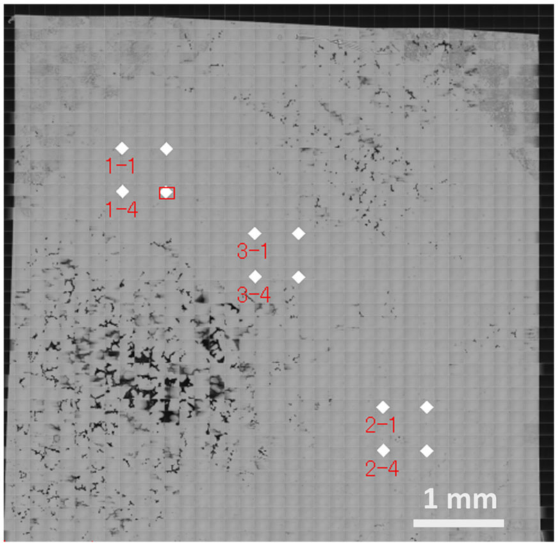

Figure 35. Optical micrograph of the as-cast IN617-M1 sample with indents for Vickers hardness measurements.

Figure 35 presents an optical micrograph of the as-cast IN617-M1 sample. Three regions (potential matrix) were selected, and a 2 × 2 array of indentations was performed on the selected regions to determine the hardness. The as-cast IN617-M1 sample had regions with porosity, while other regions were fully dense. The Vickers hardness data of the as-cast IN617-M1 sample is given in Table 14. The indentation regions are indicated in Figure 35.

The average hardness values obtained from the three arrays of indents for the cast sample are given in Table 14. All three averages are self-consistent with each other, with an average of 194.89 ± 9.71 HV.

Table 14. Vickers hardness values for the as-cast IN617-M1 alloy for the indentation regions marked in Figure 35.

Indentation Region	Vickers Hardness, HV	Average Vickers Hardness, HV	Average of all the Readings, HV
1	199.49	199.76 ± 11.51	194.35 ± 9.71
	212.52		
	181.48		
	205.53		
2	193.47	197.04 ± 2.08	
	198.51		
	197.78		
	198.38		
3	185.5	187.88 ± 8.27	
	201.97		
	181.59		
	182.45		

5.4.3 XRD of the IN617-M1 Cast Alloy

The XRD patterns of IN617 and our Mn-rich IN617-M1 modified alloy is shown in Figure 36. Both alloys show similar solid solution phases (fcc phases), with a peak shift to low angles in IN617-M1, suggesting a larger lattice parameter than that of the unmodified IN617 sample. The increase in the lattice parameter may reflect the incorporation of Mn into the IN617 matrix, while the peak broadening is likely due to a smaller crystallite size and higher lattice strain in the sample compared to the unmodified IN617 material.

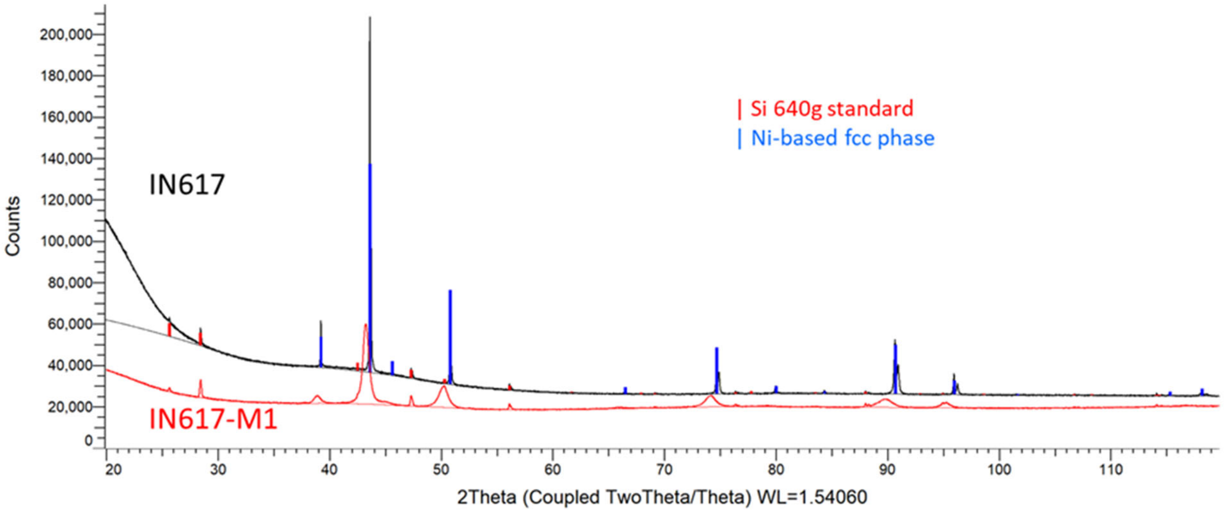

Figure 36. Comparison of IN617-Co 12.5 wt% and the modified IN617-M1-Co 2.5 wt% alloy sample from casting at ~1700°C using an induction furnace. Peaks correspond to the Si standard (NIST SRM 640g), and the fcc phase is denoted by red and blue tick marks, respectively.

5.4.4 Compositional Analysis of the IN617-M1 Cast Alloy

Figure 37 presents the XEDS compositional maps of the backscattered electron (BSE) micrographs of the as-cast IN617-M1 sample. Six regions/points were identified from the sample, and detailed analyses were performed. The primary purpose was to determine whether the composition of the matrix hit the composition close to M1 target (Co substitution by Mn). The unmelted material identified as Block 1 was observed to be Ti enriched, which has a higher melting point than the base alloy IN617-M1. The precipitates (ppt) decorating the grain boundaries (GBs) were observed to be Cr, Mo and Mn enriched. A detailed compositional analysis of the identified region is presented in Table 15. From this table, the matrix composition is found to be very close to the IN617-M1 composition.

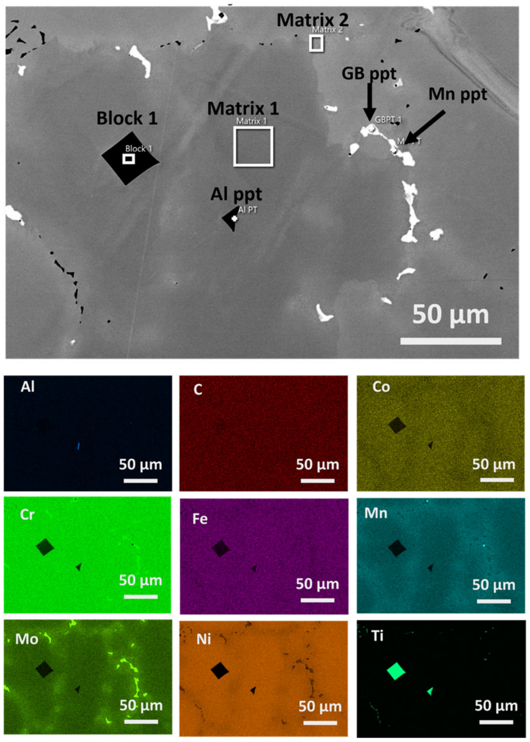

Figure 37. XEDS compositional maps of the backscattered electron micrographs of the IN617-M1 cast alloy.

Table 15. Elemental compositions of the regions highlighted in Figure 37. The IN617-M1 composition is included for comparison.

Location	C	Al	Ti	Cr	Mn	Fe	Co	Ni	Se	Mo	Total
IN617-M1	0.06	1.2	0.3	26.6	5	0.9	2.5	53.6	-	9.5	99.66
Map Sum 1	0.06	0.71	0.80	27.28	4.61	1.65	2.28	52.26	0.00	10.35	100.00
Matrix 1	0.06	0.67	0.07(a)	27.31	3.69	1.83	2.51	55.98	0.00	7.87	100.00
Block 1	0.06	0.00	87.13	11.37	0.12(a)	0.00	0.00	0.63	0.00	0.69	100.00
Matrix 2	0.06	0.65	0.06(a)	28.33	5.85	1.38	2.02	48.01	0.00	13.64	100.00
Mn PT	10.1	0.42	0.00	5.87	31.09	0.33	0.27	5.99	26.16	19.78	100.00
GBPT 1	10.07	0.17	0.00	29.51	3.24	0.95	1.57	25.10	0.00	29.39	100.00
Al PT	0.06	22.78	62.92	9.97	0.20(a)	0.16(a)	0.15(a)	2.96	0.00	0.79	100.00

(a) Trace elements below the confidence threshold

5.4.5 IN617-M1 Friction Stir Alloying

The results obtained from the mechanical testing and chemical analyses of the IN617-M1 friction stir alloy sample are discussed in the sections below.

5.4.6 Optical Imaging and Hardness

Figure 38(a) presents an optical micrograph of the FSA IN617-M1 sample along with the indents performed, and Figure 38(b) presents the Vickers hardness. Ten indentations were performed along each of four lines identified as L-1, L-2, L-3, and L-4 on the sample to determine the variation in hardness parallel to the flat surface (top) of the sample, which is assumed to be the starting point of the FSA fabrication process. In general, the FSA IN617-M1 sample was observed to show higher hardness as compared to that of the as-cast IN617-M1 sample.

Table 16. Summary of the Vickers hardness values measured for both cast and FSA samples.

Sample Type	Array of Indents	Indented Region	Vickers Hardness, HV Load 300 gf, Dwell Time 10 s, Spacing 0.5 mm	Average Hardness, HV
As-Cast IN617-M1	2 × 2	1	199.76 ± 11.51	194.35 ± 9.71
		2	197.04 ± 2.08	
		3	187.88 ± 8.27	
FSA IN617-M1	2 × 10	1	348.18 ± 36.65	346.68 ± 45.64
		2	345.17 ± 53.10	

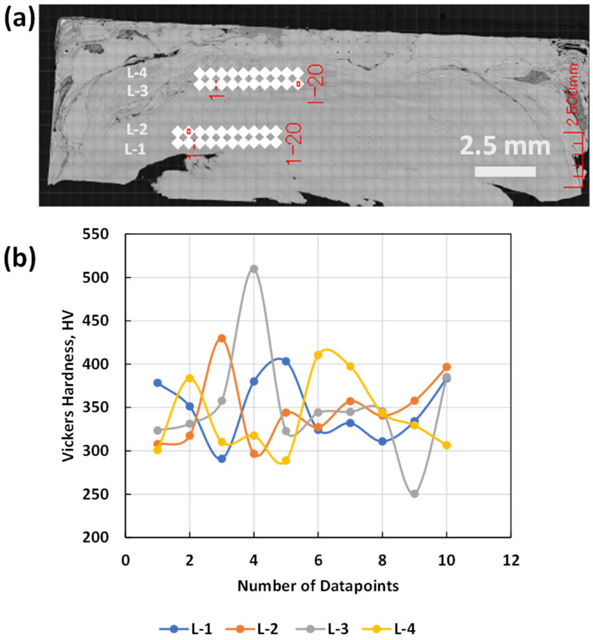

Figure 38. (a) Optical micrograph and indents and (b) Vickers hardness of the FSA IN617-M1 sample.

5.4.7 Microstructural Analysis of FSA IN617-M1

Figure 39(a–c) present BSE micrographs of the FSA IN617-M1 sample. The lower magnification images in Figure 39(a–b) show the variation in image contrast that represents inhomogeneity in the alloy. However, the higher magnification image in Figure 39(c) shows the formation of small equiaxed grains in the alloy with a significant amount of porosity. The grain size was measured using ImageJ and was observed to be 1.67 ± 0.39 µm. The higher hardness observed in the FSA IN617-M1 sample could potentially be attributed to this small grain size. Figure 39(d) is an inverse pole figure from the same alloy showing the distribution of fcc grains. From these results, it can be inferred that the FSA process is able to form alloys with uniform grain sizes, but further process optimization is needed for macroscopic chemical homogeneity.

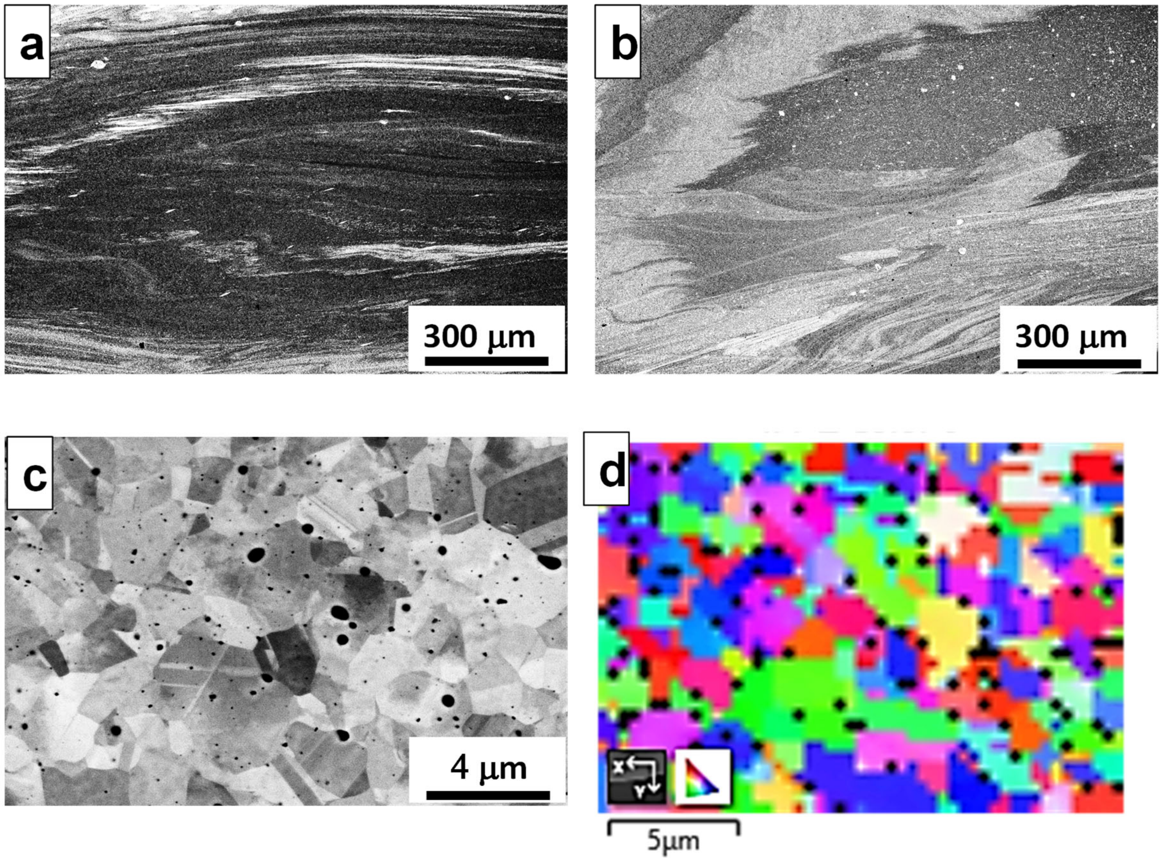

Figure 39. (a–c) BSE micrographs of the FSA IN617-M1 sample and (d) inverse pole figure.

5.4.8 Compositional Analysis of IN617-M1

A localized area in the FSA IN617-M1 sample was analyzed to determine its chemical composition, as presented in Figure 40. The compositional evaluation was carried to confirm the presence of all intended elements for IN617-M1 chemistry. The observed uniformity of composition across this smaller region indicates that further process parameter optimization is required for fabricating dense homogeneous products. This localized region also has a composition close to that of IN617-M1 (Table 17). The presence of Si at the pores is mostly due to the residual Si used for polishing the samples.

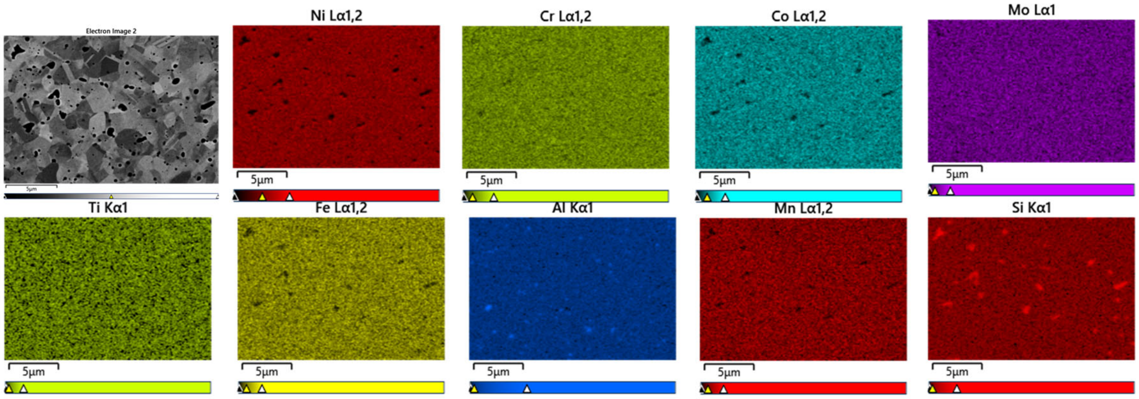

Figure 40. XEDS compositional maps of backscattered electron micrographs of the IN617-M1 FSA sample.

Table 17. Chemical composition of the IN617-M1 FSA sample corresponding to Figure 40.

Ni	Cr	Mn	Fe	Co	O	Mo	Al	Si	Ti
54.14	33.51	4.23	3.22	2.67	1.44	0.42	0.25	0.1	0.03

5.5 MD Performance Conclusions

Krishna et al. (2010) reported the Vickers hardness of solution annealed IN617 to be 186.6 ± 5 HV when measured with a load of 20 kgf. This value is comparable to the as-cast IN617-M1 hardness value of 194.35 ± 9.7 HV obtained in this study. Table 18 summarizes the grain size in micrometers and the Vickers hardness values (HV) of the MD informed IN617-M1 formulation results for both the as-cast alloy and FSA samples, along with unmodified IN617.

Table 18. Comparison of MD performance compared to experimental data.

Alloy Studied	Grain Size, μm	Hardness, HV	Ref
As-cast IN617	10.2	230.7 ± 6.8	van Rooyen et al. (2024)
Solution Annealed IN617	120	186.6 ± 5	Krishna et al. (2010)
FSA IN617	1.35	356.5 ± 15.8	van Rooyen et al. (2024)
As-cast IN617-M1	~800	194.35 ± 9.71	Burns et al. (2024)
FSA IN617-M1	1.67 ± 0.39	346.68 ± 45.64	Burns et al. (2024)

IN617-M1 shows considerable promise as a material, particularly when subjected to advanced processing methods like FSA, due to the grain refinement as an additional strengthening mechanism. In the as-cast condition, IN617 exhibits a hardness of 230.7 ± 6.8 HV with a grain size of 10.2 μm, while as-cast IN617-M1 has a lower hardness of 194 ± 9.71 HV, accompanied by a much larger grain size of 800 μm. This reduction in hardness for M1 is likely due to the significant difference in grain size, as smaller grains typically provide more barriers to dislocation movement, resulting in higher hardness. The larger grain size in IN617-M1 naturally leads to lower hardness, but this doesn't necessarily indicate poor performance, especially considering the potential for grain refinement through processing.

When subjected to FSA, both IN617 and IN617-M1 show significant improvements in hardness due to grain refinement. FSA IN617 achieves a hardness of 356.49 ± 15.8 HV with a grain size of 1.35 µm, while FSA IN617-M1 reaches a hardness of 346 ± 45 HV with a slightly larger grain size of 1.67 µm. The minimal difference in hardness between the two alloys after FSA processing suggests that M1 can achieve nearly equivalent mechanical performance to IN617 when its grain structure is refined. This is consistent with the MD predictions, where M1 exhibited a slightly higher tensile strength (12.33 GPa) compared to IN617 (11.82 GPa), indicating its potential for superior mechanical properties.

In summary, while as-cast IN617-M1 exhibits lower hardness due to its coarser grain structure, the alloy shows great potential when processed to refine its microstructure. The close match in hardness between FSA IN617 and FSA IN617-M1, along with the MD predictions of a higher tensile strength for M1, suggests that M1 is as promising as IN617 for applications requiring high strength, particularly when processing techniques like FSA are employed to optimize its grain structure.

5.6 New Alloy Development Using Multiobjective Bayesian Optimization

The objective of new alloy development is to develop new alloys having high hardness and yield strength without CMs (i.e., nickel and cobalt) using a multiobjective Bayesian optimization (MOBO) technique. The HEA system within which new compositions were developed is Fe–Cr–Cu–Al–Nb–Ta–Ti–V–Zr–Mo–W–Mn. Both objectives are optimized by learning the Pareto front (i.e., learning a set of nondominated solutions where each point on the Pareto front is a compromise between multiple objectives—namely, hardness and yield strength).

Most machine learning (ML) research on developing HEAs has been focused on predicting a single physical property like hardness, yield strength, or Young’s modulus (Khakurel et al., 2021; Taufique et al., 2024; Wen et al., 2019). There has been a gradual shift to leverage ML and statistical methods to optimize two or more physical properties for an HEA system using methods like generative adversarial networks (GANs), multiobjective optimization techniques like the nondominated sorting genetic algorithm (NSGA) and Bayesian optimization (Li et al. 2024; Shi et al., 2023; Solomou et al., 2018). In this study, MOBO was used to develop new material compositions without CMs—nickel and cobalt—with maximum yield strength and hardness. Two neural network models were developed to predict the yield strength and hardness using two separate datasets available on yield strength and hardness (Taufique et al., 2024), and these models were used to predict the hardness and yield strength of new compositions developed through MOBO. From all the new compositions developed, optimal solutions were learned from the Pareto front.

5.6.1 Design Strategy

The design strategy used to develop new alloys using MOBO is depicted in the Figure 41. A database of alloys was curated, which had both their hardness and yield strength data measured at room temperature. These data were used to train a Gaussian process model (i.e., a surrogate model to model the unknown objective function for both the hardness and yield strength). Once a surrogate model was established to model the objective function from the curated data, an acquisition function used the surrogate model to establish the next point or set of points in the search space within the bounds and constraints.

The hardness and yield strength models developed separately are used to predict the hardness and yield strength for new candidate/candidates. A separate hardness and yield strength database is used to develop these separate models for the hardness and yield strength. The newly generated candidates and their predicted hardness and yield strength values are added back to original curated dataset, and the whole cyclic process of approximating the unknown objective function and predicting next set of candidate/candidates using the acquisition function and their hardness and yield strength values is repeated for several iterations. At the end of the scheduled number of iterations, the hardness and yield strength of all curated alloys and new compositions are plotted together to extract the Pareto front. The solutions obtained in the Pareto front are to be analyzed using MD. The aim is to fabricate and test the hardness and yield strength of those solutions on the Pareto front (nondominated solutions) whose performance can be validated using MDs.

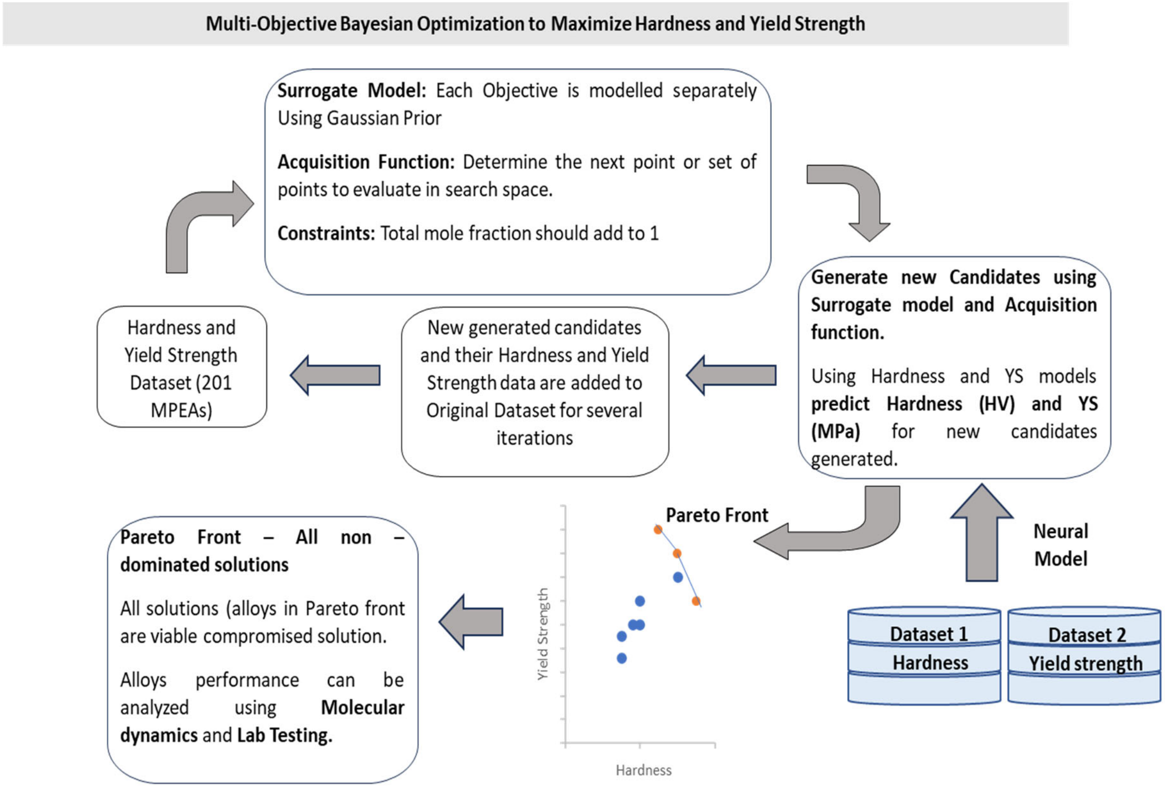

Figure 41. Multiobjective Bayesian optimization framework.

5.6.2 Hardness and Yield Strength Model

Data on yield strength (MPa) and hardness (HV) used are previously collected data from the existing literature (Couzinié et al., 2018; Gorsse et al., 2018; Taufique et al., 2024). The dataset for the yield strength model contains yield strength data for 160 multiprincipal element alloys (MPEAs) and HEAs curated from literature (Taufique et al., 2024). The dataset for the hardness model contains hardness data on 243 MPEAs and HEAs curated from the literature (Taufique et al., 2024).

Neural models were used train two separate models to predict the yield strength and hardness using the curated yield strength and hardness data from their respective datasets and 14 computed features related to MPEAs. These features have been found to have an effect on the mechanical properties of MPEAs (Khakurel et al., 2021; Roy et al., 2022a). The data on elemental values for features like the valence electron concentration (VEC), Pauling and Allen electronegativities, enthalpy, atomic radii, and lattice constants were gathered from various domain-specific sources (Takeuchi and Inoue 2005). These 14 features were computed for all alloys using Python scripts; details on the 14 features computed are available in Table 19.

Table 19. Formulas used to compute the input features of the hardness and yield strength models.

Feature Description	Formula
Difference in Pauling Electronegativity	$\Delta x_{\text{pauling}} = \sqrt{\sum_{i=1}^{n} C_i (x_i - \bar{x})^2}$ x_i – Pauling electronegativity of element C_i – Molar ratio of each element $\bar{x} = \sum_{i=1}^{n} C_i x_i$
Difference in Allen Electronegativity	$\Delta x_{\text{allen}} = \sqrt{\sum_{i=1}^{n} C_i (x_i - \bar{x})^2}$ x_i – Allen electronegativity of element C_i – Molar ratio of each element $\bar{x} = \sum_{i=1}^{n} C_i x_i$
Mixing Entropy	$S_{\text{mix}} = -8.314 \sum_{i=1}^{n} C_i ln C_i$ C_i – Molar ratio of each element
Mixing Enthalpy	$H_{\text{mix}} = 4 \sum_{i=1,j>i}^{n} C_i C_j H_{i-j}^{\text{mix}}$ C_i, C_j – Molar ratio of each element
Difference in Atomic Radii	$\delta = \sqrt{\sum_{i=1}^{n} C_i \left(1 - \frac{r_i}{\bar{r}}\right)^2}$ r_i – Atomic radius of element C_i – Molar ratio of each element $\bar{r} = \sum_{i=1}^{n} C_i r_i$
Difference in Lattice Constants	$\Delta a = \sqrt{\sum_{i=1}^{n} C_i (a_i - \bar{a})^2}$ a_i – Lattice constant of element C_i – Molar ratio of each element $\bar{a} = \sum_{i=1}^{n} C_i a_i$

Feature Description	Formula
Difference in Melting Temperature	$\Delta T_{\mathrm{m}} = \sqrt{\sum_{i=1}^{n} C_i (T_i - \bar{T})^2}$ T_i – Melting temperature of element C_i – Molar ratio of each element $\bar{T} = \sum_{i=1}^{n} C_i T_i$
Parameter - λ	$\lambda = \frac{S_{\mathrm{mix}}}{\delta^2}$
Parameter - Ω	$\Omega = \frac{T_{\mathrm{m}} S_{\mathrm{mix}}}{\lvert \Delta H_{\mathrm{mix}} \rvert}$
Average Lattice Constant	$a_{\mathrm{m}} = \sum_{i=1}^{n} C_i a_i$ a_i – Lattice constant of element C_i – Molar ratio of each element
Valence Electron Concentration	$VEC = \sum_{i=1}^{n} C_i VEC_i$ VEC_i – VEC of element *i* C_i – Molar ratio of each element
Difference in Shear Modulus	$\Delta G = \sqrt{\sum_{i=1}^{n} C_i (G_i - \bar{G})^2}$ G_i – Shear modulus of element C_i – Molar ratio of each element $\bar{G} = \sum_{i=1}^{n} C_i G_i$
Average Shear Modulus	$G_m = \sum_{i=1}^{n} C_i G_i$ G_i – Shear modulus of element C_i – Molar ratio of each element

The neural network constructed to train two separate models for predicting the hardness and yield strength is a fully connected network consisting of a sequence of layers. A sequential model is created by adding one layer at a time; the neural model has total of five layers. The 14 computed features from Table 19—namely, the difference in Pauling electronegativity, difference in Allen electronegativity, mixing entropy, mixing enthalpy, difference in atomic radii, difference in lattice constants, difference in melting temperature, average lattice constant, VEC, difference in shear modulus, average shear modulus, and the parameters λ and Ω are passed on as input to the first layer. The first two hidden layers have 32 nodes each, followed by two more layers having 16 nodes each. All four hidden layers have rectified linear unit (ReLU) activation function. The fifth layer is the output layer having one node for the hardness. The neural network is compiled using the mean squared loss as a loss function and the Adam optimizer. Once the neural network is defined and compiled, the training is done on training data and then tested on the test data to measure the performance of the model.

The hardness dataset consisting of hardness data for 243 MPEAs is split into training and test data containing 202 and 41 MPEAs, respectively. Similarly, the yield strength dataset consisting of yield strength data for 160 MPEAs is split into training and test data containing 128 and 32 MPEAs, respectively. The training data are used to train the hardness model, and the model performance is gauged using the test data. The coefficient of determination (R^2) is used to measure the performance of neural network trained on the test data. Table 20 contains the details of the performance of the hardness and yield strength neural models on the test data.

Table 20. Performance of the hardness and yield strength models.

Model	R^2 Accuracy
Hardness Neural Model	84.09%
Yield Strength Neural Model	61.49%

5.6.3 Multiobjective Bayesian Optimization

Bayesian optimization is a technique used for the optimization of black box functions. A black box is system whose internal working is unknown, and the only available information on hand is the input and output to the box. Bayesian optimization helps in optimizing this unknown function, which is also referred to as the objective of the optimization. In this study, the MOBO problem involves optimizing multiple objectives to develop new alloy compositions in the elemental space of Fe–Cr–Cu–Al–Nb–Ta–Ti–V–Zr–Mo–W–Mn by maximizing the hardness and yield strength simultaneously. In a multiobjective optimization problem, both objectives compete (i.e., when one objective is maximized or minimized, the other objective suffers, and vice versa). Hence, multiobjective optimization generally involves reaching a compromise or trade-off between both objectives. This set of compromised or nondominated solutions is referred to as a Pareto front (Shi et al., 2023).

MOBO consists of two parts—first to develop a surrogate model (typically, a Gaussian process model is used) to fit the known data available and predict the outcome in the unknown space. The surrogate model computes a posterior probability distribution. This distribution is an estimate of the data and includes the uncertainty associated with the distribution (Ghorbani et al., 2024; Schulz et al., 2017). The second part to MOBO is to design an acquisition function to deduce the new set of candidates and evaluate the target property based on known information available through the posterior distribution. An acquisition function finds the new candidates by balancing the exploration of unknown regions and the exploitation of regions, which maximizes the target objectives (Brochu et al., 2010; Rasmussen et al., 2003).

A dataset is curated from the literature containing hardness and yield strength data for 201 MPEAs (Gorsse et al., 2018; Li et al., 2023). This curated dataset is contained in a 23-element space namely Ni–Co–Fe–Cr–Cu–Al–Nb–Ta–Ti–V–Zr–Hf–Mo–Si–W–Re–C–Y–Sn–Pd–Mn–Sc–Zn. The mole fractions of the elements contained in each of the 210 MPEAs is computed and passed on as inputs to the developed MOBO model.

In this study, MOBO is implemented to maximize the hardness and yield strength using BoTorch. BoTorch is a Python framework developed by Facebook built on top of PyTorch. It contains application programming interfaces (APIs) that aid in implementing single- and multiobjective Bayesian problems. Two surrogate models are implemented to fit—one each for hardness and yield strength—using the SingleTaskGP API. Then, both surrogate models are combined into one multioutput model using ModelListGP, where each target property is modeled independently. The acquisition function is then implemented using parallel q-expected hypervolume improvement (qEHVI) (Daulton et al., 2020) to generate a new composition with the objective of optimizing the maximization of the hardness and yield strength into one. The hypervolume is defined as a Lebesgue measure dominated by a certain Pareto front and bounded below by a reference point (Shi et al., 2023). The new candidate/composition performance on the Pareto front is evaluated through hypervolume improvement (HVI) (i.e., solutions on the Pareto front should have a higher hypervolume, and all solutions on the Pareto front should have similar hypervolume contributions to be considered nondominated solutions). The new alloy composition generated using MOBO is being explored in a reduced elemental space of Fe–Cr–Cu–Al–Nb–Ta–Ti–V–Zr–Mo–W–Mn. It is implemented by setting the bounds of the above elements to be within 0 to 1 (representing the mole fractions of each element) and the other elements to be 0 and linearly constrained for the total mole fraction of all elements in a new alloy being generated to add up to 1. For the new alloy composition obtained through MOBO, 14 features from Table 19 are computed, and its hardness and yield strength value are computed using the hardness and yield strength models, respectively. This newly generated data point with its computed hardness and yield strength values are appended to the original dataset of 201 MPEAs. The posterior probability distribution of the surrogate models is updated, and the acquisition function uses the updated model to determine the next point to evaluate. This cyclic process of adding the new composition to the training data, updating the surrogate model, and querying the next sample is repeated for 200 iterations; each iteration generates four new compositions in parallel using the batch optimization technique. A total of 800 new compositions are generated, and after plotting the hardness and yield strength objectives, three compositions are found in the Pareto front. Figure 42 shows the hardness and yield strength values of old and new MPEAs. Table 21 contains the details about these three compositions on the Pareto front.

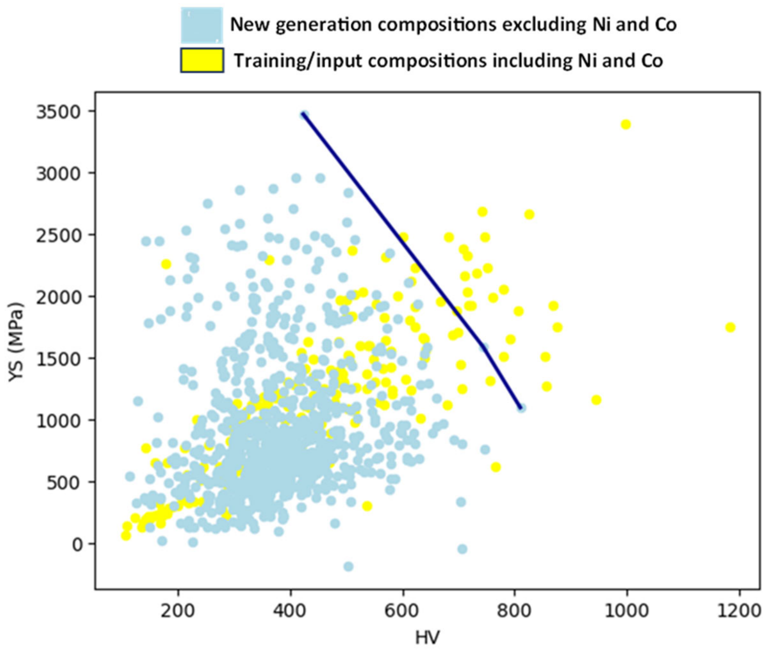

Figure 42. Hardness versus yield strength of the alloys in the original training data represented by yellow dots and new compositions suggested by Bayesian optimization represented by blue dots. The solid blue line represents the alloys in the Pareto front.

Table 21. Details of three compositions on the Pareto front and their predicted hardness and yield strength (YS).

Fe	Cr	Cu	Al	Nb	Ta	Ti	V	Zr	Mo	W	Mn	Pred HV	Pred. YS
0.122	0.046	0.006	0.001	0.080	0.071	0.077	0.068	0.100	0.234	0.175	0.0199	424	3468
0.223	0.331	0.046	0.027	0.009	0.031	0.141	0.068	0.013	0.102	0.010	0.0003	744	1589
0.240	0.020	0.027	0.036	0.091	0.077	0.021	0.005	0.100	0.040	0.342	0.0005	810	1097

5.6.4 New MOBO Alloys: Next Actions

The predictions made through MOBO need to be verified by conducting simulations using MD and by experimentally developing the alloys and measuring their hardness and yield strength values. Moreover, the MOBO model and the models to predict the hardness and yield strength need to be further optimized. Current neural models developed for predicting the hardness and yield strength are not very high performing models; hence, the predicted hardness and yield strength values have a higher prediction uncertainty associated with them. To derive more reliable and accurate predictions, the aim is to explore other tree-based ensemble models and kernel models in future work. The accuracy of these hardness and yield strength models has a major impact on the MOBO model. For the new compositions generated, we need the predictions to be as close to accurate as possible, and a higher uncertainty might hinder the predictions and the overall performance obtained from MOBO. The current MOBO model just takes the mole fraction ratios as inputs to the model, whereas the hardness and yield strength models take the 14 features in Table 19 as inputs to their model. These inconsistencies in inputs given to MOBO and the hardness and yield strength neural models might also be hampering the overall performance of MOBO. In future work, developing models having consistent inputs to the MOBO, hardness, and yield strength models needs to be explored. There are many new acquisition functions that can be explored in MOBO in addition to the qEHVI acquisition function, like upper confidence bound (UCB), mutual information (MI), parallel q-noisy expected hypervolume improvement (qNEHVI) (Daulton et al., 2021), and many more. Overall, the MOBO model developed in this study is in its nascent stage of implementation and needs further optimization to derive more reliable new compositions from it.

6.0 Conclusions and Recommendations

The outcomes and conclusions from the AMMT program's critical minerals (CM) studies are described in strategic reports issued by Hartmann et al. (2022, 2023) and in detailed experimental design and execution reports by (1) Burns et al. (2024), regarding the replacement of high-risk CMs such as cobalt and subsequently niobium with more abundant minerals, and (2) van Rooyen et al. (2024), concerning the minimization and utilization of CM waste streams. This report summarizes the AMMT program’s work as detailed in the aforementioned body of work. Key project findings are as follows: The AMMT strategy to decrease nuclear material vulnerability due to CM supply and the economic impact focuses on (1) Co, as a short-term (2020–2050) and medium-term (2025–2035) high supply risk, and (2) Ni, a near-critical material for the near term, but a high critical material for the medium term (2025–2035).

- Recycling 70% of certain alloying metals can delay their peak production by about 50 years. Experimental feasibility studies show that the recycling of solid waste through the consolidation of machining chips or offcuts and liquid waste metal recovery through aqueous separation can have positive impacts for nuclear material supply risks. This process shows the benefit of a full circular process, with no waste of CMs, and can be repeated several times. FSC has been considered in this work because it has been reported to be a reproducible process and can refine the microstructure without producing unwanted textures, thereby reducing anisotropy.
- Three nuclear grade materials have been processed by FSC to evaluate the feasibility of this process for the efficient recovery of materials: (1) Alloy 709 (Fe–20Cr–25Ni with other minor elements such as Mo, Mn, Nb, N, C, etc.) is a 20Cr–25Ni austenitic grade stainless steel and has been considered for SFRs. (2) Alloy 316H is a high carbon modification of Alloy 316 developed for use at elevated temperatures. The alloy is used for structural and pressure vessel applications at temperatures above 500°C and is currently considered for multiple reactor types. (3) Alloy 617 is a nickel–chromium–cobalt alloy that has many outstanding properties such as high-temperature oxidation resistance and corrosion resistance in various corrosive aqueous environments. It is the sixth material cleared by the BPVC for use in high-temperature nuclear reactors.
- In the FSC process, metal chips of all three alloys were successfully solid-state-consolidated into dense products after limited optimization of process parameters. The extent of consolidation in A709 and IN617 are higher compared to that in 316H. Further, the real-time density evolution was measured, revealing the mechanism of the consolidation process, which will allow for future upscaling benefits. In all three alloys (A709, 316H, and IN617) that were FSC-processed, the grains are refined in size and nearly equiaxed, removing any anisotropy from the starting material. In A709, the grain size decreased by nearly 80 percent (from 10 to 2 µm). Similarly, the grain size reduction was nearly 88 percent in IN617 (from 10.2 to 1.2 µm). Subsequently, the hardness of the FSC product substantially increases because of grain boundary strengthening (Hall–Petch relationship).
- Adsorbents based on iMOFs were successfully designed for CM extraction from aqueous solution, thereby providing a pathway for future upscaling for salvaging dissolved Ni ions. This research has achieved its goal of showing the impact of novel applications of recycling technologies for solid and liquid wastes that can be upscaled for application. The uptake properties of the iMOFs were evaluated in terms of the adsorption capacity, removal efficiency, and kinetics. The adsorption capacity of the iMOFs towards nickel reaches 34.1 mg/g with a removal efficiency of >99.9%. Notably, complete removal of nickel takes place within 5 min, which is much faster compared to other adsorbents. Moreover, the iMOFs

can simultaneously coextract multiple minerals, proving their effectiveness as general adsorbents.

- The design of nuclear materials without critical elements as alloying elements is a part of the nuclear materials strategy to overcome CM scarcity. In this report, two approaches are evaluated—namely, (1) the replacement of critical elements as alloying elements in nuclear materials and (2) the design of new alloys that do not contain CMs as an alloying element.
- For the first approach, IN617 has been selected as an alloy system to substitute its high Co concentration using noncritical Mn. Inconel 617 is an alloy system that has been recently ASME-code certified for high-temperature nuclear systems (U.S. Office of Nuclear Energy, 2020); therefore, it was used in a feasibility study. A computational feasibility study of compositional changes to IN617 with simulation-generated stress–strain curves determined the impact that Co replacement with Mn has on the alloy's mechanical properties (e.g., tensile strength). For select compositions, phase diagrams were calculated, and for promising and similar results compared to the original alloy, experimental verification was performed. The phase diagrams and tensile simulations suggest that Mn substituted for Co will yield similar tensile strength and phase stability. The composition with the best combination of simulated oxygen penetration and tensile strength was down-selected for experimental fabrication and characterization. Two different fabrication methods were used to fabricate alloy samples: (1) casting and (2) FSC and alloying. The samples were then characterized using SEM-EDS, XRD (casting alloy only), and the Vickers hardness. IN617-M1 shows considerable promise as a material, particularly when subjected to advanced processing methods like FSA, due to the grain refinement as an additional strengthening mechanism.
- For the second approach evaluated herein, MOBO techniques were employed to design novel alloys for nuclear applications that do not contain the CMs nickel and cobalt while maximizing the alloys' yield strength and hardness. The material system within which new compositions were developed for this study is Fe–Cr–Cu–Al–Nb–Ta–Ti–V–Zr–Mo–W–Mn. Predictions made through MOBO need to be verified by conducting simulations using MD and by experimentally producing the alloys and measuring their hardness and yield strength values.

In conclusion, a significant number of alloying elements of nuclear materials are classified as scarce CMs with high economic risk and supply chain disruptions, and the supply of critical raw materials is highly concentrated, posing risks to supply chain reliability, affordability, and sustainability. The feasibility experimentation shows that it is viable to design new material types and minimize current waste of these alloying elements. This report showed that action needs to be taken into consideration in the early stages of design and development to minimize the impact on the current fleet and new reactor types. In conclusion, the research successfully showcased novel recycling technologies for solid and liquid waste, with promising upscaling opportunities for various industrial applications.

7.0 Reports, Publications and Presentations

Three reports have resulted to date from this project:

- “Draft Critical Minerals Evaluation Report,” PNNL-33356, M3CR-22PN0401018, September 2022, Thomas Hartmann, Stuart Maloy, Isabella van Rooyen
- “Strategic Plan: Decrease Critical Minerals Waste through Enabling Advanced Manufacturing Techniques,” Revision 1, PNNL-34225, M2CR-22PN0401011, July 2023, Thomas Hartmann, Praveen K. Thallapally, Isabella van Rooyen
- “Nuclear Energy Critical Material Waste Minimization Enabled by AM Techniques,” PNNL-36049, M3CR-22PN0401013, May 2024, IJ van Rooyen, T Wang, S Meher, D Garcia, P Thallapally, M Nartu, J Dos Santos, QRS Miller, C Silva, T Hartmann, SHR Shin.
- Development Results on Replacement Materials for Current Scarce or High Supply Chain Risk Materials,” PNNL-36491, M3CR-22PN0401015, August 2024, Carolyne Burns, Ankit Roy, Steven Livers, Subhashish Meher, Asif Mahmud, David Garcia, Pratikshya Meher, Benjamin Lund, Mohan Nartu, Jorge Dos Santos, Thomas Hartman, Isabella van Rooyen

Two conference presentations have resulted to date from this project:

- Chinthaka Silva, Ankit Roy, Carolyne Burns, Benjamin Lund, Steven Livers, Thomas Hartman, Mohan Nartu, Subhashish Meher, Isabella van Rooyen, “Development of Nuclear Reactor Structural Materials with Low Critical Mineral Concentrations,” MS&T2024: Where Materials Innovation Happens, October 6–9, 2024 | David L. Lawrence Convention Center | Pittsburgh, Pennsylvania, USA
- Isabella van Rooyen, Thomas Hartman, Praveen K. Thallapally, Chinthaka Silva, Ankit Roy, Subhashish Meher, Jorge Dos Santos, Carolyne Burns, Ben Lund, Steven Slivers, “Impact of Additive Manufacturing Technologies on Critical Mineral Usage and Waste for Nuclear Structural Materials,” ASTM International Conference on Advanced Manufacturing 2024 (ICAM2024), October 28, 2024–November 1, 2024.

Two peer-reviewed journal publications have been submitted for review to date from this work:

- Ankit Roy, Carolyne Burns, Steven Livers, Benjamin Lund, Subhashish Meher, Mohan Nartu, Asif Mahmud, Tianhao Wang, David Garcia, Jorge Dos Santos, Pratikshya Meher, Chinthaka Silva, Thomas Hartmann, Isabella J van Rooyen, “Critical Mineral Substitutions in IN617: A Combined Computational and Experimental Approach to Performance Evaluation and Feasibility,” submitted to *Materialia*, September 10th, 2024.
- Sun Hae Ra Shin, Thomas Hartmann, Isabella J. van Rooyen, Praveen K. Thallapally, “Fast Extraction of Nickel from Aqueous Media by Using Ionic Metal-Organic Frameworks,” submitted to *Journal of Coordination Chemistry*, September 2024.

8.0 References

Ali, A.-H., and R. El-Bishtawi. 1997. “Removal of Lead and Nickel Ions Using Zeolite Tuff.” *Journal of Chemical Technology & Biotechnology* 69: 27–34.

An, X. H., S. D. Wu, Z. F. Zhang, R. B. Figueiredo, N. Gao, and T. G. Langdon. 2010. “Evolution of Microstructural Homogeneity in Copper Processed by High-Pressure Torsion.” *Scripta Materialia* 63 (5): 560–563.

Bandura, A. V., and J. D. Kubicki. 2003. “Derivation of Force Field Parameters for TiO_2–H_2O Systems from Ab Initio Calculations.” *The Journal of Physical Chemistry B* 107 (40): 11072–11081.

Bauer, D. J., R. T. Nguyen, and B. J. Smith. 2023. *Critical Materials Assessment*. U.S. Department of Energy. Washington, DC.

Brochu, E., V. M. Cora, and N. De Freitas. 2010. “A Tutorial on Bayesian Optimization of Expensive Cost Functions, with Application to Active User Modeling and Hierarchical Reinforcement Learning.” *arXiv* preprint arXiv:1012.2599.

Broitman, E. 2017. “Indentation Hardness Measurements at Macro-, Micro-, and Nanoscale: A Critical Overview.” *Tribology Letters* 65: 23.

Burns, C. A., R. Ankit, S. Liver, B. Lund, S. Meher, M. Nartu, A Mahmud, T. Wang, D. Garcia, J. Dos Santos, P. Meher, C Silva, T. Hartmann, and I. van Rooyen. 2024. *Development Results on Replacement Materials for Current Scarce or High Supply Chain Risk Materials*. Pacific Northwest National Laboratory PNNL-36491. Richland, WA.

Capilitan, J., A. Balbin, I. D. Tabañag, and E. Taboada. 2023. “Examining Soil Erodibility, Soil pH, and Heavy Metal Accumulation in a Nickel Ore Mine: A Case Study in Tubay, Agusan del Norte, Philippines.” *Environment and Natural Resources Journal* 21 (3): 279–289. https://doi.org/10.32526/ennrj/21/202200271.

Catalini, D., D. Kaoumi, A. P. Reynolds, and G. J. Grant. 2013. “Friction Consolidation of MA956 Powder.” *Journal of Nuclear Materials* 442 (1–3): S112–S118. https://doi.org/10.1016/j.jnucmat.2012.11.054.

Coman, V., B. Robotin, and P. Ilea. 2013. Nickel Recovery/Removal from Industrial Wastes: A Review.” *Resources, Conservation and Recycling* 73: 229–238.

Couzinié, J. P., O. N. Senkov, D. B. Miracle, and G. Dirras. 2018. “Comprehensive Data Compilation on the Mechanical Properties of Refractory High-Entropy Alloys.” *Data in Brief* 21: 1622–1641. https://doi.org/10.1016/j.dib.2018.10.071.

Daulton, S., M. Balandat, and E. Bakshy. 2020. “Differentiable Expected Hypervolume Improvement for Parallel Multi-Objective Bayesian Optimization.” *Advances in Neural Information Processing Systems* 33: 9851–9864.

Daulton, S., M. Balandat, and E. Bakshy. 2021. “Parallel Bayesian Optimization of Multiple Noisy Objectives with Expected Hypervolume Improvement.” *Advances in Neural Information Processing Systems* 34: 2187–2200.

DOE. 2021. *Critical Minerals and Materials: U.S. Department of Energy's Strategy to Support Domestic Critical Mineral and Material Supply Chains (FY 2021–FY 2031)*. U.S. Department of Energy. Washington, DC.

Dutta, S., Y. D. More, S. Fajal, W. Mandal, G. K. Dam, and S. K. Ghosh, 2022. "Ionic metal-organic frameworks (iMOFs): progress and prospects as ionic functional materials." *Chemical Communications*, 58(19), 13676-13698. https://doi.org/10.1039/D2CC05131A

Elsaidi, S. K., M. A. Sinnwell, A. Devaraj, T. C. Droubay, Z. Nie, V. Murugesan, B. P. McGrail, and P. K. Thallapally. 2018. "Extraction of Rare Earth Elements Using Magnetite@MOF Composites." *Journal of Materials Chemistry A* 6 (38): 18438–18443. https://doi.org/10.1039/C8TA04750B.

Georgieva, V., M. Saraiva, N. Jehanathan, O. Lebelev, D. Depla, and A. Bogaerts. 2009. "Sputter-Deposited Mg–Al–O Thin Films: Linking Molecular Dynamics Simulations to Experiments." *Journal of Physics D: Applied Physics* 42 (6): 065107.

Ghorbani, M., M. Boley, P. N. H. Nakashima, and N. Birbilis. 2024. "An Active Machine Learning Approach for Optimal Design of Magnesium Alloys Using Bayesian Optimisation." *Scientific Reports* 14 (1): 8299. https://doi.org/10.1038/s41598-024-59100-9.

Gorokhovsky, A., M. Vikulova, J. I. Escalante-Garcia, E. Tretyachenko, I. Burmistrov, D. Kuznetsov, and D. Yuri. 2020. "Utilization of Nickel-Electroplating Wastewaters in Manufacturing of Photocatalysts for Water Purification." *Process Safety and Environmental Protection* 134: 208–216. https://doi.org/https://doi.org/10.1016/j.psep.2019.11.040.

Gorsse, S., M. H. Nguyen, O. N. Senkov, and D. B. Miracle. 2018. "Database on the Mechanical Properties of High Entropy Alloys and Complex Concentrated Alloys." *Data in Brief* 21: 2664–2678. https://doi.org/10.1016/j.dib.2018.11.111

Gröger, R., V. Vitek, and A. Dlouhý. 2020. "Effective Pair Potential for Random fcc CoCrFeMnNi Alloys." *Modelling and Simulation in Materials Science and Engineering* 28 (7): 075006. https://doi.org/10.1088/1361-651x/ab7f8b.

Gusieva, K., C. H. J. Davies, J. R. Scully, and N. Birbilis. 2015. "Corrosion of Magnesium Alloys: The Role of Alloying." *International Materials Reviews* 60 (3): 169–194.

Hall, E. O. 1951. "The Deformation and Ageing of Mild Steel: III Discussion of Results." *Proceedings of the Physical Society Section B* 64 (9): 747–755. https://doi.org/10.1088/0370-1301/64/9/303.

Hartmann, T., S. Maloy, I. J. van Rooyen. 2022. *Draft Critical Minerals Evaluation Report – Advanced Materials and Manufacturing Technology*. Pacific Northwest National Laboratory PNNL-33356. Richland, WA.

Hartmann, T., P. K. Thallapally, I. J. van Rooyen. 2023. *Strategic Plan: Decrease Critical Minerals Waste through Enabling Advanced Manufacturing Techniques*. Pacific Northwest National Laboratory PNNL-34225. Richland, WA.

Hermet, J., G. Geneste, and G. Dezanneau. 2010. “Molecular Dynamics Simulations of Oxygen Diffusion in $GdBaCo_2O_{5.5}$.” *Applied Physics Letters* 97 (17): 174102. https://doi.org/10.1063/1.3504250.

Leinonen, H., and J. Lehto, 2000. “Ion-Exchange of nickel by iminodiacetic acid chelating resin Chelex 100.” *Reactive and Functional Polymers*, 43(1-2), 1-6. https://doi.org/10.1016/S1381-5148(98)00082-0

Hund, K., D. L. Porta, T. P. Fabregas, T. Laing, and J. Drexhage. 2020. *Minerals for Climate Action: The Mineral Intensity of the Clean Energy Transition*. The World Bank - Climate-Smart Mining Facility. Washington, DC.

IAEA. 2021. *Energy, Electricity and Nuclear Powder Estimates for the Period up to 2050*. International Atomic Energy Agency. Vienna.

IEA. 2022. *The Role of Critical Minerals in Clean Energy Transitions World Energy Outlook Special Report*, p. 182. International Energy Agency. Paris, France.

IEA. 2023. *Energy Technology Perspectives 2023a*. International Energy Agency. Paris, France. https://www.iea.org/reports/energy-technology-perspectives-2023.

IEA. 2023. *Critical Mineral Market Review 2023b*. International Energy Agency. Paris, France. https://iea.blob.core.windows.net/assets/c7716240-ab4f-4f5d-b138-291e76c6a7c7/CriticalMineralsMarketReview2023.pdf.

Jiang, X., S. A. Whalen, J. T. Darsell, S. N. Mathaudhu, and N. R. Overman. 2017. “Friction Consolidation of Gas-Atomized Fe–Si Powders for Soft Magnetic Applications.” *Materials Characterization* 123: 166–172. https://doi.org/10.1016/j.matchar.2016.11.026.

Khakurel, H., M. F. N. Taufique, A. Roy, G. Balasubramanian, G. Ouyang, J. Cui, D. D. Johnson, and R. Devanathan. 2021. “Machine Learning Assisted Prediction of the Young’s Modulus of Compositionally Complex Alloys.” *Scientific Reports* 11 (1): 17149. https://doi.org/10.1038/s41598-021-96507-0.

Khaleel, M., Y. Nassar, H. J. El-Khozondar, M. Elmnifi, Z. Rajab, E. Yaghoubi, and E. Yaghoubi. 2024. “Electric Vehicles in China, Europe, and the United States: Current Trend and Market Comparison.” *International Journal of Electrical. Engineering and Sustainability* 2 (1): 1–20. https://ijees.org/index.php/ijees/article/view/70.

Kim, H., J. G. Gigax, J. Fan, F. A. Garner, T.-L. Sham, and L. Shao. 2019. “Swelling Resistance of Advanced Austenitic Alloy 709 and Its Comparison with 316 Stainless Steel at High Damage Levels.” *Journal of Nuclear Materials* 527: 151818. https://doi.org/10.1016/j.jnucmat.2019.151818.

Kołodyńska, D., J. Krukowska, and P. Thomas. 2017. “Comparison of Sorption and Desorption Studies of Heavy Metal Ions from Biochar and Commercial Active Carbon.” *Chemical Engineering Journal* 307: 353–363. https://doi.org/10.1016/j.cej.2016.08.088.

Komarasamy, M., X. Li, S. A. Whalen, X. Ma, N. Canfield, M. J. Olszta, T. Varga, A. L. Schemer-Kohrn, A. Yu, N. R. Overman, S. N. Mathaudhu, and G. J. Grant. 2021.

"Microstructural Evolution in Cu–Nb Processed via Friction Consolidation." *Journal of Materials Science* 56: 12864–12880. https://doi.org/10.1007/s10853-021-06093-9.

Krishna, R., S. V. Hainsworth, H. V. Atkinson, and A. Strang. 2010. "Microstructural Analysis of Creep Exposed IN617 Alloy." *Materials Science and Technology* 26 (7): 797–802. https://doi.org/10.1179/026708309X12584564052094.

Li, H., and F. Ebrahimi. 2003. "Synthesis and Characterization of Electrodeposited Nanocrystalline Nickel–Iron Alloys." *Materials Science and Engineering*: *A* 347 (1–2): 93–101. https://doi.org/10.1016/S0921-5093(02)00586-5.

Li, Z., Z. R. Zeng, R. Tan, M. L. Taheri, and N. Birbilis. 2023. "A Database of Mechanical Properties for Multi Principal Element Alloys." *Chemical Data Collections* 47: 101068. https://doi.org/10.1016/j.cdc.2023.101068.

Li, Z., S. Li, and N. Birbilis. 2024. "A Machine Learning-Driven Framework for the Property Prediction and Generative Design of Multiple Principal Element Alloys." *Materials Today Communications* 38: 107940. https://doi.org/10.1016/j.mtcomm.2023.107940.

Liu, J., B. P. McGrail, S. Nune, M. Sinnwell, and P. Thallapally. 2024. Polymer-Functionalized Magnetic Particle Embodiments for Solute Separation, and Devices and Systems for Using the Same. US Patent 11,944,982.

Lu, X., F. Wang, X. Li, K. Shih, and E. Y. Zeng. 2016. "Adsorption and Thermal Stabilization of Pb^{2+} and Cu^{2+} by Zeolite." *Industrial & Engineering Chemistry Research* 55 (32): 8767–8773. https://doi.org/10.1021/acs.iecr.6b00896.

Mankins, W. L., J. C. Hosier, and T. H. Bassford. 1974. "Microstructure and Phase Stability of INCONEL Alloy 617." *Metallurgical Transactions* 5: 2579–2590. https://doi.org/10.1007/BF02643879.

Maphanga, R. R., S. C. Parker, and P. E. Ngoepe. 2009. "Atomistic Simulation of the Surface Structure of Electrolytic Manganese Dioxide." *Surface Science* 603 (21): 3184–3190. https://doi.org/10.1016/j.susc.2009.07.038.

Mehmanparast, A., C. M. Davies, G. A. Webster, and K. M. Nikbin. 2014. "Creep Crack Growth Rate Predictions in 316H Steel Using Stress Dependent Creep Ductility." *Materials at High Temperatures* 31 (1): 84–94. https://doi.org/10.1179/0960340913Z.00000000011.

Minervini, L., M. O. Zacate, and R. W. Grimes. 1999. "Defect Cluster Formation in M_2O_3-Doped CeO_2." *Solid State Ionics* 116 (3–4): 339–49.

Mohammed, N. H. B., and W. Z. W. Yaacob. 2016. "Remediation of AMD Using Industrial Waste Adsorbents." *AIP Conference Proceedings* 1784 (1): 060043. https://doi.org/10.1063/1.4966881.

Moss, R. L., E. Tzimas, H. Kara, P. Willis, and J. Kooroshy. 2011. *Critical Metals in Strategic Energy Technologies - Assessing Rare Metals as Supply-Chain Bottlenecks in Low-Carbon Energy Technologies*. *JRC Scientific and Technical Reports, European Commission*. Luxembourg.

Nagib, S., K. Inoue, T. Yamaguchi, and T. Tamaru. 1999. “Recovery of Ni from a Large Excess of Al Generated from Spent Hydrodesulfurization Catalyst Using Picolylamine Type Chelating Resin and Complexane Types of Chemically Modified Chitosan.” *Hydrometallurgy* 51: 73–85.

Nassar, N. T., and S. M. Fortier. 2021. *Methodology and Technical Input for the 2021 Review and Revision of the U.S. Critical Minerals List*. U.S. Geological Survey Open-File Report 2021-1045. Reston, VA.

Natesan, A. P. K., and S. W. Tam. 2003. *Materials Behavior in HTGR Environments*. U.S. Nuclear Regulatory Commission NUREG/CR-6824/ANL-02/37. Washington, DC.

Peng, Y., H. Huang, Y. Zhang, C. Kang, S. Chen, L. Song, D. Liu, and C. Zhong. 2018. “A Versatile MOF-Based Trap for Heavy Metal Ion Capture and Dispersion.” *Nature Communications* 9 (1): 187. https://doi.org/10.1038/s41467-017-02600-2.

Piątek, J., T. M. Budnyak, S. Monti, G. Barcaro, R. Gueret, E. Svensson Grape, A. Jaworski, A. K. Inge, B. V. M. Rodrigues, and A. Slabon. 2021. “Toward Sustainable Li-Ion Battery Recycling: Green Metal–Organic Framework as a Molecular Sieve for the Selective Separation of Cobalt and Nickel.” *ACS Sustainable Chemistry & Engineering* 9 (29): 9770–9778. https://doi.org/10.1021/acssuschemeng.1c02146.

Plimpton, S. 1995. “Fast Parallel Algorithms for Short-Range Molecular Dynamics.” *Journal of Computational Physics* 117 (1): 1–19. https://doi.org/10.1006/jcph.1995.1039.

Qasem, N. A. A., R. H. Mohammed, and D. U. Lawal. 2021. “Removal of Heavy Metal Ions from Wastewater: A Comprehensive and Critical Review.” *npj Clean Water* 4 (1): 36. https://doi.org/10.1038/s41545-021-00127-0.

Qiu, Y., S. Thomas, M. A. Gibson, H. L. Fraser, and N. Birbilis. 2017. “Corrosion of High Entropy Alloys.” *npj Materials Degradation* 1 (1): 1–18.

Rai, A. K., H. Trpathy, R. N. Hajra, S. Raju, and S. Saroja. 2017. “Thermophysical Properties of Ni Based Super Alloy 617.” *Journal of Alloys and Compounds* 698: 442–450. https://doi.org/10.1016/j.jallcom.2016.12.183.

Rajaramakrishna, R., P. Nijapai, P. Kidkhunthod, H. J. Kim, J. Kaewkhao, and Y. Ruangtaweep. 2020. “Molecular Dynamics Simulation and Luminescence Properties of Eu^{3+} Doped Molybdenum Gadolinium Borate Glasses for Red Emission.” *Journal of Alloys and Compounds* 813: 151914.

Rasmussen, C. E. 2003. “Gaussian Processes in Machine Learning.” In *Advanced Lectures on Machine Learning (ML 2003)*, Lecture Notes in Computer Science, vol. 3176. edited by O. Bousquet, U. von Luxburg, and G. Rätsch. Berlin: Springer. https://doi.org/10.1007/978-3-540-28650-9_4.

Restrepo, Ó. A., Ó. Arnache, J. Restrepo, C. S. Becquart, and N. Mousseau. 2022. “Comparison of Bulk Basic Properties with Different Existing Ni-Fe-O Empirical Potentials for Fe_3O_4 and $NiFe_2O_4$ Spinel Ferrites.: *Computational Materials Science* 213: 111653. https://doi.org/10.1016/j.commatsci.2022.111653.

Revathi, M., M. Saravanan, A. B. Chiya, and M. Velan, 2012. “Removal of Copper, Nickel, and Zinc from Electroplating Rinse Water.” CLEAN-*Soil, Air, Water*, 40(1): 66-79. http://dx.doi.org/10.1002/clen.201000477

Richard, C.. “Global Wind Fleet Set to Reach 5.9TW by 2050 – DNV.” Windpower Monthly. 1 September, 2021

Roy, A., R. Devanathan, D. D. Johnson, and G. Balasubramanian. 2022a. “Grain-Size Effects on the Deformation in Nanocrystalline Multi-Principal Element Alloy.” *Materials Chemistry and Physics* 277: 125546. https://doi.org/10.1016/j.matchemphys.2021.125546.

Roy, A., M. F. N. Taufique, H. Khakurel, R. Devanathan, D. D. Johnson, and G. Balasubramanian. 2022b. “Machine-Learning-Guided Descriptor Selection for Predicting Corrosion Resistance in Multi-Principal Element Alloys.” *Materials Degradation* 6 (1): 9. https://doi.org/10.1038/s41529-021-00208-y.

Schulz, E., M. Speekenbrink, and A. Krause. 2017. “A Tutorial on Gaussian Process Regression: Modelling, Exploring, and Exploiting Functions.” *bioRxiv*: 095190. https://doi.org/10.1101/095190.

Sharma, A., and G. Balasubramanian. 2017. “Dislocation Dynamics in $Al_{0.1}$CoCrFeNi High-Entropy Alloy under Tensile Loading.” *Intermetallics* 91: 31–34. https://doi.org/10.1016/j.intermet.2017.08.004.

Shi, B., T. Lookman, and D. Xue. 2023. “Multi-objective Optimization and Its Application in Materials Science.” *Materials Genome Engineering Advances* 1 (2): e14. https://doi.org/10.1002/mgea.14.

Singh, P., A. Sharma, A. V. Smirnov, M. S. Diallo, P. K. Ray, G. Balasubramanian, and D. D. Johnson. 2018. “Design of High-Strength Refractory Complex Solid-Solution Alloys.” *npj Computational Materials* 4 (1): 16.

Smith, D. S., N. J. Lybeck, J. K. Wright, and R. N. Wright. 2017. “Thermophysical Properties of Alloy 709.” *Nuclear Engineering and Design* 322: 331–335. https://doi.org/10.1016/j.nucengdes.2017.07.016.

Solar Energy Technologies Office. n.d. “Solar Futures Study.” energy.gov. Accessed July 26, 2022. https://www.energy.gov/eere/solar/solar-futures-study.

Solomou, A., G. Zhao, S. Boluki, J. K. Joy, X. Qian, I. Karaman, R. Arróyave, and D. C. Lagoudas. 2018. “Multi-objective Bayesian Materials Discovery: Application on the Discovery of Precipitation Strengthened NiTi Shape Memory Alloys through Micromechanical Modeling.” *Materials & Design* 160: 810–827. https://doi.org/https://doi.org/10.1016/j.matdes.2018.10.014.

Stukowski, A. 2009. “Visualization and Analysis of Atomistic Simulation Data with OVITO–The Open Visualization Tool.” *Modelling and Simulation in Materials Science and Engineering* 18 (1): 015012. http://doi.org/10.1088/0965-0393/18/1/015012.

Svensson Grape, E., A. J. Chacón-García, S. Rojas, Y. Pérez, A. Jaworski, M. Nero, M. Åhlén, E. Martínez-Ahumada, A. E. Galetsa Feindt, M. Pepillo, M. Narongin-Fujikawa, I. A. Ibarra, O. Cheung, C. Baresel, T. Willhammar, P. Horcajada, and A. K. Inge. 2023. “Removal of

Pharmaceutical Pollutants from Effluent by a Plant-Based Metal–Organic Framework.” *Nature Water* 1 (5): 433–442. https://doi.org/10.1038/s44221-023-00070-z.

Sverdrup, H., and K. V. Ragnarsdottir. 2014. “Natural Resources in a Planetary Perspective.” *Geochemical Perspectives* 3 (2): 129–341. https://doi.org/10.7185/geochempersp.3.2.

Sverdrup, H. U., D. Koca, and K. V. Ragnarsdottir. 2013. “Peak Metals, Minerals, Energy, Wealth, Food and Population: Urgent Policy Considerations for a Sustainable Society.” *Journal of Environmental Science and Engineering B* 2 (4): 198–222.

Taufique, M. F. N., O. Mamun, A. Roy, H. Khakurel, G. Balasubramanian, G. Ouyang, J. Cui, D. D. Johnson, and R. Devanathan. 2024. “Machine Learning Guided Prediction of the Yield Strength and Hardness of Multi-principal Element Alloys [Version 2; Peer Review: 2 Approved, 2 Approved with Reservations].” *Materials Open Research* 2: 9. https://doi.org/10.12688/materialsopenres.17476.2.

Takeuchi, A., and A. Inoue. 2005. “Classification of Bulk Metallic Glasses by Atomic Size Difference, Heat of Mixing and Period of Constituent Elements and Its Application to Charcterization of the Main Alloying Element.” *Materials Transactions* 46 (12): 2817–2829.

Thallapally, P. K., I. J. van Rooyen, S. S. Hera, T. Hartman, and H. Goettesche. 2024. *Co-extraction of Critical Minerals from Advanced Manufactured Processes*. PNNL Invention Disclosure IPID 33099-E.

Thermo-Calc Software. n.d. a. “TCFE13 Steels/Fe-alloys Database.” Thermo-Calc Software. Accessed September 25, 2024. https://thermocalc.com/products/databases/steel-and-fe-alloys/.

Thermo-Calc Software. n.d. b. “TCHEA7 High Entropy Alloys Database.” Thermo-Calc Software. Accessed September 25, 2024. https://thermocalc.com/products/databases/high-entropy-alloys/.

Ünlü, N., and M. Ersoz. 2007. “Removal of Heavy Metal Ions by Using Dithiocarbamated-sporopollenin.” *Separation and Purification Technology* 52 (3): 461–469. https://doi.org/10.1016/j.seppur.2006.05.026.

US Office of Nuclear Energy. 2020. “New Alloy Material Approved for Use in High-Temperature Nuclear Plants” Accessed August 8, 2024. https://www.energy.gov/ne/articles/new-alloy-material-approved-use-high-temperature-nuclear-plants

US Office of Office of Energy Efficiency & Renewable Energy. 2024. *Solar Futures Study*. Accessed August 26th, 2024. https://www.energy.gov/eere/solar/solar-futures-study.

Upadhayay, S., H. Li, P. Bowen, and A. Rabiei. 2018. “A Study on Tensile Properties of Alloy 709 at Various Temperatures.” *Materials Science and Engineering A* 733: 338–349. https://doi.org/10.1016/j.msea.2018.06.089.

van Rooyen I., S. Meher, P. K. Thallapally, J. Fernandez dos Santos, C. M. Silva, S. Shin, T. Wang, D. Garcia, M. Nartu, QRS. Miller and T Hartman. 2024. *Nuclear Energy Critical Material Waste Minimization Enabled by AM Techniques*. Pacific Northwest National Laboratory PNNL-36049. Richland, WA.

Verhoef, L. A., B. W. Buddle, C. Chockalingam, B. G. Nodar, and A. J. M. van Wijk. 2018. “The Effect of Additive Manufacturing on Global Energy Demand: An Assessment Using a Bottom-up Approach.” *Energy Policy* 112: 349–360.

Wang, Y., Q. Liu, Z. Cai, H. Wang, L. Shi, and K. Li. 2023. “Nitride Precipitation and Formation in In617 Superalloy During Creep.” *Journal of Alloys and Compounds* 948: 169709.

Wen, C., Y. Zhang, C. Wang, D. Xue, Y. Bai, S. Antonov, L. Dai, T. Lookman, and Y. Su. 2019. “Machine Learning Assisted Design of High Entropy Alloys with Desired Property.” *Acta Materialia* 170: 109–117. https://doi.org/10.1016/j.actamat.2019.03.010.

Zhang, P., S. X. Li, and Z. F. Zhang. 2011. “General Relationship between Strength and Hardness.” *Materials Science and Engineering: A* 529: 62–73. https://doi.org/10.1016/j.msea.2011.08.061.

Zhou, X. W., R. A. Johnson, and H. N. G. Wadley. 2004. “Misfit-Energy-Increasing Dislocations in Vapor-Deposited CoFe/NiFe Multilayers.” *Physical Review B* 69 (14): 144113. https://doi.org/10.1103/PhysRevB.69.144113.

Pacific Northwest National Laboratory

902 Battelle Boulevard
P.O. Box 999
Richland, WA 99354

1-888-375-PNNL (7665)

www.pnnl.gov